Modelling of radon transport in the KVI radon vessel

van der Spoel, W.H.

Award date:
1993

R-57

Modelling of radon transport in the KVI radon vessel

W.H. van der Spoel 27 juli 1993

Kernfysisch Versneller Instituut
Zernikelaan 25, 9747 AA Groningen

Supervisors: Dr. E.R. van der Graaf
Prof. Dr. R.J. de Meijer

This report is submitted to the Eindhoven University of Technology, the faculty of Physical Engineering, in partial fulfillment of the requirements for obtaining the M.Sc. degree.

Summary

At the KVI a laboratory facility 'the radon vessel' has been built to study radon transport in soil under well defined and controlled conditions. It consists of a 2 m high vessel with a diameter of 2 m, filled with sand. The radon concentration in the soil can be determined at several different depths.

This report is an account of the modelling of radon transport in this laboratory facility. Based on the fundamental equations that describe radon transport in porous materials, three techniques are considered to find values for the radon concentration in soil. The first technique is an analytical method to find an expression for the radon concentration in soil as function of depth and time under diffusive conditions only. To obtain values for the tortuosity and emanation factor, this expression was fitted to experimental data. The other two techniques imply numerical procedures based on the finite-difference approach. The first numerical model calculates the radon concentration as function of time in one spatial dimension, while the other model is able to perform these calculations in two spatial dimensions. Experimental data, obtained under combined diffusive and advective radon transport, were analysed by means of the two numerical models.

From this exercise, it is concluded that radon transport in the laboratory facility under advective conditions can only be understood and described with the 2D model, i.e. in this situation radon is transported not only in the axial direction of the vessel, but also in the radial direction. Further, model predictions of the radon concentration with the 2D model are accurate within 15% when values for the tortuostiy and emanation factor are used that were found using the analytical expression for the radon concentration under diffusive conditions only. However, it is possible to obtain model predictions accurate within 5%, using slightly different values for these parameters. Indications are present that the emanation factor and tortuosity may have changed during the experiments with the radon vessel.

Contents

Chapter 1

Introduction

Natural materials consist of a variety of different elements, from the lightest element hydrogen to the heaviest element uranium. The distribution of elements in the solid surface of planet earth is far from homogeneous. Locally high concentrations of heavy elements can occur in solid rock. Some of these elements are radioactive and belong, except ^{40}K, to one of the three natural occuring decay series, namely that of uranium, thorium or actinium. Each of these series contains the decay of a radium isotope into a radon isotope. Radon is an inert gas. This implies that it has little affinity to get chemically bound to other materials. In contrast to solid rock, sediments like sand, clay and gravel originate from a large area and therefore the distribution of heavy elements in these materials is more homogeneous. In general also the concentration of heavy elements is lower.

The health risk for humans with respect to radioactivity lies in the fact that radiation may cause damage in matter. For radon, the radon progeny predominantly are of risk for humans. These progeny may adhere to dust-particles in air that, in turn when inhalated, may attach to the tissue in our lungs. In the decay of the radon-daughters α-particles are emitted which damage the lung tissue and so may induce lung cancer. According to the latest investigations in the Netherlands 450-1800 fatal lung-cancers per year occur due to radiation from radon progenies [Ba91].

In the Netherlands we are living on sediments like sand and clay and as a result the research at the KVI involving radon transport in soil is carried out for these type of materials.

Radon isotopes have different half-lifes: 3.85 days for ^{222}Rn, a progeny of ^{238}U, 56 seconds for ^{220}Rn, also called thoron and originating from ^{232}Th. The third isotope ^{219}Rn has a half-life of approximately 4 seconds. When radon decays while it is still in the soil, its daugther element will be bound to the solid phase and will not contribute to the exposure dose. Due to its relatively long half life ^{222}Rn has the largest chance to be exhalated into free air and consequently most measurements are executed to determine the concentration of this particular isotope in air. For this reason 'radon' will be used in this report, referring to ^{222}Rn.

In Fig. 1.1 the decay series of ^{238}U is shown. The half life of the parent nuclide ^{238}U is much longer than the half lifes of all its progenies. Under the assumption that the earth is ca. $5{\cdot}10^9$ years old and that none of the elements between ^{238}U and radon escape, it implies that the activity of all these elements in this series is the same (secular equilibrium). As a consequence the production rate of radon is constant as function of time.

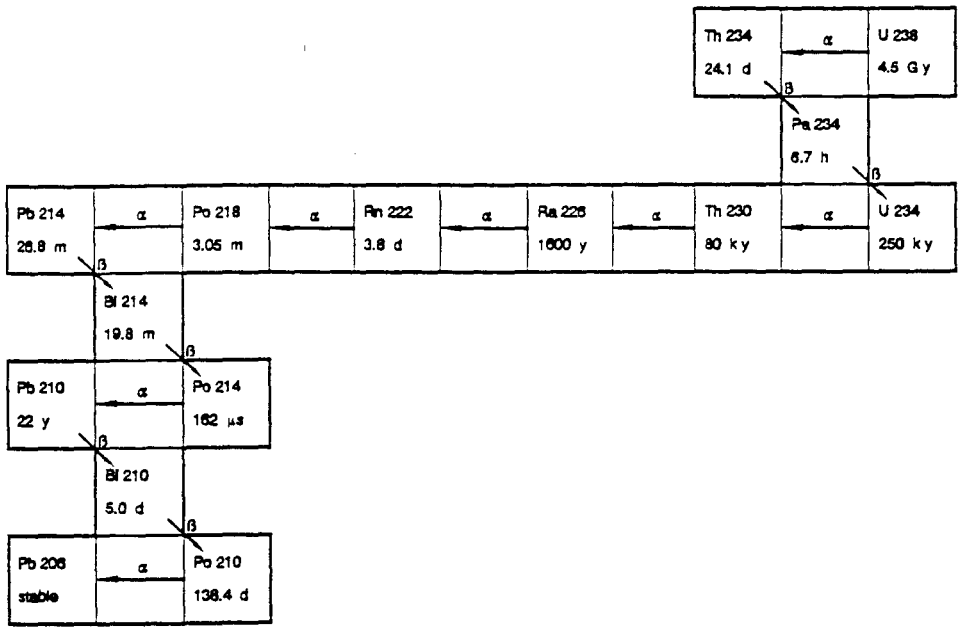

Figure 1.1: Decay scheme of ^{238}U.

The amount of radon and thoron that is produced depends on the activity concentration of ^{226}Ra and ^{224}Ra, the direct parents of radon and thoron, respectively. These activity concentrations can be measured by means of gamma-spectroscopy. A device for this purpose is available at the KVI.

In the experiments described in this report, measurements of radon concentration in soil concern only radon which is present in the air-filled pore space. This will be a fraction of all the radon that was formed in the soil. Part of it stays inside the grains or inside the liquid phase. There are also indications [Ro91a] that the fraction of radon (emanation factor) which escapes out of the solid phase into the pore space is a function of the pore-water content. Presently this moisture dependency of the emanation factor is being measured with an instrument specially designed for this purpose [An92a]. In addition to this the emanation factor also depends on size, shape and composition of the soil particles.

Before radon can escape into the air that we breathe, it has to move through the material in which it was formed. Radon transport takes mainly place in the pore space of the material. Driving forces for this transport are diffusion and advection. The latter is caused by a pressure gradient of the air in the pore space.

Diffusion, driven by radon concentration gradients, is most significant in the gas phase. The diffusion coefficient of radon in air ($= 1.1 \cdot 10^{-5}$ m^2 s^{-1}) is about 1000 times larger than in water. Nevertheless, diffusion in the aqueous phase may not be neglected because frequent intermittent blockage of soil pore segments by water will occur. If soil is saturated with water, there is no gas phase and all diffusion takes place in the liquid phase. As a result the diffusion coefficient can vary over at least three orders of magnitude depending on the moisture content of the soil.

Advection, resulting from pressure-driven flow of soil gas, carries radon at the soil

gas velocity. The relative importance of advection depends on the magnitude of pressure gradients and permeability of the soil. Pressure gradients applied over the soil in the experiments described in this report were in the order of 1 Pa m^{-1}. For these pressure gradients Darcy's law may be applied which states that the transport of soil gas is linear proportional to the pressure gradient.

The exposure in the indoor environment is larger than the outdoor exposure due to accumulation of radon in indoor air and to longer residence time. Soil (appr. 70%) and building materials (appr. 30%) are the most important sources for indoor radon [Ba91]. Investigations of radon infiltration in dwellings [Me91] show that radon transport in soil is a complicated process in which pressure gradients, permeability, porosity, ground water level and water content of pores have a large influence on radon production and transport. Therefore validation of models on the basis of measurements of radon concentration in soil under natural conditions is an almost impossible task, because of the relatively rapid and uncontrollable variation of parameters that influence radon concentration. With respect to this, one of the recommendations stated in [Me91] was to study radon transport in soil under controlled conditions.

The laboratory facility (the radon vessel) that has been built for this purpose will be described in this report. The emphasis of this work will be on the mathematical description of radon transport in soil, applied to the geometry and conditions valid for this facility. Chapter 2 will give an outline of the experimental facility and procedures involved for the determination of radon activity concentration. In Chapter 3 the fundamental equations describing radon transport in soil will be derived. The models considered can be divided into 3 parts, covering Chapters 4, 6 and 7. First, in Chapter 4, a time-dependent analytical solution for diffusive radon transport in a homogeneous material will be derived with appropriate boundary conditions. Analytical solutions can be derived for even more complex situations (e.g. time-dependent solutions with diffusive and advective radon transport), but it was noticed that this exercise is extremely complex and minute. For this reason it was decided to focus on numerical recipes. In Chapter 5 the principles of finite differences are presented as well as the effects of discretisation on the numerical solution. In Chapter 6 a one-dimensional numerical procedure will be presented that calculates the radon activity concentration as a function of time and space in a non-homogeneous material for various boundary conditions under diffusive and advective conditions. When the radon vessel was built, it was assumed that radon transport in the sand column would almost be completely one-dimensional. In order to check this assumption, a two-dimensional (2D) model was constructed partly based on the method used for the 1D numerical model. This model will be described in detail in Chapter 7. Finally the results of the first experiments with the radon vessel will be presented in Chapter 8 and will be compared with the models and some preliminary conclusions will be drawn.

Chapter 2

Experimental methods

2.1 Introduction

Measurements of radon concentrations in soil under various but controlled conditions were performed using a laboratory facility that has been described in detail in [Va92a]. In short, this facility consists of a 2 m high vessel with a diameter of 2 m, filled with soil. The vessel can be closed with a height-adjustable lid. In general, soil, in the Netherlands mainly existing of clay and sand, is a porous material. Such a material can be described as being composed of three different phases. viz, solid phase (soil grains), gas phase (air-filled pore space) and a liquid phase (water-filled pore space). With probes inserted radially at several heights in the vessel the radon concentration, the pore-water content and soil permeability may be measured. In this chapter the laboratory facility and experimental procedures will be described.

2.2 The radon vessel

2.2.1 General description and features

The laboratory facility, shown schematically in Fig. 2.1, consists of a stainless-steel vessel with a diameter and height of 2 m, filled with soil. These dimensions have been chosen on the basis of the available space in the building, the maximum load of the floor and the diffusion length of radon which, for highly porous materials, is in the order of 2 m. Consequently, only a minor influence of boundary effects is expected and for wet soil those effects are probably even negligible.

Since the vessel, when filled with soil, contains a mass of about 10 tons, the bottom is made somewhat concave for strength. The vessel is surrounded by a watertight ring in which the lid can be lowered. The water inside the ring acts as a seal for air and radon. The space between the lid and the soil is meant to simulate a crawl space under a dwelling and is adjustable in height. Multi-functional probes are inserted radially at 9 different heights. The centre of the perforated section of the probes is situated exactly in the middle of the vessel. With these probes, air, present at the central axis of the vessel, can be sucked out of the sand for radon activity concentration analysis. Also the pore-water content can be determined by means of measuring the pore-water suction with a pressure transducer.

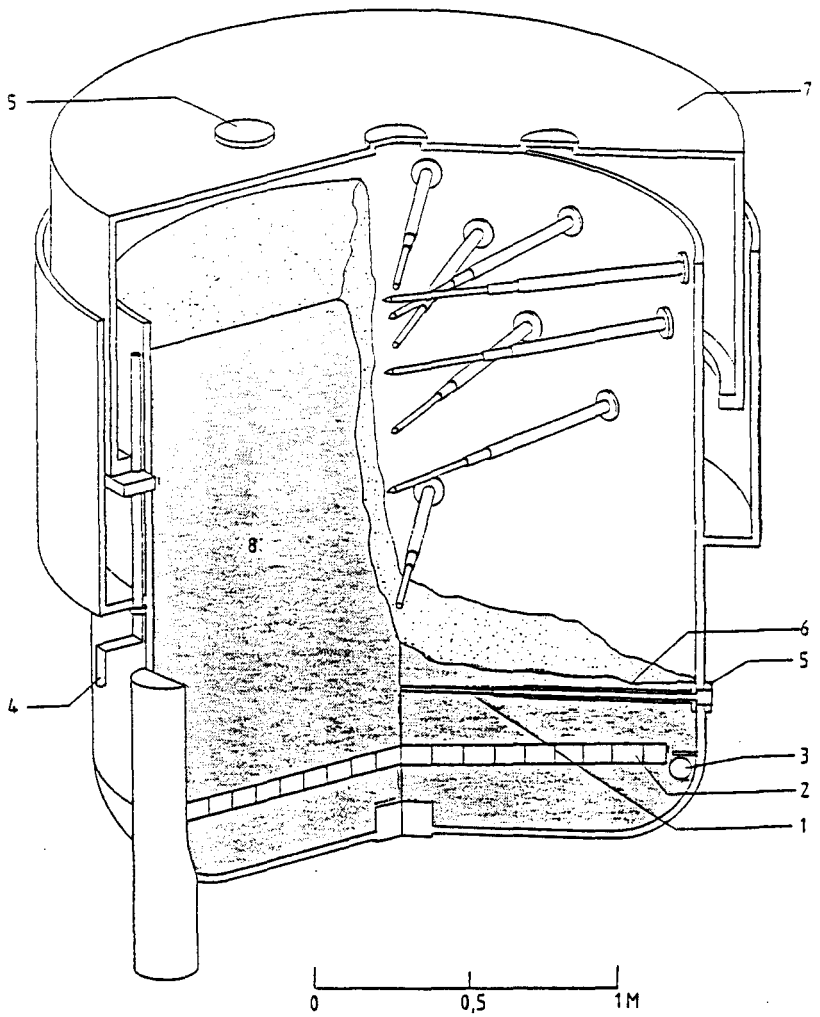

Figure 2.1: Schematic drawing of the vessel. 1) multi-functional probe; 2) perforated cylindrical box; 3) drainage tube (not present at the moment); 4) adjustment point for height of the lid; 5) flange; 6) sleeve; 7) lid of the vessel; 8) soil.

The air permeability of the soil near that particular probe may be derived by inducing an air flow through the probe and by measuring the flow and the air pressure increase needed to reach this flow. The main objective of the radon vessel experiments is to measure the radon concentration inside the soil as function of depth (radon concentration profile) under various conditions. The following conditions can be controlled:

Soil type: An optimal soil for a designed experiment can be selected. Another possibility is to have two or more different layers of soil in the vessel.

Ground-water level: Through a water inlet/outlet in the bottom of the vessel, water may enter or leave the soil. The time schedule for the radon vessel experiments did not permit measurements of the influence of the ground-water level on the radon concentration before September 1993. Until May 1993 only measurement with dry soil have been executed. For this reason also the model tests, although suited for moisturised and non-homogeneous soil, have been restricted to dry, homogeneous sand.

Pressure gradient in the soil: A perforated box with a diameter of 162 cm and a height of 3 cm is situated at a depth of ca. 163 cm under the soil surface. Via a plastic tube, entering the vessel at the centre of the bottom and also entering the pressure box at the centre, air can be pumped into or sucked out of the pressure box. The box itself is filled with a perforated glass-fiber grating and is covered at both sides by perforated metal plates. By pumping air through the soil a pressure field is induced inside the soil. Measurements with different flow rates have been carried out.

Irigation of soil: With the use of sprinklers in the lid, rain fall can be simulated. Experiments with this feature have not been executed. The models do not have the possibility to simulate rain fall, although probably only a small effort is required to add this phenomenon, that so often occurs in the Netherlands.

Crawl-space parameters: The height of the air column under the lid is adjustable from ca. 5 to 50 cm. In addition, also the ventilation rate of the pseudo crawl space can be varied. Both can be modelled and measurements are in progress.

2.2.2 The radon vessel geometry

In Fig. 2.2 the vertical cross-section of the vessel through the symmetry axis is shown. The cavity at the centre of the bottom is closed on top and surrounded by a fine stainless steel mesh through which sand can not penetrate. This cavity was constructed with the aim that water can enter or leave the vessel without taking sand with it. During the measurements this cavity was closed at the bottom with a flange.

To supply the vessel its needed firmness, two metal rings were constructed: near the top and at the location where the concave bottom of the vessel is attached (in further discussion, when the word 'ring' is used, it is meant as a reference to the latter ring). Especially the ring, covering approximately one third of the horizontal cross-section at that particular location, has an influence on the transport of radon and the pressure field inside the soil. The top of the pressure box is at a depth of 163 ± 0.5 cm and its bottom is located exactly inside the ring, leaving a space of only 0.5 cm between the ring and the box. The diameter of the pressure box is 162 cm.

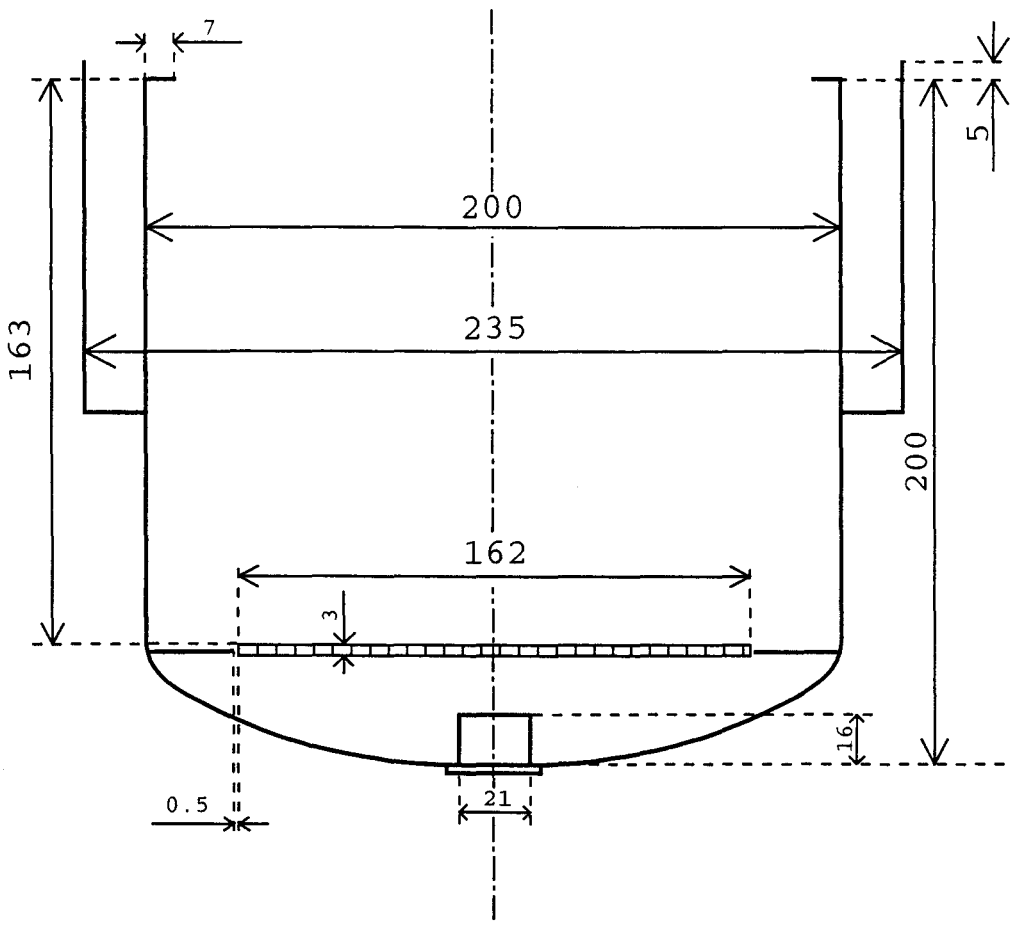

Figure 2.2: Vertical cross-section of the radon vessel through the symmetry axis. Dimensions are given in centimeters.

Nine probes radially penetrate the vessel at nine different depths below the soil surface. In Table 2.1 the depth of the probes are indicated. Accuracy of the probe depth is about 5 mm.

probe number	probe depth (cm)
1	10
2	15
3	20
4	30
5	40
6	60
7	80
8	120
9	150

Table 2.1: Depth of the probes inside the radon vessel relative to the surface of the sand column.

2.3 Soil type

In general, soils may be characterised by the following parameters:

Porosity: This is the volume fraction of the total bulk volume which is not occupied by the grains.

Permeability: The air flow through soil is directly proportional to the applied pressure gradient (at small gradients). The permeability is the constant defining the relation between air flow and pressure gradient.

Bulk dry density: Mass per unit bulk volume of dry soil.

Tortuosity: This is a factor which indicates the ratio between the straight distance from point A to point B (distance much larger than the mean grain size) and the path length for a particle moving from point A to point B in the pores of a porous medium. The tortuosity is an important factor for diffusion processes and is also related to the grain-size distribution and pore-water content.

Water-retention curve: The functional relationship between the pore-water content and the pore-water pressure is given by the water-retention curve. Soils existing mainly of large grains tend to loose water easily. When part of the soil is saturated with water, these soils will show a small transition range from wet to dry soil, whereas soils with mainly small grains (clay) will retain water even at low water pressure, resulting in a large transition range.

Radium content: Defined as the radium activity per unit bulk dry mass. Depending on origin and composition, radium content of sand varies from approximately 3 to 20 Bq kg^{-1} in the Netherlands [Va92b].

Emanation factor: The fraction of radon that is available for transport. The emanation factor depends on the pore-water content.

Based on desired soil characteristics for the first measurements with the radon vessel the sand type 'Ankersmit 0.25-0.50 mm' was selected [Va92b]. The parameters for this sand type are given in Table 2.2.

Grain size	0.25 - 0.50 mm
Porosity	0.36 ± 0.018
Bulk dry density	$(1.76 \pm 0.09) \cdot 10^3$ kg m^{-3}
Tortuosity (dry)	0.73 ± 0.06
Permeability	$(5.45 \pm 0.13) \cdot 10^{-11}$ m^2
Radium content	3.68 ± 0.13 Bq kg^{-1}
Emanation factor	0.243 ± 0.013

Table 2.2: Parameters of the sand type 'Ankersmit 0.25 - 0.50 mm', that was used in the radon vessel experiments.

The emanation factor and tortuosity were calculated from experiments carried out in the radon vessel, see Chapter 8. Former independent measurements of the emanation factor of this sand resulted in a value of 0.10 $\pm$0.03 [Va92b]. Supplementary experiments with the same instrument indicated 0.13 $\pm$0.02 (not published). It is not clear what causes this discrepancy; experiments are in progress to examine this. Since this report focusses on the modelling of radon transport in soil, an extensive discussion on the measuring techniques will be omitted. The value of the permeability was determined from measuring the air pressure at the probes with an air flow through the sand column [Va93a]. Parameters given in Table 2.2 are taken as input for the models. The water-retention curve can be found in [Va92, p. 15 g].

Another parameter involved, but not characteristic for the soil type, is the homogeniety of the sand column in the vessel. Regarding the validation of radon-transport models, a good homogeneous soil is required. From a check of the homogeniety, described in [Va93c], it was concluded that deviations from the ideal case are less than approximately 15%.

2.4 Radon-concentration analysis

To measure a radon-concentration profile inside the sand in the vessel, air samples were taken via the probes located at nine depths under the sand surface. Since we are only interested in the radon concentration inside the sand, first 0.5 liter is sucked out of the probes and discarded (the volume of air inside the probes, ca. 0.3 liter, is not of interest). Then a second sample of 0.5 liter is taken with a piston. (The functional relationship between the radon concentration and the amount of air that is sucked out of the pores has been determined. From this function it was observed that, at first, the radon concentration increases with increasing air volume and thereafter, the radon concentration is more or less constant as function of the air volume. It was decided to sample the air volume at which the radon concentration has just reached the constant value.) With this procedure about

9 liter of soil gas is removed from the sand when all nine probes are sampled. Regarding the total air volume inside the sand column, which is approximately 2 m^3, the disturbance of the radon concentration profiles due to sampling is likely to be negligible.

After the piston is filled with soil gas, radon and thoron concentrations will decrease due to radioactive decay. To measure only the ^{222}Rn concentration, the piston is left undisturbed for 15 minutes or longer. After this period it is assumed that all thoron (^{220}Rn), with a half life of about 56 seconds, will have decayed into its daughter products. Then the air inside the piston is led through a filter into an evacuated Lucas cell. This filter is used to intercept all radon and thoron daughters.

A Lucas cell is an airtight metal cilinder that has a transparant window at one end and an air inlet/outlet at the other end. The inside of the cell (except for the window) is covered with a scintillation material sensitive to α-radiation. In the decay series of ^{222}Rn α-particles are produced by ^{222}Rn and its daughter products. The Lucas cell can be mounted onto a monitor (Pylon model AB-5 portable radiation monitor from Pylon Electronic Development Company, Ltd. Ottawa, Canada) which is equipped with a photo-multiplier tube to count the number of light pulses from the scintillation material. Routinely, the number of counts in 30 minutes is stored into memory for subsequent time intervals during ca. 24 h. Regarding the fact that several monitors and Lucas cells are used, all the monitors and Lucas cells have been calibrated to eliminate systematic errors introduced by different efficiencies [Va93b]. The relative standard deviation in the activity concentration determined with this procedure is calculated to be less than 5%.

To be able to correct for possible systematic errors, for each probe the same combination of piston, Lucas cell and Pylon monitor was used.

2.5 Radon-profile measurements

In this report the measurements with the vessel until May 1993 will be discussed and compared with calculations. Until that date only measurements of radon concentration as function of depth (radon-concentration profile) without the lid and with dry soil were performed. In principle two types of conditions inside the vessel have been examined:

Type 1: In this case only diffusion is the driving force for radon transport; no air flow was induced through the sand column.

Starting from an initial condition in which the radon concentration is practically zero inside the sand, the radon concentration will increase due to radon production. The radon atoms formed will decay, and may also escape at the top of the sand column (no lid on top of the vessel). These processes, combined with diffusion, will generate a radon concentration profile that will develop as a function of time until equilibrium is reached. Considering the half life of radon, a measurement of the complete ingrowth from zero to equilibrium concentration takes about three weeks. A measurement of a radon profile takes about one day. For this reason the time resolution is limited to one day.

To start with zero concentration inside the sand a flow rate of 50 L min^{-1} for 24 hours is induced through the pressure box. Measurements of the radon concentration in the soil just after flushing showed that at all depths the radon concentration was below 40 Bq m^{-3}.

Two measurements were carried out to determine radon profiles as function of time.

Type 2: These measurements were performed with an air flow induced inside the sand column in the upward direction via the pressure box. In this case, besides diffusion, also advection plays a role. Because the equilibrium state is reached sooner than in the case of diffusive transport only and considering the minimum time resolution of one day, only radon profiles were measured in the equilibrium state. For each flow rate through the pressure box, three radon profiles were measured.

In Table 2.3 the measurements with the radon vessel that are discussed in this report are arranged schematically.

type	description	measurement	profile taken
1	diffusion	1	at t = 24, 48, 72, 96, 120, 144 h
		2	at t = 7, 31, 55, 79, 103, 127, 151 h
2	diffusion	1	flow = 0.1 L min^{-1} steady state
	+	2	flow = 0.2 L min^{-1} ,,
	advection	3	flow = 0.4 L min^{-1} ,,
		4	flow = 0.8 L min^{-1} ,,
		5	flow = 2.2 L min^{-1} ,,
		6	flow = 6.5 L min^{-1} ,,
		7	flow = 10 L min^{-1} ,,

Table 2.3: Overview of the measurements with the radon vessel described in this report.

Chapter 3

Equations for radon transport in porous materials

In this chapter the equations describing radon transport in porous materials will be derived. In this derivation the effect of moisture in the soil and adsorption on the surface of the solid phase is (partly) accounted for. However, model calculations and measurements have only been executed for dry sand. Further, in these calculations, it is assumed that adsorption of radon to sand grain surfaces can be neglected for dry sand.

3.1 Some definitions

A soil volume V (m^3) containing gaseous, liquid and solid material may be considered as the sum of contributions from various phases of interest. For example, the volume may be subdivided into

$$V = V_g + V_w + V_s, \tag{3.1}$$

where g, w, s refer to gaseous, liquid, and solid phases, respectively. From Eq. (3.1) the volume of pore space (V_p) per total volume, ϵ, called porosity, may be derived:

$$\epsilon = \frac{V_p}{V} = 1 - \frac{V_s}{V} = \epsilon_a + \epsilon_w, \tag{3.2}$$

where ϵ_a is the volume of gas space per total volume, called air porosity, and ϵ_w is the volume of liquid per total volume, called water porosity. The fraction of water saturation of the pores, m, is defined as:

$$m = \frac{\epsilon_w}{\epsilon}. \tag{3.3}$$

3.2 Radon generation and decay

Radon is formed in the decay of radium, present in the soil grains. The radium activity per unit bulk volume is given by ρC_{Ra}, where ρ is the bulk density of dry soil and C_{Ra} the radium activity per unit dry bulk mass. The rate of change of the number of radon atoms (N_{Rn}) in a bulk volume V is determined by the decay and production (radium activity) of radon:

$$\frac{dN_{Rn}}{dt} = -\lambda N_{Rn} + \rho C_{Ra} V, \tag{3.4}$$

where λ is the decay constant of radon ($= 2.1 \cdot 10^{-6}$ s^{-1}). The rate of change of the number of radon atoms in the pore volume (N_{Rn}^{p}) is, multiplying the production term in Eq. (3.4) with the radon emanation factor η (the fraction of radon atoms that become available for transport) gives

$$\frac{dN_{Rn}^{\mathrm{p}}}{dt} = -\lambda N_{Rn}^{\mathrm{p}} + \eta\rho C_{Ra} V. \tag{3.5}$$

Multiplying this equation with the decay constant λ and using the relation $\epsilon VC = \lambda N_{Rn}^{\mathrm{p}}$, where C is the radon-activity concentration in the pore space, results in:

$$\frac{dC}{dt} = -\lambda C + \frac{\eta\rho\lambda C_{Ra}}{\epsilon}. \tag{3.6}$$

The second term at the righthand side of Eq. (3.6) is defined as the radon production term S (Bq m^{-3}s^{-1}):

$$S = \frac{\eta\rho\lambda C_{Ra}}{\epsilon}. \tag{3.7}$$

This generation rate may be divided into three terms, S_a, S_w and S_s, reflecting the emanation of radon atoms into the air-filled pore parts (η_a), water-filled pore parts (η_w) and solid surface (η_s). Therefore we have the relation:

$$S = (\eta_a + \eta_w + \eta_s)\frac{\rho\lambda C_{Ra}}{\epsilon} = S_a + S_w + S_s. \tag{3.8}$$

3.3 Radon transport

3.3.1 Diffusion

Diffusion in isotropic media is based on the hypothesis that the rate of transfer of a diffusing substance through an unit area $\vec{F}$ (m^{-2} s^{-1}) is proportional to the concentration gradient measured normal to this area, i.e. Fick's law:

$$\vec{F} = -D\nabla C, \tag{3.9}$$

where D (m^2 s^{-1}) is the bulk diffusion coefficient.

In terms of the bulk flux of radon activity $\vec{j_d}$ (Bq m^{-2} s^{-1}) caused by diffusion, we may write

$$\vec{j_d} = -D\nabla C_a, \tag{3.10}$$

where the subscript d is a reference to diffusion and C_a is the radon activity concentration (Bq m^{-3}) in the air-filled pore space. We assume that radon transport in the liquid phase is negligible over a distance that is much larger than the grain size. But actually, for porous materials the bulk diffusion coefficient D can be written as

$$D = \epsilon_a\tau_a D_a + \epsilon_w\tau_w D_w, \tag{3.11}$$

in which τ_a and τ_w are so called tortuosity factors of the material for transport in the air and liquid phase and where D_a and D_w are the diffusion coefficients of radon in air and liquid, respectively. The tortuosity factors account for the effect of the tortuous path

of radon atoms in the material. Effectively the result is a smaller diffusion coefficient ($0 < \tau \leq 1$, further in this report τ is used to specify τ_a). For wet soil there is diffusion in the air-filled pore space as well as in the water-filled pore space. This means that D will decrease with increasing moisture saturation. Theoretical developments to describe the moisture dependence of the bulk diffusion coefficient are hampered by the number of parameters involved. In [Ro91b] an empirical relation between diffusion coefficient and moisture saturation is stated.

3.3.2 Advection

Gases in soil can be displaced by bulk movement of the soil air phase in response to differences in air pressure. These pressure differences can be induced by wind, rainfall, temperature and ventilation effects. Here we assume only ventilation, e.g. that the soil gas moves in response to pressure differences imposed at the boundaries. For the magnitude of the pressure gradients applied in the radon vessel (< 20 Pa per meter), Darcy's law (equation of motion for a porous medium) may be used:

$$\vec{q} = -\frac{k}{\mu}\nabla p, \tag{3.12}$$

where $\vec{q}$ is the bulk flux of soil gas ($\mathrm{m^3\,m^{-2}\,s^{-1}}$), k the intrinsic permeability of the medium ($\mathrm{m^2}$) and μ the dynamic viscosity of air ($1.83 \cdot 10^{-5}$ Pa s). The equation of continuity for flow through a porous medium is [Bi60]:

$$\epsilon\frac{\partial \rho_a}{\partial t} = -\nabla \cdot (\rho_a q), \tag{3.13}$$

where ρ_a is the density of air. Since in the radon vessel experiments the pressure differences over the sand column are less than 40 Pa (0.04% of atmospheric pressure), the air can be considered incompressible, e.g. ρ_a is independent of p. Then, combining Eqs. (3.12) and (3.13), results in:

$$\nabla \cdot (k\nabla p) = 0. \tag{3.14}$$

Later, Eq. (3.14) will be used in the derivation of the time-dependent equations for radon transport. The bulk flux of radon activity $\vec{j_a}$ ($\mathrm{Bq\,m^{-2}\,s^{-1}}$) caused by advection is obtained by multiplying Eq. (3.12) with the radon activity concentration:

$$\vec{j_a} = C_a\vec{q} = -C_a\frac{k}{\mu}\nabla p. \tag{3.15}$$

3.4 Time-dependent equations for radon transport

The formulation as presented in this section is based in a large part on [An92b] and [An93].

It is assumed that the partition of radon between the gas phase, liquid phase and radon adsorbed on the solid phase of the pore space is permanently in equilibrium. From Henry's law we can write for the liquid-vapor partitioning:

$$C_w = LC_a, \tag{3.16}$$

where C_w (Bq m^{-3}) is the radon activity concentration in the liquid (water) phase and L is the Ostwald coefficient (dimensionless form of Henry's constant). L is 0.26 at 20°C. A table of L as function of temperature can be found in [An92b]. The amount of radon adsorbed on solid surfaces in pores is also linear proportional to the radon concentration in the gas phase:

$$C_s = k_a C_a, \tag{3.17}$$

where C_s (Bq kg^{-1}) is the adsorbed radon concentration and k_a (m^3 kg^{-1}) the radon surface-adsorption coefficient. This coefficient depends on soil type and moisture saturation. Data presented in [Ro91a] shows that adsorption is negligible for dry coarse sand, although values up to 1 for k_a were measured for sand with activated charcoal. Furthermore the adsorption coefficient will decrease with increasing moisture saturation [Ro91a].

We assume that transport of radon in the liquid phase over a distance larger than the grain size is negligible. Effectively this means that we take $D_w = 0$. This assumption is only valid when soil is only partly moisturised and most transport takes place in the gas phase. The derivation hereafter is not valid for soils having a high pore-water content. For these soils, the (spatial) distribution of gas and liquid phases in the pores and probably also the kinetics of the phase partitioning must be taken into account in the derivation of time-dependent equations for radon transport.

Consider a volume (V) of soil, much larger than the volume of soil grains, in which we have soil grains, pore water, pore gas and solid surfaces in the pores. We may write for the radon concentration in the water phase in the volume V:

$$\frac{V_w}{V}\frac{\partial C_w}{\partial t} = \frac{V_p}{V}S_w - \frac{V_w}{V}\lambda C_w, \tag{3.18}$$

which may be written as:

$$\epsilon_w \frac{\partial C_w}{\partial t} = \epsilon S_w - \epsilon_w \lambda C_w. \tag{3.19}$$

For radon adsorbed on solid surfaces we have:

$$\rho\frac{\partial C_s}{\partial t} = \epsilon S_s - \rho\lambda C_s, \tag{3.20}$$

where C_s is the adsorbed-radon concentration (Bq kg^{-1}). Finally for radon in the air-filled pore space we can write, using conservation of mass within the volume V:

$$\epsilon_a \frac{\partial C_a}{\partial t} = \epsilon S_a - \epsilon_a \lambda C_a - \nabla\cdot(\vec{j_d} + \vec{j_a}). \tag{3.21}$$

With Eqs. (3.8), (3.16) and (3.17), Eqs. (3.19), (3.20) and (3.21) can be combined into one equation for radon transport in the gas phase:

$$\beta\frac{\partial C_a}{\partial t} = \epsilon S - \beta\lambda C_a - \nabla\cdot\vec{j}, \tag{3.22}$$

where the quantity β is the partition-corrected porosity, defined as:

$$\beta = \epsilon_a + L\epsilon_w + \rho k_a, \tag{3.23}$$

and $\vec{j}$ (Bq m^{-2} s^{-1}) specifies the bulk radon-activity flux:

$$\vec{j} = \vec{j_a} + \vec{j_d} = -C_a \frac{k}{\mu} \nabla p - D \nabla C_a. \tag{3.24}$$

Thus, in full detail, Eq. (3.22) is written as, using Eq. (3.14):

$$\beta \frac{\partial C_a}{\partial t} = \epsilon S - \beta \lambda C_a + \frac{k}{\mu} \nabla p \cdot \nabla C_a + \nabla \cdot (D \nabla C_a). \tag{3.25}$$

If the soil is homogeneous and dry, and if adsorption may be neglected, Eq. (3.25) is simplified into:

$$\frac{\partial C_a}{\partial t} = S - \lambda C_a + \frac{k}{\epsilon \mu} \nabla p \cdot \nabla C_a + \nabla \cdot (D_e \nabla C_a). \tag{3.26}$$

Here we have introduced the effective diffusion coefficient D_e that can be written as:

$$D_e = \frac{D}{\epsilon} = \tau D_a. \tag{3.27}$$

Diffusion length

Another variable that is often used is the diffusion length of radon in soil. The physical meaning of this variable can best be elucidated with the following example.

Suppose we have a semi-finite column of dry (no adsorption), homogeneous sand and no pressure gradients inside the sand pores. Then, in one dimension and in equilibrium, Eq. (3.26) reduces to,

$$D_e \frac{d^2 C_a}{dz^2} - \lambda C_a + S = 0, \tag{3.28}$$

where z is the space variable. If the concentration at $z = 0$ is zero and the sand column extends from $z = 0$ to $z = \infty$, then the solution of this differential equation for $z \geq 0$ is:

$$C_a(z) = \frac{S}{\lambda} \left(1 - e^{(\frac{-z}{l})}\right), \tag{3.29}$$

where l is the diffusion length:

$$l = \sqrt{\frac{D_e}{\lambda}}. \tag{3.30}$$

The diffusion length is the characteristic distance travelled by the radon atoms during one half-life

Chapter 4

Analytical diffusion model

To interpret measurements of radon concentration as a function of time and height in the radon vessel, a model has to be available. In this chapter the solution of the time-dependent diffusion equation derived in the previous chapter with boundary conditions applicable to radon exhalation from dry, homogeneous porous materials will be discussed. In this analytical model the effect of a flow through the porous material is not taken into account and the effect of moisture is also not included. The latter can be introduced by means of using 'effective' coefficients in the differential equations [Ro91b]. The equations were solved by using Laplace-transformations.

4.1 Experimental set-up and boundary conditions

The one-dimensional analytical diffusion model can be applied to experimental set-ups that are comparable with the KVI radon vessel. Schematically Fig. 4.1 shows such a set-up, consisting of a soil column of height h inside a closed (besides for possible leakage at the top) cylinder leaving an air column of height d above the sand.

Diffusive radon transport in a dry and homogeneous soil is described by Eq. (3.26) without the advective term. In one dimension this is represented by

$$\frac{\partial C}{\partial t} = S - \lambda C + D_e \frac{\partial^2 C}{\partial z^2}, \tag{4.1}$$

where, for convenience, the notation C is used for the radon-activity concentration in the air space of a pore instead of C_a. To find a unique solution of Eq. (4.1), it necessary to apply two boundary conditions and one initial condition. The bottom of the vessel is impermeable for radon. This means there will be no radon flux at $z = 0$. The flux of radon is proportional to the concentration gradient (Eq. (3.10)). Consequently this results in the following boundary condition:

$$\frac{\partial C}{\partial z} = 0, \quad z = 0;\ t > 0. \tag{4.2}$$

There is a balance in the steady-state situation between the exhalation and the loss of activity due to decay and ventilation (leakage). If there is imbalance, the activity concentration at the interface ($z = h$) will change with time, according to the following boundary

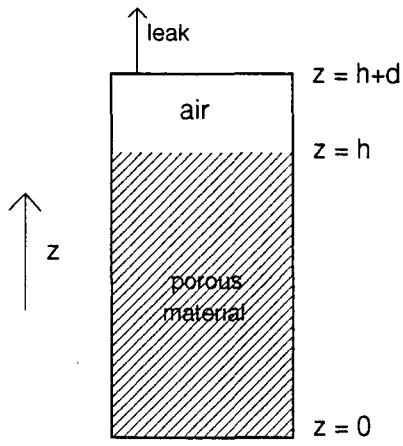

Figure 4.1: Schematic presentation of a radon vessel as used in the 1D analytical diffusion model.

condition

$$\frac{\partial C}{\partial t} = -\frac{\epsilon D_e}{d}\frac{\partial C}{\partial z} - (\lambda + \lambda_{leak})C, \quad z = h;\ t \geq 0. \tag{4.3}$$

Here we assume that the concentration just inside the pores of the material is the same as in the volume above the sand column (continuity condition) and that gas in this volume is completely mixed. As an initial condition, we have several possibilities. The first one that will be considered in Section 4.2 is

$$C = 0, \quad 0 \leq z \leq h;\ t = 0. \tag{4.4}$$

In Section 4.3 a solution will be given when C at $t = 0$ is equal to the equilibrium concentration with $d = \infty$. In that case we can write for the initial radon concentration:

$$C = \frac{S}{\lambda}\left(1 - \frac{\cosh(\frac{z}{l})}{\cosh(\frac{h}{l})}\right). \tag{4.5}$$

4.2 Solution when $C = 0$ at $t = 0$

The method of Laplace transformation (see [Cr56, p. 17-22]) is used to find the concentration as a function of time and height. Suppose $f(t)$ to be a known function of t for positive values of t. Then the Laplace transform $\overline{f}(p)$ of $f(t)$ is defined as

$$\overline{f}(p) = \int_0^\infty e^{-pt} f(t)dt, \tag{4.6}$$

where p is a number sufficiently large to make the integral (4.6) converge. The Laplace transform of the differential equation (4.1) is then

$$\int_0^\infty e^{-pt}\frac{\partial C}{\partial t}dt = D_e\int_0^\infty e^{-pt}\frac{\partial^2 C}{\partial z^2}dt - \lambda\int_0^\infty e^{-pt}C\,dt + \int_0^\infty e^{-pt}S\,dt. \tag{4.7}$$

Integrating the first term in Eq. (4.7) by parts we have

$$\int_0^\infty e^{-pt}\frac{\partial C}{\partial t}dt = \left[Ce^{-pt}\right]_0^\infty + p\int_0^\infty Ce^{-pt}dt = -C|_{t=0} + p\overline{C} = p\overline{C}, \tag{4.8}$$

since $C|_{t=0} = 0$ due to initial conditions. Further, if we assume that the order of differentiation and integration can be interchanged, we may write the second term in Eq. (4.7) as:

$$D_e\int_0^\infty e^{-pt}\frac{\partial^2 C}{\partial z^2}dt = D_e\frac{\partial^2}{\partial z^2}\int_0^\infty Ce^{-pt}dt = D_e\frac{d^2\overline{C}}{dz^2}. \tag{4.9}$$

The transform of the constant production rate S is

$$\int_0^\infty e^{-pt}S\,dt = \frac{S}{p}. \tag{4.10}$$

Using Eqs. (4.8), (4.9) and (4.10) in Eq. (4.7) we find

$$p\overline{C} = D_e\frac{d^2\overline{C}}{dz^2} - \lambda\overline{C} + \frac{S}{p}. \tag{4.11}$$

Similarly the transformed boundary conditions (4.2) and (4.3) are

$$\frac{d\overline{C}}{dz} = 0, \qquad z = 0, \tag{4.12}$$

and

$$p\overline{C} = -b\frac{d\overline{C}}{dz} - \lambda_i\overline{C}, \qquad z = h. \tag{4.13}$$

In which the dummy variables b and λ_i have been introduced as:

$$b = \frac{\epsilon D_e}{d}, \qquad \lambda_i = \lambda + \lambda_{leak}. \tag{4.14}$$

The general solution $\overline{C}$ of the differential equation (4.11) consists of the sum of a particular solution $\overline{C}_{\text{part}}$ and the solution $\overline{C}_{\text{hom}}$ of the homogeneous differential equation:

$$\overline{C} = \overline{C}_{\text{hom}} + \overline{C}_{\text{part}} = A\cos(kz) + B\sin(kz) + \frac{S}{p(p+\lambda)} \tag{4.15}$$

with

$$k^2 = -\frac{p+\lambda}{D_e}. \tag{4.16}$$

The variables A and B can be found from boundary conditions (4.12) and (4.13). After some algebra this gives

$$A = -\frac{S}{p(p+\lambda)(\cos(kh) - \frac{bk}{p+\lambda_i}\sin(kh))}; \quad B = 0. \tag{4.17}$$

So the solution of Eq. (4.11) is

$$\overline{C} = \frac{S}{p(p+\lambda)} - \frac{S\cos(kz)}{n(p)} \tag{4.18}$$

with

$$n(p) = p(p+\lambda)(\cos(kh) - \frac{bk}{p+\lambda_i}\sin(kh)). \tag{4.19}$$

The final step is to calculate the inverse transformation of $\overline{C}$. In general (see [Cr56, p .21]), it may be stated that if a transform $\overline{y}$ has the form

$$\overline{y} = \frac{f(p)}{g(p)}, \tag{4.20}$$

where $f(p)$ and $g(p)$ are polynomials in p which have no common factor, the degree of $f(p)$ being lower than that of $g(p)$, and if

$$g(p) = (p-a_1)(p-a_2)...(p-a_m), \tag{4.21}$$

where $a_1, a_2, ..., a_m$ are constants which may be real or complex but must all be different, then the function $y(t)$, which transform is $\overline{y}(p)$, is given by

$$y(t) = \sum_{r=1}^{m} \frac{f(a_r)}{g'(a_r)} e^{a_r t}. \tag{4.22}$$

Here $g'(a_r)$ denotes the value of $\frac{dg(p)}{dp}$ when $p = a_r$. Eq. (4.22) still holds for $m = \infty$. The justification of this assumption involves the theory of functions of a complex variable in order to carry out a contour integration and can be found in [Ca59].

Using Eq. (4.22) we find for the first term on the right-hand side of Eq. (4.18):

$$C_0 = \frac{S}{\lambda}\left(1 - e^{-\lambda t}\right). \tag{4.23}$$

The subscript j in the solutions C_j refers to the corresponding term of the series in Eq. (4.22). Since the solution (4.23) does not refer to a term in Eq. (4.22), the subscript 0 is used. The denominator $n(p)$ of the second term at the right-hand side of Eq. (4.18) can be written in a form given by Eq. (4.21) with an infinite number of factors, where $a_1 = 0$, $a_2 = -\lambda$ and $a_3 ...., a_\infty$ are the p's for which

$$\cos(kh) = \frac{bk\sin(kh)}{p+\lambda_i}. \tag{4.24}$$

Using Eq. (4.16) this can be written as

$$k\tan(kh) + \frac{D_e k^2 + \lambda - \lambda_i}{b} = 0. \tag{4.25}$$

The k and p values for which Eq. (4.25) is valid are denoted by k_r and p_r, $r = 3, 4, ..., \infty$. The subscripts 1 and 2 are for the roots of the first two terms of $n(p)$: $p_1 = 0$ and $p_2 = -\lambda$. From Eq. (4.24) it follows that Eq. (4.25) is only valid for $k \neq 0$ (when the top of the cylinder is open ($b = 0$, $d = \infty$), it is seen that the roots of Eq. (4.24) are $k_r = \frac{\pi}{h}(r - \frac{5}{2})$, $r = 3, 4...\infty$). This means that $n(p)$ only has a single root for $p = -\lambda$ ($k = 0$), originating from the factor $(p + \lambda)$. Also the negative values of k are not considered. This is related to the complex theory of inverse transformation and devolves on the requirement that p and k must have an injective relation (one to one correspondence). The requirement that the p values for which Eq. (4.25) is valid must all be different, may be checked grafically. The derivative of $n(p)$ with respect to p is given by

$$n'(p) = \frac{dn(p)}{dp} = \left(2p + \lambda + \frac{p(p+\lambda)bh}{2D_e(p+\lambda_i)}\right)\cos(kh) +$$

$$+ \left(-\frac{2bk}{p(p+\lambda_i)} + \frac{\lambda bk}{p(p+\lambda)(p+\lambda_i)} + \frac{h}{2D_e k} + \frac{b}{2D_e k(p+\lambda_i)} + \frac{bk}{(p+\lambda_i)^2}\right) \cdot \tag{4.26}$$

$$\cdot\, p(p+\lambda)\sin(kh).$$

To find C_j, $j = 1, ..., \infty$, it is necessary to calculate $n'(p_r)$, $r = 1, ..., \infty$. The solutions are, itemised for $r = 1$, $r = 2$, and $r \geq 3$:

- $r = 1$, $p_1 = 0$
  In this case $k_1 = \pm i\sqrt{\frac{\lambda}{D_e}} = \pm\frac{i}{l}$, where l is the diffusion length. The solution is

$$C_1 = -\frac{S}{\lambda}\left(\frac{\cosh(\frac{z}{l})}{\cosh(\frac{h}{l}) + \frac{\epsilon D_e}{l d \lambda_i}\sinh(\frac{h}{l})}\right). \tag{4.27}$$

- $r = 2$, $p_2 = -\lambda$
  Now $k_2 = 0$ and it appears that there are two solutions. One in the case that there is no leakage, i.e. $\lambda_i = \lambda$, and the other one when there is some leakage. (When $\lambda_i = \lambda$ we find the solution by taking the limit for $p \to -\lambda$ of Eq. (4.18), using Eq. (4.16)). We obtain

$$C_2 = \frac{S}{\lambda}\left(1 - \frac{\delta_{\lambda,\lambda_i}}{1 + \frac{d}{\epsilon h}}\right)e^{-\lambda t}. \tag{4.28}$$

  Physically, it may seem strange that the expression for C_2 changes dramatically when $\lambda_i = \lambda$. But also Eq. (4.31) changes completely when $\lambda_i = \lambda$. This is related to the *positive* roots of Eq. (4.25): The root close to $p = -\lambda$ (smallest k) will disappear when $\lambda_i = \lambda$. As a result the solution for $\lambda_i = \lambda + \epsilon$ with $\epsilon \to 0$ converges to the solution for $\lambda_i = \lambda$, which is required from a physical point of view.

- $r = 3, ..., \infty$

  As we only need to know $n'(p_r)$ when Eq. (4.25) is satisfied, we can rewrite Eq. (4.26) as

$$n'(p_r) = \frac{dn(p)}{dp}|_{p=p_r} =$$

$$p_r \left[\left(\frac{p_r + \lambda}{p_r + \lambda_i} \right) \left(1 + \frac{bh}{2D_e} \right) - \frac{h(p_r + \lambda_i)}{2b} - \frac{1}{2} \right] \cos(k_r h), \quad k_r > 0; \quad b > 0. \tag{4.29}$$

  The relation between k_r and p_r is given by Eq. (4.16):

$$k_r^2 = -\frac{p_r + \lambda}{D_e}, \tag{4.30}$$

  and the solution is given by

$$C_{\text{rest}} = -S \sum_{r=3}^{\infty} \frac{\cos(k_r z) e^{p_r t}}{n'(p_r)}. \tag{4.31}$$

  When the top of the cylinder is open ($b = 0$, $d = \infty$), Eq. (4.29) can not be used. In that case Eq. (4.26) must be used to find values of $n'(p_r)$.

4.2.1 Ultimate solution

The ultimate solution in the case that at $t = 0$ the radon concentration is 0, consists of the sum of Eqs. (4.23), (4.27), (4.28) and (4.31):

$$C = \frac{S}{\lambda} \left(1 - \frac{\cosh(\frac{z}{l})}{\cosh(\frac{h}{l}) + \frac{\epsilon D_e}{l d \lambda_i} \sinh(\frac{h}{l})} - \frac{e^{-\lambda t}}{1 + \frac{d}{\epsilon h}} \delta_{\lambda,\lambda_i} - \lambda \sum_{n=1}^{\infty} \frac{\cos(k_n z) e^{p_n t}}{n'(p_n)} \right), \tag{4.32}$$

where k_n are given by substituting Eq. (4.14) into Eq. (4.25), i.e. the positive roots of

$$k \tan(kh) + \frac{d(D_e k^2 - \lambda_{leak})}{\epsilon D_e} = 0, \tag{4.33}$$

and p_n is related to k_n by

$$p_n = -D_e k_n^2 - \lambda, \tag{4.34}$$

and $n'(p_n)$ is given by

$$n'(p_n) = p_n \left[\left(\frac{p_n + \lambda}{p_n + \lambda_i} \right) \left(1 + \frac{\epsilon h}{2d} \right) - \frac{dh(p_n + \lambda_i)}{2\epsilon D_e} - \frac{1}{2} \right] \cos(k_n h), \quad d \neq \infty. \tag{4.35}$$

In the case that $d = \infty$ we have the solution

$$C = \frac{S}{\lambda} \left(1 - \frac{\cosh(\frac{z}{l})}{\cosh(\frac{h}{l})} - \lambda \sum_{n=1}^{\infty} \frac{\cos(k_n z) e^{p_n t}}{n'(p_n)} \right) \tag{4.36}$$

with

$$k_n = \frac{\pi}{h} \left(n - \frac{1}{2} \right), \tag{4.37}$$

and p_n is related to k_n, given by Eq. (4.34).

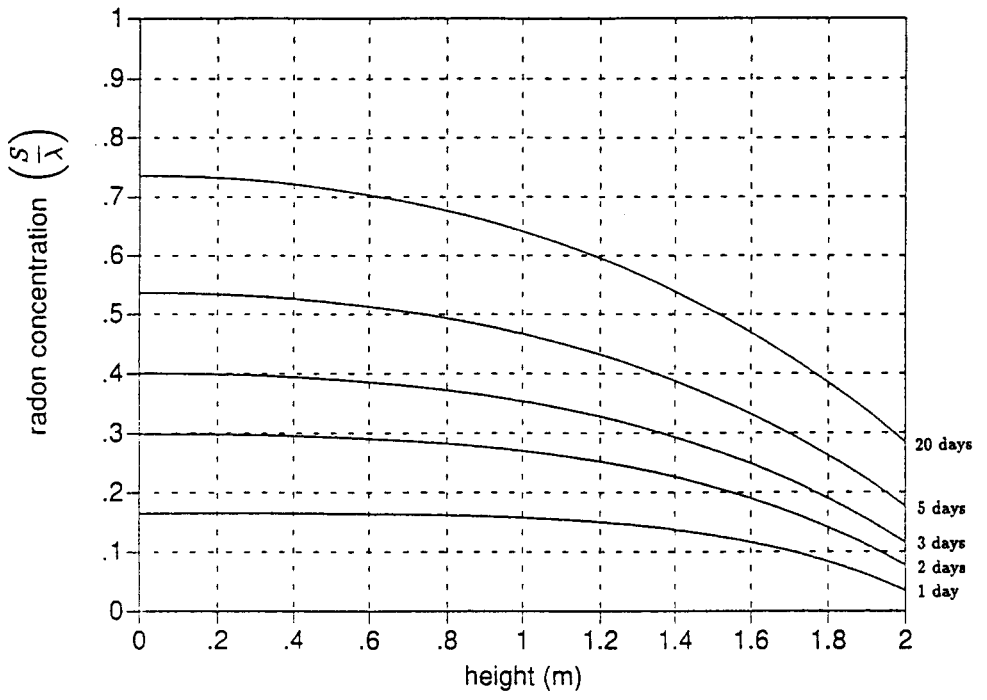

Figure 4.2: Radon profiles as function of height and time in the sand column given by Eq. (4.32), with $D_e = 3 \cdot 10^{-6}$ m^2 s^{-1}, $\epsilon = 0.36$, $d = 0.5$ m, $h = 2$ m, $\lambda = 2.1 \cdot 10^{-6}$ s^{-1} and $\lambda_i = 4.2 \cdot 10^{-6}$ s^{-1}. Radon concentration is in units $\frac{S}{\lambda}$. At $t = 0$ the radon concentration is 0. Radon profiles are given after 1, 2, 3, 5 and 20 days.

Fig. 4.2 shows radon profiles, calculated with Eq. (4.32), of a sand column with parameters (listed in the figure caption) that are reasonably in agreement with the quantities in the radon vessel experiments. For the effective diffusion coefficient $3 \cdot 10^{-6}$ m^2 s^{-1} is taken. Later, after the first radon vessel experiments, it became obvious that this was about a factor 3 smaller than the effective radon diffusion coefficient of the sand inside the vessel.

4.3 Solution when C at $t = 0$ is equal to the equilibrium concentration with $d = \infty$

In the case that $C|_{t=0} \neq 0$, according to Eq. (4.8), we obtain an extra term in the transformed differential equation (4.11):

$$-C(z)|_{t=0} + p\overline{C} = D_e \frac{d^2\overline{C}}{dz^2} - \lambda\overline{C} + \frac{S}{p}. \tag{4.38}$$

The boundary condition at $z = 0$ (Eq. (4.12)) remains unchanged, but the boundary condition at $z = h$ (Eq. (4.13)) changes to

$$-C(z)|_{t=0} + p\overline{C} = -b\frac{d\overline{C}}{dz} - \lambda_i\overline{C}, \qquad z = h;\ t > 0. \tag{4.39}$$

The solution is found similarly as in Section 4.2.

Suppose we have a material in equilibrium exhaling into free space ($d = \infty$) and that we enclose the sample at time $t = 0$, leaving an air space of height d above the top of the sand-column. The initial condition for the concentration distribution within the material is given by Eq. (4.36) in the equilibrium state ($t \to \infty$):

$$C(z)|_{t=0} = \frac{S}{\lambda}\left(1 - \frac{\cosh(\frac{z}{l})}{\cosh(\frac{h}{l})}\right). \tag{4.40}$$

The particular solution of Eq. (4.38) is given by

$$\overline{C}_{\text{part}} = \frac{S}{p\lambda}\left(1 - \frac{\cosh(\frac{z}{l})}{\cosh(\frac{h}{l})}\right). \tag{4.41}$$

Thus, in general, the solution is

$$\overline{C} = \overline{C}_{\text{hom}} + \overline{C}_{\text{part}} = A\cos(kz) + B\sin(kz) + \frac{S}{p\lambda}\left(1 - \frac{\cosh(\frac{z}{l})}{\cosh(\frac{h}{l})}\right). \tag{4.42}$$

The variables A and B can be found using the boundary conditions (4.12) and (4.39). After some algebra this gives

$$A = \frac{Sb\tanh(\frac{h}{l})}{p\lambda l((p+\lambda_i)\cos(kh) - bk\sin(kh))}; \qquad B = 0. \tag{4.43}$$

So the solution of Eq. (4.38) is

$$\overline{C} = \frac{S}{p\lambda}\left(1 - \frac{\cosh(\frac{z}{l})}{\cosh(\frac{h}{l})}\right) + \frac{\frac{Sb}{\lambda l}\tanh(\frac{h}{l})\cos(kz)}{n(p)} \tag{4.44}$$

with

$$n(p) = p((p+\lambda_i)\cos(kh) - bk\sin(kh)). \tag{4.45}$$

With Eq. 4.22 we find for the solution of the first term on the right-hand side of Eq. (4.44) ($p = 0$ is the only root):

$$C_0 = \frac{S}{\lambda}\left(1 - \frac{\cosh(\frac{z}{l})}{\cosh(\frac{h}{l})}\right). \tag{4.46}$$

The same as the initial condition. Note that from Eq. (4.43) it is seen that $A = 0$ when $b = 0$ ($d = \infty$). In that case Eq. (4.46) presents the final solution: the radon concentration does not change, as could be expected. This implies that the derivation hereafter is only valid for $b > 0$.

The zero's of $n(p)$ are: $p_1 = 0$, and the roots of Eq. (4.25), denoted by p_r, $r = 2, ..., \infty$. The derivative of $n(p)$ with respect to p is given by

$$n'(p) = \frac{dn(p)}{dp} = (2p + \lambda_i + \frac{pbh}{2D_e})\cos(kh) + \tag{4.47}$$

$$+ (-bk + \frac{ph(p+\lambda_i)}{2D_e k} + \frac{pb}{2D_e k})\sin(kh). \tag{4.48}$$

Thus we have the following cases:

- $r = 1$, $p = 0$.
  The solution is

$$C_1 = \frac{S}{\lambda}\left(\frac{\frac{b}{l\lambda_i}\tanh(\frac{h}{l})\cosh(\frac{z}{l})}{\cosh(\frac{h}{l}) + \frac{b}{l\lambda_i}\sinh(\frac{h}{l})}\right); \qquad b = \frac{\epsilon D_e}{d}. \tag{4.49}$$

- $r = 2, ..., \infty$; p is a root of Eq. (4.25) ($k > 0$).
  Now the solution is

$$C_{\text{rest}} = \frac{S}{\lambda}\frac{b}{l}\tanh(\frac{h}{l})\sum_{r=2}^{r=\infty}\frac{\cos(k_r z)e^{p_r t}}{n'(p_r)}, \tag{4.50}$$

  where $n'(p_r)$ is given by

$$n'(p_r) = \frac{dn(p)}{dp}|_{p=p_r} =$$

$$p_r\left[\left(\frac{p_r+\lambda_i}{p_r+\lambda}\right)\left(-\frac{1}{2} - \frac{h(p_r+\lambda_i)}{2b}\right) + 1 + \frac{bh}{2D_e}\right]\cos(k_r h), \qquad k_r > 0; \quad b > 0. \tag{4.51}$$

  The relation between k_r and p_r is given by Eq. (4.30).

There is however a special case when $\lambda_i = \lambda$. Then $p = -\lambda$ is a root of the denominater $n(p)$, and the limit for $p \to -\lambda$ (and $k \to 0$) must be taken of Eq. (4.47). When this is carried out, it will result in the following solution for $p = -\lambda$

$$C = -\frac{S}{\lambda}\left(\frac{\frac{b}{l\lambda}\tanh(\frac{h}{l})}{1 + \frac{\epsilon h}{d}}\right)e^{-\lambda t}. \tag{4.52}$$

At first sight it seems strange that only when $\lambda_i = \lambda$ this expression adds to the final solution. But examining the *positive* roots of Eq. (4.25) shows that the root close to $p = -\lambda$ (smallest k) will drop for $\lambda_i = \lambda$.

4.3.1 Ultimate solution

In summary, the solution for the radon concentration within the material in the case that at $t = 0$ the radon concentration is the equilibrium state with an infinit space above the material is the sum of Eqs. (4.46), (4.49), (4.50) (and Eq. (4.52) when $\lambda = \lambda_i$), which, after some rearranging gives:

$$C = \frac{S}{\lambda}\left(1 - \frac{\cosh(\frac{z}{l})}{\cosh(\frac{h}{l}) + \frac{\epsilon D_e}{ld\lambda_i}\sinh(\frac{h}{l})} - \frac{\frac{\epsilon D_e}{ld\lambda}\tanh(\frac{h}{l})e^{-\lambda t}}{1 + \frac{\epsilon h}{d}}\delta_{\lambda,\lambda_i} + \frac{\epsilon D_e}{ld}\tanh(\frac{h}{l})\sum_{n=1}^{\infty}\frac{\cos(k_n z)e^{p_n t}}{n'(p_n)}\right), \tag{4.53}$$

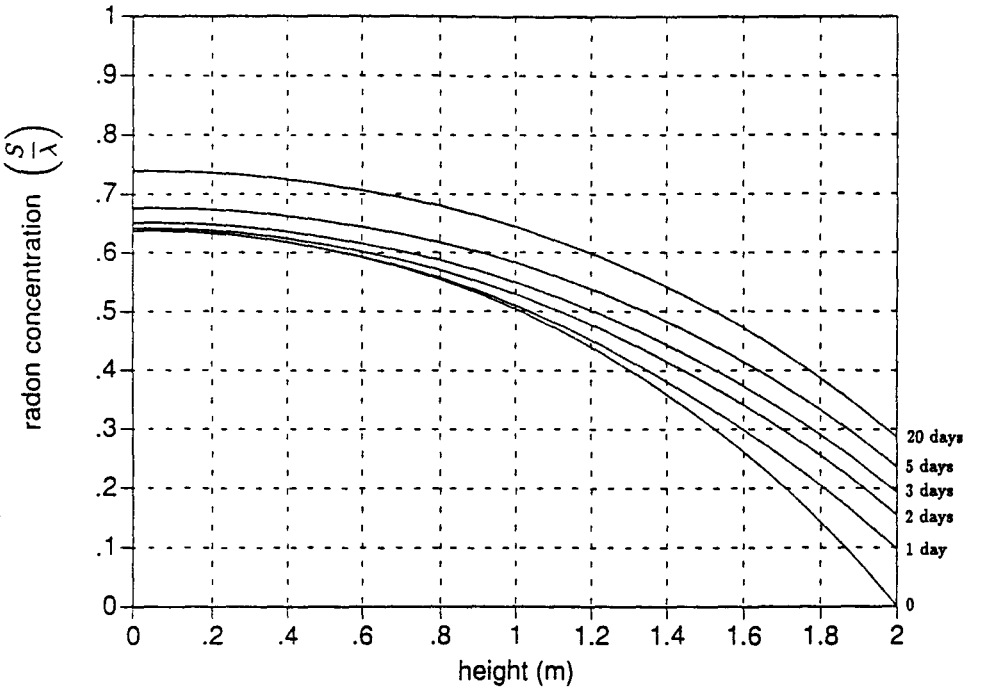

Figure 4.3: Radon profiles as function of height and time in the sand column given by Eq. (4.53), with $D_e = 3 \cdot 10^{-6}$ m^2 s^{-1}, $\epsilon = 0.36$, $d = 0.5$ m, $h = 2$ m, $\lambda = 2.1 \cdot 10^{-6}$s^{-1} and $\lambda_i = 4.2 \cdot 10^{-6}$ s^{-1}. Radon concentration is in units $\frac{S}{\lambda}$. At $t = 0$ the sand column is covered with a lid leaving an air column of 0.5 m above the sand, and the radon concentration profile is the equilibrium state with $d = \infty$. Profiles are given 1, 2, 3, 5 and 20 days after enclosure.

where k_n are the positive roots of

$$k \tan(kh) + \frac{d(D_e k^2 - \lambda_{leak})}{\epsilon D_e} = 0,$$

and p_n is related to k_n by

$$p_n = -D_e k_n^2 - \lambda,$$

and $n'(p_n)$ is given by

$$n'(p_n) = p_n \left[\left(\frac{p_n + \lambda_i}{p_n + \lambda} \right) \left(-\frac{1}{2} - \frac{hd(p_n + \lambda_i)}{2\epsilon D_e} \right) + 1 + \frac{\epsilon h}{2d} \right] \cos(k_n h), \quad b > 0. \qquad (4.54)$$

Fig. 4.3 shows radon profiles, calculated with Eq. (4.53), of a sand column with the same parameters as used to calculate the profile in Fig. 4.2. At $t = 0$ the sand column, previously in the equilibrium state, is enclosed, leaving an air space of height 0.5 m above the sand.

Chapter 5

Numerical method

5.1 Introduction

In the previous chapter an analytical solution for radon transport was derived for homogeneous soil without advection. However, measurements with the radon vessel under advective conditions have also been carried out so that a model that includes advection is needed to interpret these measurements. At the moment analytical solutions of the equilibrium state in case of combined advection and diffusion that treat the radon vessel *with the pressurebox* as a one-dimensional set-up are available.

In this chapter we will focus on a numerical method to solve the radon transport equation (Eq. (3.25)). The reason for this numerical approach is twofold:

1. Although analytical solutions provide more insight in the problem; the derivation can be very complex and minute. As a result it is limited to simple set-ups. Another consequence is that finding a solution for set-ups with position dependent variables, for example the diffusion coefficient or the partition-corrected porosity (Eq. (3.23)), is a non-trivial task.

2. Since in reality the radon vessel is a three-dimensional object, one and two dimensional solutions are only approximations of the real situation. But two-dimensional calculations are expected to represent the real situation in a better way. The numerical recipes presented in this chapter will be used in a 1D (chapter 6) and 2D (chapter 7) numerical method.

5.2 Method of finite differences

The numerical method used to solve the radon-transport equation is based on the finite-difference approach [An84]. In this approach, the continuous problem domain is 'discretised' so that the dependent variables are considered to exist only at discrete points. Derivatives are approximated by differences resulting in an algebraic representation of the partial differential equation (PDE).

One of the first steps to be taken is to replace the continuous problem domain by a finite-difference mesh or grid. Suppose we want to solve a PDE for which $U(x,t)$ is the dependent variable. Then the (x,t) plane will be divided in a two dimensional grid (j,n),

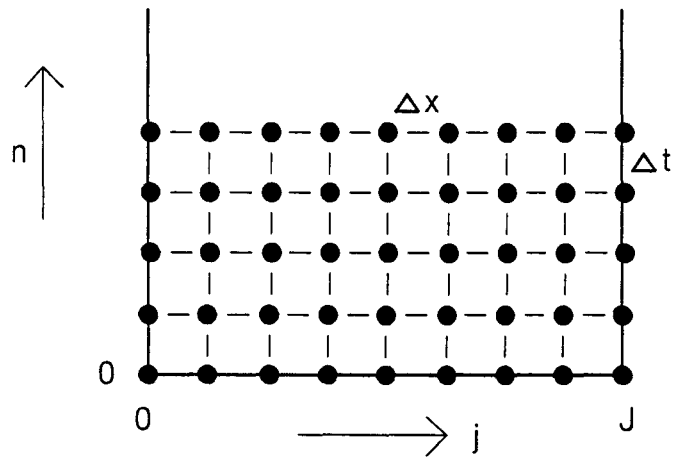

Figure 5.1: Finite-difference grid.

see Fig. 5.1, with $j = 0$ the left boundary and $j = J$ the right boundary; n refers to $t = n\Delta t$, $n \geq 0$. In this section we will assume that the grid spacing is uniform. Later, the appropriate equations are derived for a non-uniform grid that is used in the model. To each value of j corresponds a value x_j. Also, to each value of n corresponds a value t_n. Grid-spacings are Δx and Δt.

Further, we introduce the following shorthand notation:

$$U_{j+k}^{n+l} = U(x_j + k\Delta x, t_n + l\Delta t), \tag{5.1}$$

where k and l are integers. A Taylor-series expansion for $U(x_j + \Delta x, t_n)$ about $U(x_j, t_n)$ gives:

$$U(x_j + \Delta x, t_n) = U(x_j, t_n) + \frac{\partial U}{\partial x}|_{x_j,t_n}\Delta x + \frac{\partial^2 U}{\partial x^2}|_{x_j,t_n}\frac{(\Delta x)^2}{2} + \cdots. \tag{5.2}$$

From this we can form the 'forward' difference:

$$\frac{\partial U}{\partial x}|_{x_j,t_n} = \frac{U(x_j + \Delta x, t_n) - U(x_j, t_n)}{\Delta x} - \frac{\partial^2 U}{\partial x^2}|_{x_j,t_n}\frac{(\Delta x)}{2} + \cdots. \tag{5.3}$$

Switching now to the shorthand notation, we have

$$\frac{\partial U}{\partial x}|_{x_j,t_n} = \frac{U_{j+1}^n - U_j^n}{\Delta x} + O(\Delta x), \tag{5.4}$$

where we have used the order of (O) notation. Also the 'backward' difference can be found from the Taylor series expansion:

$$U(x_j - \Delta x, t_n) = U(x_j, t_n) - \frac{\partial U}{\partial x}|_{x_j,t_n}\Delta x + \frac{\partial^2 U}{\partial x^2}|_{x_j,t_n}\frac{(\Delta x)^2}{2} - \cdots, \tag{5.5}$$

giving:

$$\frac{\partial U}{\partial x}|_{x_j,t_n} = \frac{U_j^n - U_{j-1}^n}{\Delta x} + O(\Delta x). \tag{5.6}$$

We can substract Eq. (5.5) from Eq. (5.2) and obtain the 'central' difference:

$$\frac{\partial U}{\partial x}|_{x_j,t_n} = \frac{U_{j+1}^n - U_{j-1}^n}{2\Delta x} + O(\Delta x)^2. \tag{5.7}$$

We can also add Eq. (5.5) and Eq. (5.2) to obtain an approximation to the second derivative:

$$\frac{\partial^2 U}{\partial x^2}|_{x_j,t_n} = \frac{U_{j+1}^n - 2U_j^n + U_{j-1}^n}{(\Delta x)^2} + O(\Delta x)^2. \tag{5.8}$$

These types of finite differences could also have been made in the t-direction and it should be emphasized that in the above only a few examples were given of the possible ways in which first and second derivatives can be approximated.

It is convenient to utilise difference operators to represent finite differences. We have forward, backward and central operators for application in the first derivative:

$$\Delta_j U_j^n = U_{j+1}^n - U_j^n \quad \text{(forward)}, \tag{5.9}$$

$$\nabla_j U_j^n = U_j^n - U_{j-1}^n \quad \text{(backward)}, \tag{5.10}$$

$$\delta_j U_j^n = U_{j+1}^n - U_{j-1}^n \quad \text{(central)}. \tag{5.11}$$

For application in the second derivative we have:

$$\delta_j^2 U_j^n = \Delta_j U_j^n - \nabla_j U_j^n = U_{j+1}^n - 2U_j^n + U_{j-1}^n. \tag{5.12}$$

The operators defined in the above are used for spatial derivates. Similar difference operators for time derivates can be defined. For example the forward operator with respect to time is given by:

$$\Delta_n U_j^n = U_j^{n+1} - U_j^n. \tag{5.13}$$

5.3 Finite-difference schemes

In this section several finite-difference schemes for solving the diffusion equation and the advection equation will be discussed. Each scheme has its advantages and disadvantages. Based on these properties of difference schemes a most suitable method for the problem at hand can be chosen. This procedure is followed since the 2D-model is constructed in such a general way that each of the schemes contemplated hereafter can be applied. The flexibility of the 1D-model is somewhat less since the approach used in this model is somewhat different. (In the 1D-model we make use of the requirement of continuity of radon flux at each gridpoint. In doing so, it is not necesarry to apply special boundary conditions at interfaces between two different media.)

5.3.1 Finite-difference schemes for the diffusion equation

The explicit, implicit and an intermediate form of finite-difference presentations and their (dis)advantages will be presented.

Explicit method

In a finite-difference approach the diffusion equation (derived from Fick's law: $\vec{F} = -D\frac{\partial C}{\partial x}$ and using conservation of mass)

$$\frac{\partial U}{\partial t} = D\frac{\partial^2 U}{\partial x^2} \tag{5.14}$$

may be written as

$$\frac{\Delta_n U_j^n}{\Delta t} = D\frac{\delta_j^2 U_j^n}{(\Delta x)^2}. \tag{5.15}$$

If all U_j^n are known at any time t_n, Eq. (5.15) enables U_j^{n+1} to be calculated directly (that is, *explicitly*). Thereafter U_j^{n+2} can be calculated from U_j^{n+1} and so on. The advantage of this method is that programming is easy and computing times are short. A main disadvantage is that, using Eq. (5.15), this numerical method is only stable when $2D\Delta t \leq (\Delta x)^2$ [Ca69] (stability of finite-difference schemes is discussed in section 5.3.2). This means that if a a finer grid-spacing is choosen (Δx small, giving a better approximation of the PDE) the maximum allowed time step will be smaller too. In the case of a non-uniform grid, the maximum time step will be determined by the smallest Δx, which could result in a large computing time.

Another point of consideration is that the value U_j^n can only be influenced by $U_{j\pm1}^{n-1}$ and U_j^{n-1}. Physically U_j^n is determined from all U_j's at time level $n-1$.

Implicit method

The implicit method overcomes both these difficulties at the expense of a more complicated calculational procedure. It consists of representing the second derivative by a finite-difference form evaluated at the advanced point of time t_{n+1}, instead of t_n. The difference presentation of Eq. (5.14) then becomes

$$\frac{\Delta_n U_j^n}{\Delta t} = D\frac{\delta_j^2 U_j^{n+1}}{(\Delta x)^2}. \tag{5.16}$$

It is concluded [Ca69] that the implicit method is unconditionally stable, thus regardless the ratio of Δt and $(\Delta x)^2$. The disadvantage is that the value U_j^{n+1} can not be calculated directly. With the implicit method a number of linear equations (as much as grid points) has to be solved. Each equation (except at the boundaries) describes the relation between three adjacent points. As a consequence the matrix for this system of linear equations is tridiagonal, and Thomas algorithm (Appendix 1) is used to solve this system.

Intermediate implicit method

Both the explicit and implicit methods just described lead to truncation errors of $O[\Delta t + (\Delta x)^2]$. To obtain $O(\Delta t)^2$, we may write, using Eq. (5.7), for the derivative $\frac{\partial U}{\partial t}$ at the half-way point (j,n+$\frac{1}{2}$):

$$\frac{\partial U}{\partial t}|_{x_j, t_{n+\frac{1}{2}}} = \frac{U_j^{n+1} - U_j^n}{\Delta t} + O(\Delta t)^2. \tag{5.17}$$

For the approximation of the second derivative with respect to x a weighed mean at the time levels n and $n+1$ may be taken:

$$\frac{\partial^2 U}{\partial x^2}|_{x_j,t_{n+\theta}} = \frac{\theta\delta_j^2 U_j^{n+1} + (1-\theta)\delta_j^2 U_j^n}{(\Delta x)^2} + \cdots, \tag{5.18}$$

where the value θ is anywhere in the range $0 \leq \theta \leq 1$. The resulting finite-difference approximation is:

$$\frac{\Delta_n U_j^n}{\Delta t} = D\frac{\theta\delta_j^2 U_j^{n+1} + (1-\theta)\delta_j^2 U_j^n}{(\Delta x)^2}. \tag{5.19}$$

For $\theta = \frac{1}{2}$ we have the so called Crank-Nicolson Method (also referred to as 'time-centred'). With this method the truncation error is $O[(\Delta x)^2 + (\Delta t)^2]$. This is the only value of θ at which the approximation (5.19) is second-order accurate in time. (For some combinations of θ, D and grid spacing, the truncation error in space of Eq. (5.19) may be of fourth order or even of sixth order [An84]. However, since in the models a non-uniform grid is used, these combinations may only occur for some of the grid points). It can be shown that the discretisation scheme (5.19) is unconditionally stable for $\frac{1}{2} \leq \theta \leq 1$ [Ca69]. Note that for $\theta = 0$ we have the explicit scheme (5.15) and for $\theta = 1$ it is the same as the total implicit scheme (5.16). For $0 < \theta < \frac{1}{2}$ the explicit scheme dominates; a tridiagonal matrix must be solved and, for stability, the maximum allowed time step is limited.

To have a large flexibility, Eq. (5.19) is implemented in the 2D-model and the value θ can be chosen by the user. Considering the properties of the schemes discussed, it is recommended to apply a value of θ between $\frac{1}{2}$ and 1.

5.3.2 Finite-difference schemes for the advection equation

An advection equation is of the type

$$\frac{\partial U}{\partial t} + c\frac{\partial U}{\partial x} = 0; \qquad c > 0. \tag{5.20}$$

Eq. (5.20) describes a wave propagating in the positive x direction with a velocity c. There are numerous finite-difference schemes for this equation, but since in our problem we have combined diffusion and advection, the scheme describing advection ought to be 'compatible' with the scheme used for diffusion. This means for example that if a total implicit scheme is used to represent the diffusion of radon, the scheme for the advection of radon also has to be total implicit and vice versa. The only flexibility we have here is the finite-difference scheme of $\frac{\partial U}{\partial x}$. In section 5.2 three schemes were presented for the first derivative: the forward, backward and central finite-difference schemes (Eqs. (5.4), (5.6) and (5.7), respectively). In case the schemes give different solutions, the one that represents the real solution (of some known test case) the best may be prefered. To decide which scheme to take, some characteristics of finite-difference schemes will be outlined first. The terms discussed are stability, dissipation and dispersion.

Stability

The stability of a numerical method describes the growth of errors while computations are being performed. The type of stability analysis discussed is called Fourier or Neumann analysis [An84].

A numerical solution, at some time level n, can be regarded as the exact solution (which would be obtained with a computer with infinite accuracy, thus *not* the analytical solution) plus errors due to round-off. These round-off errors influence the solution at time level $n+1$; thus introduce extra errors at that time level. A stable scheme prevents these errors from growing during the computation steps whereas an unstable scheme does not have this property and the errors may grow larger, which eventually might blow up the solution.

Stability analysis of a finite-difference scheme is performed by substituting an initial solution in the scheme and calculate how much the solution will differ from this initial solution after one time step. The initial solution (in space) is assumed to be composed of waves with different frequencies. For example, if we have a grid with 5 grid points and the distance between the first and last grid point is L, then three waves are possible with wavelengths $2L$, L and $\frac{1}{2}L$. The analysis examines the growth of the amplitude of each of these waves and the results are lumped in the amplification factor G, which is the amplitude at the new time level divided by the amplitude at the initial time level as a function of the frequency of the initial wave. If the absolute value of the amplification factor for some frequency is larger than 1, the solutions (or errors) having this frequency will grow. On the other hand, if $G < 1$ for some frequency, the error will remain limited. The criterium for stability is that G must be equal or smaller than one and in general the amplification factor is a function of the frequency of the initial wave, of the grid spacing Δx, Δt and, in case of the advection equation, of c. Performing such an analysis for the finite-difference approximations of the advection equation with the three possible schemes for the first spatial derivative shows that a forward scheme is unstable (assumed that the grid on the x-axis is defined such that the grid-point index j changes positively in the positive x-direction). But if c would be smaller than 0, i.e. a wave propagating in the negative x-direction, a backward scheme is unstable. For this reason we speak about an upwind (or upstream) scheme when the first spatial derivative at point j involves the adjacent grid point from which the wave will propagate. Central and upwind schemes are stable, but still have different effects on the numerical solution. In order to judge which one is preferable under what circumstances, two other properties of finite-difference schemes will be discussed.

Dissipation and dispersion

All finite-difference schemes are approximations of the partial differential equation they represent and introduce a truncation error for which we used the order of (O) notation. These truncation errors actually exist of a number of terms with different derivatives. The consequence for the solution will be elucidated on the basis of one finite-difference approximation of the advection equation. Before giving this approximation, we return to the backward finite-difference scheme in space, Eq. (5.6), which can be written as:

$$\frac{U_j^n - U_{j-1}^n}{\Delta x} = \frac{\partial U}{\partial x}|_{x_j,t_n} - \frac{\partial^2 U}{\partial x^2}|_{x_j,t_n}\frac{(\Delta x)}{2} + \cdots. \tag{5.21}$$

In the same way the forward scheme for the time derivative can be written as:

$$\frac{U_j^{n+1} - U_j^n}{\Delta t} = \frac{\partial U}{\partial t}|_{x_j,t_n} + \frac{\partial^2 U}{\partial t^2}|_{x_j,t_n}\frac{(\Delta t)}{2} + \cdots. \tag{5.22}$$

The approximation of Eq. (5.20) with an explicit finite-difference scheme with backward differencing for the spatial derivative and forward differencing for the time derivative is:

$$\frac{U_j^{n+1} - U_j^n}{\Delta t} + c\frac{U_j^n - U_{j-1}^n}{\Delta x} = 0; \qquad c > 0. \tag{5.23}$$

Substitution of Eqs. (5.21) and (5.22) in Eq. (5.23) gives the equation that is solved *exactly* with this approximation:

$$\frac{\partial U}{\partial t} + c\frac{\partial U}{\partial x} = -\frac{\Delta t}{2}\frac{\partial^2 U}{\partial t^2}|_{x_j,t_n} + \frac{c\Delta x}{2}\frac{\partial^2 U}{\partial x^2}|_{x_j,t_n} + \cdots. \tag{5.24}$$

The left-hand side of this equation corresponds to the advection equation and the right-hand side is the truncation error which is generally not zero. The significance of terms in the truncation error can be more easily interpreted if the time derivative terms are replaced by spatial derivatives. To replace $\frac{\partial^2 U}{\partial t^2}$ by a spatial derivative term, we take the partial derivative of Eq. (5.24) with respect to time. The resulting expression is added to the expression obtained from taking the partial derivative of Eq. (5.24) with respect to x, multiplied by $-c$. The final result is:

$$\frac{\partial^2 U}{\partial t^2}|_{x_j,t_n} = c^2\frac{\partial^2 U}{\partial x^2}|_{x_j,t_n} + O[\Delta t + \Delta x]. \tag{5.25}$$

Substitution of this second derivative with respect to time in Eq. (5.24) gives

$$\frac{\partial U}{\partial t} + c\frac{\partial U}{\partial x} = \left(-\frac{c^2\Delta t}{2} + \frac{c\Delta x}{2}\right)\frac{\partial^2 U}{\partial x^2}|_{x_j,t_n} + \cdots. \tag{5.26}$$

This is the partial differential equation which is actually solved when the finite-difference method (Eq. (5.23)) is applied to the advection equation (5.20). The right-hand side of Eq. (5.26) is the truncation error (which contains second and higher-order terms, but the latter were not calculated precisely in the derivation above) since it represents the difference between the original PDE and the finite-difference approximation to it. The lowest-order term of the truncation error in the present case contains the partial derivative $\frac{\partial^2 U}{\partial x^2}$ which makes this term similar to damping (or diffusion, but this is confusing since the term 'diffusion' is also used for the combined effect of dissipation and dispersion, see further). Damping tends to reduce all gradients in the solution and the effect, which is the direct result of even derivative terms in the truncation error, is called *dissipation.* Another effect of numerical schemes is called *dispersion*, that is the direct result of the odd derivative terms which appear in the truncation error. As a result of dispersion, phase relations between various waves are distorted (the phase velocity of the waves is a function of frequency). For example if at $t = 0$ we have a block-form as initial condition (composed of waves with different frequencies), the advection equation describes that this block-form would travel undistorted with velocity c. A finite-difference scheme with mainly dispersion will show wiggles in the solution after some time-steps. If the scheme mainly shows dissipation, these wiggles will be smoothed as well as the whole solution. Figure 5.2 illustrates the effects of dissipation and dispersion on the computation of such a discontinuity.

A parameter frequently used in the analysis of the behaviour of finite-difference approximations of the advection equation is the Courant number ν:

$$\nu = c\frac{\Delta t}{\Delta x}. \tag{5.27}$$

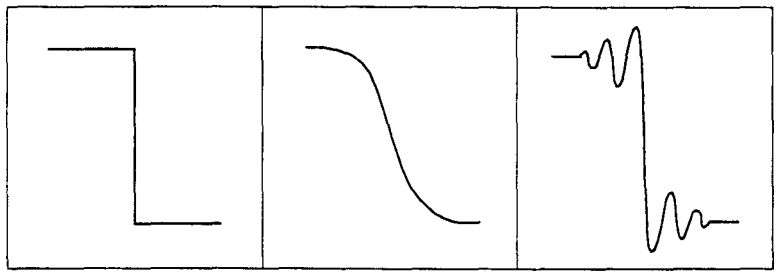

Figure 5.2: Effects of dissipation and dispersion. (a) Exact solution. (b) Numerical solution distorted by dissipation errors. (c) Numerical solution distorted by dispersion errors.

With reference to stability analysis, the amplification factor G is often written as function of (among other variables) the Courant number. Further, it is seen that the second-order term of the truncation error in Eq. (5.26) is zero when $\nu = 1$ (keeping track of higher-order terms reveals that these are all zero when $\nu = 1$ and the advection equation is solved exactly; but when the grid spacing is non-uniform, this will never occur since ν is not constant over the grid in that case). The amplification factor and the truncation error are related in the sense that dissipation corresponds to an amplification factor which is smaller than unity. A decrease of G is accompanied by an increase of the even derivative terms in the truncation error. Dispersion errors are not related to the magnitude of the amplification factor.

Properties of finite-difference approximations at hand for the advection equation

In the section on approximations of the diffusion equation, it was concluded that an implicit scheme is favourite above an explicit scheme, whether total implicit or time-centred. Therefore, since in our problem we deal with combined diffusion and advection, schemes with θ between $\frac{1}{2}$ and 1 are stable for the advective part of the partial differential equation. As a result, in principle, an infinite number of schemes is possible. In view of the stability criterium, only schemes with $\theta = \frac{1}{2}$ or 1 will be considered. Moreover, it was concluded in the former section that for the spatial derivative a central or upwind scheme ought to be used. The two possibilities for both time and space differencing, results in four finite-difference schemes for the advection equation.

In the following, the 4 possible schemes are itemised with, shortly, their specific properties. Extended information can be found in [An84]. In Chapter 7 we will discuss which scheme under what circumstances is preferable for our problem.

Implicit upwind: The discretisation scheme is

$$\frac{\Delta_n U_j^n}{\Delta t} + c\frac{\nabla_j U_j^{n+1}}{\Delta x} = 0; \qquad \text{error } O[\Delta x + \Delta t], \tag{5.28}$$

and the factor for the second space derivative in the truncation error is

$$\frac{c\Delta x}{2}(1+\nu).$$

From this it is seen that for large Courant numbers this method introduces a lot of dissipation. With respect to radon transport, the dissipation might be more than the physical diffusion. The amplification factor is close to 1 for very low wave numbers (this is valid for all schemes discussed) but decreases rapidly for higher wave numbers. At high Courant numbers the decrease of G is very fast.

In general, with respect to the behaviour of finite-difference schemes, the first term in the truncation error (in this case a second-order term) is dominating above the other terms. Expressions for the magnitude of third and higher-order terms can be found in [An84]

Time-centred upwind: The discretisation scheme is

$$\frac{\Delta_n U_j^n}{\Delta t} + c\frac{\nabla_j U_j^{n+1} + \nabla_j U_j^n}{2\Delta x} = 0; \qquad \text{error } O[\Delta x + (\Delta t)^2], \tag{5.29}$$

and the factor for the second space derivative in the truncation error is

$$\frac{c\Delta x}{2}.$$

Here the dissipation is independent of the time step (Courant number) applied in the numerical process. But still, a high velocity (c) might give much dissipation. The amplification factor does not differ much with the implicit upwind method. Only it will stay closer to unity for high Courant numbers.

Implicit space centred: The discretisation scheme is

$$\frac{\Delta_n U_j^n}{\Delta t} + c\frac{\delta_j U_j^{n+1}}{2\Delta x} = 0; \qquad \text{error } O[(\Delta x)^2 + \Delta t], \tag{5.30}$$

and the factor for the second space derivative in the truncation error is

$$\frac{1}{2}c^2\Delta t.$$

Depending on the velocity and time step, dissipation might be present. The amplification factor is close to unity for very low and very high wave numbers. For intermediate wave numbers and Courant numbers larger than 0.1, the amplification factor is small.

Time centred; space centred: The discretisation scheme is

$$\frac{\Delta_n U_j^n}{\Delta t} + c\frac{\delta_j U_j^{n+1} + \delta_j U_j^n}{4\Delta x} = 0; \qquad \text{error } O[(\Delta x)^2 + (\Delta t)^2], \tag{5.31}$$

In this case there is no even space derivative in the truncation error; the leading term contains a third derivative. The factor for this term is:

$$-\frac{c^3(\Delta t)^2}{12} - \frac{c(\Delta x)^2}{6}.$$

As a result this scheme has no dissipation, only dispersion. The amplification factor is 1 for all Courant numbers.

In this chapter we have shortly outlined the basics of the method of finite differences. In the next chapter, on the 1D-model, the numerical method is based mainly on the principles of finite-differences, but a slightly different approach is used to represent the governing PDE. Therefore, much of the characteristics of the schemes described above can not be applied directly to the 1D-method. On the other hand, in the 2D-model, schemes are applied that are nearly identical to the schemes discussed in this chapter. Consequently a discussion of what type of scheme to use, is left to Chapter 7 in which the 2D-model is presented.

Chapter 6

1D numerical model

In this chapter a finite-difference approximation of the one dimensional form of Eq. (3.25) is presented. After rearranging terms and using C instead of C_a for the radon concentration in the air filled part of a pore, this equation may be written as

$$\beta\frac{\partial C}{\partial t} = \frac{\partial}{\partial z}(D\frac{\partial C}{\partial z}) + \frac{k}{\mu}\frac{dp}{dz}\frac{\partial C}{\partial z} - \beta\lambda C + \epsilon S. \tag{6.1}$$

Solutions are found with appropriate boundary and initial conditions. To keep the applicability of the model as general as possible, soil parameters in Eq. (6.1): radon production term S ($\mathrm{Bq\,m^{-3}s^{-1}}$), permeability k ($\mathrm{m^2}$), partition corrected porosity β, porosity ϵ and bulk diffusion coefficient D ($\mathrm{m^2\,s^{-1}}$) need not be constant but may be functions of z.

6.1 Discretisation procedure

In Fig. 6.1 a schematic drawing of the radon vessel is shown. Schematically it is the same as used in the analytical diffusion model in Chapter 4, only with the pressure box added. For numerical calculations a grid was established on the domain $0 \leq z \leq h$ with only grid points in the area where soil is present. One grid point represents the whole pressure box. In Fig. 6.1 the grid spacing is uniform, but this is not a requirement; the 1D-model presented hereafter is also valid for a non-uniform grid. Each grid point is numbered using the counter j; $j = 0$ denotes the grid point at $z = 0$ and $j = J$ denotes the grid point at $z = h$. Consequently there are $J + 1$ grid points. Each volume containing soil between 2 adjacent grid points is parameterised by the soil parameters S, k, β, ϵ, D and the grid spacing Δz. This means that each of these volumes is homogeneous and as a result the soil parameters are also indexed. The soil parameters and the grid spacing for the volume between grid points j and $j + 1$ are indexed by j. For example D_5 corresponds to the diffusion coefficient for the soil between grid points 5 and 6. In the same way the grid spacing Δz_j is the distance between grid points j and $j + 1$.

On the other hand, the radon concentration C_j^n and the pressure P_j are calculated precisely at the position of the grid points; n is used to index the time step.

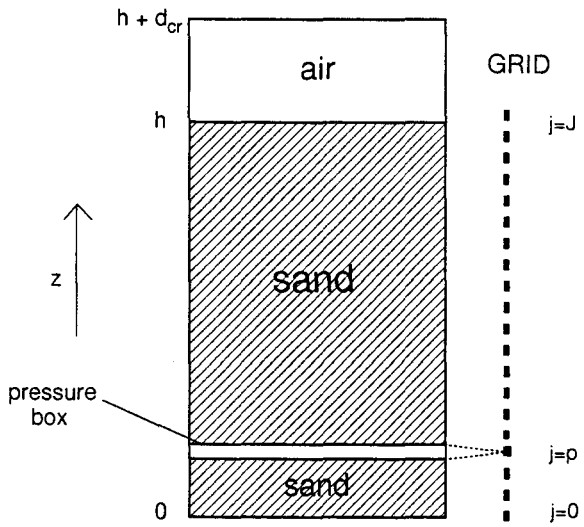

Figure 6.1: Schematic presentation of the radon vessel used in the 1D numerical model.

6.2 Finite-difference schemes

6.2.1 Calculation of the pressure field

The factor of the first spatial derivative in Eq. (6.1) contains the pressure gradient. Consequently, since the soil can be inhomogeneous, the pressure field must be calculated first. This is carried out using the 1D-form of Eq. (3.14):

$$\frac{d}{dz}\left(k\frac{dp}{dz}\right) = 0. \tag{6.2}$$

Notice that Eq. (6.2) states that the air flow $k\frac{dp}{dz}$ must be constant. Using this requirement, a finite-difference scheme for Eq. (6.2) is:

$$\frac{k_{j-1}(P_j - P_{j-1})}{\Delta z_{j-1}} - \frac{k_j(P_{j+1} - P_j)}{\Delta z_j} = 0. \tag{6.3}$$

The pressure is prescribed at the top of the pressure box and at $z = h$. At $z = 0$ there is no flow and we have $P_1 = P_0$. This system of equations is tridiagonal and the unknowns P_j are calculated with the Thomas algorithm (see Appendix).

6.2.2 Calculation of the radon concentration

In the derivation of the finite-difference scheme a slightly different approach is used than presented in Chapter 5. This approach is based on the requirement that the bulk radon flux must be continuous. With this method it is not needed to apply special finite-difference schemes at interfaces between two different media. (Each points it treated as a boundary between two media, also when soil parameters do not change).

Scheme for radon transport inside soil

Consider the grid points $j-1, j$ and $j+1$ with soil type A between the points $j-1$ and j and soil type B between points j and $j+1$. Then this continuity requirement implies the following condition for $t > 0$:

$$D_{j-1}\frac{\partial C}{\partial z}|_A = D_j\frac{\partial C}{\partial z}|_B. \tag{6.4}$$

Note that the bulk radon flux caused by advection ($Ck\nabla p$) is not involved in this equation since the calculation of the pressure field is based on the continuity of $k\nabla p$.

Further, for the diffusion term in Eq. (6.1) we can write for medium A using Taylor expansion:

$$D_{j-1}\frac{\partial^2 C}{\partial z^2}|_A = \frac{2D_{j-1}}{(\Delta z_{j-1})^2}\left(C_{j-1} - C_j + \Delta z_{j-1}\frac{\partial C}{\partial z}|_A\right) + O(\Delta z), \tag{6.5}$$

and for medium B:

$$D_j\frac{\partial^2 C}{\partial z^2}|_B = \frac{2D_j}{(\Delta z_j)^2}\left(C_{j+1} - C_j - \Delta z_j\frac{\partial C}{\partial z}|_B\right) + O(\Delta z). \tag{6.6}$$

With these equations and applying the general approach for the time differencing (comparable with Eq. (5.19)), we obtain for the finite-difference scheme of Eq. (6.1) in medium A:

$$\begin{aligned}\beta_{j-1}\frac{C_j^{n+1} - C_j^n}{\Delta t} &= \theta\frac{2D_{j-1}}{(\Delta z_{j-1})^2}\left(C_{j-1}^{n+1} - C_j^{n+1} + \Delta z_{j-1}\frac{\partial C}{\partial z}|_{A,t_{n+1}}\right)\\ &+(1-\theta)\frac{2D_{j-1}}{(\Delta z_{j-1})^2}\left(C_{j-1}^n - C_j^n + \Delta z_{j-1}\frac{\partial C}{\partial z}|_{A,t_n}\right) + \theta\frac{k_{j-1}}{\mu}\frac{\partial p}{\partial z}|_A\frac{\partial C}{\partial z}|_{A,t_{n+1}}\\ &+ (1-\theta)\frac{k_{j-1}}{\mu}\frac{\partial p}{\partial z}|_A\frac{\partial C}{\partial z}|_{A,t_n} - \theta\beta_{j-1}\lambda C_j^{n+1} - (1-\theta)\beta_{j-1}\lambda C_j^n + \epsilon_{j-1}S_{j-1}.\end{aligned} \tag{6.7}$$

In a similar way the finite-difference scheme in medium B is obtained:

$$\begin{aligned}\beta_j\frac{C_j^{n+1} - C_j^n}{\Delta t} &= \theta\frac{2D_j}{(\Delta z_j)^2}\left(C_{j+1}^{n+1} - C_j^{n+1} - \Delta z_j\frac{\partial C}{\partial z}|_{B,t_{n+1}}\right)\\ &+(1-\theta)\frac{2D_j}{(\Delta z_j)^2}\left(C_{j+1}^n - C_j^n - \Delta z_j\frac{\partial C}{\partial z}|_{B,t_n}\right) + \theta\frac{k_j}{\mu}\frac{\partial p}{\partial z}|_B\frac{\partial C}{\partial z}|_{B,t_{n+1}}\\ &+ (1-\theta)\frac{k_j}{\mu}\frac{\partial p}{\partial z}|_B\frac{\partial C}{\partial z}|_{B,t_n} - \theta\beta_j\lambda C_j^{n+1} - (1-\theta)\beta_j\lambda C_j^n + \epsilon_j S_j.\end{aligned} \tag{6.8}$$

These two schemes can be coupled by using the continuity of radon flux. For this purpose, since we are dealing with two time levels, Eq. (6.4) is rewritten such that both time levels are used:

$$D_{j-1}\left(\theta\frac{\partial C}{\partial z}|_{A,t_{n+1}} + (1-\theta)\frac{\partial C}{\partial z}|_{A,t_n}\right) = D_j\left(\theta\frac{\partial C}{\partial z}|_{B,t_{n+1}} + (1-\theta)\frac{\partial C}{\partial z}|_{B,t_n}\right). \tag{6.9}$$

By substituting for the two terms between brackets in Eq. (6.9), as can be obtained from Eqs. (6.7) and (6.8), the final result is:

$$C_j^{n+1}\left(\frac{D_{j-1}}{A_j}(\beta_{j-1}+\frac{\theta 2D_{j-1}\Delta t}{(\Delta z_{j-1})^2}+\theta\beta_{j-1}\lambda\Delta t)+\frac{D_j}{B_j}(\beta_j+\frac{\theta 2D_j\Delta t}{(\Delta z_j)^2}+\theta\beta_j\lambda\Delta t)\right)$$
$$+C_{j-1}^{n+1}\left(-\frac{D_{j-1}}{A_j}\frac{\theta 2D_{j-1}\Delta t}{(\Delta z_{j-1})^2}\right)+C_{j+1}^{n+1}\left(-\frac{D_j}{B_j}\frac{\theta 2D_j\Delta t}{(\Delta z_j)^2}\right)=$$
$$C_j^{n}\left(\frac{D_{j-1}}{A_j}(\beta_{j-1}-\frac{(1-\theta)2D_{j-1}\Delta t}{(\Delta z_{j-1})^2}-(1-\theta)\beta_{j-1}\lambda\Delta t)+\frac{D_j}{B_j}(\beta_j-\frac{(1-\theta)2D_j\Delta t}{(\Delta z_j)^2}-(1-\theta)\beta_j\lambda\Delta t)\right)$$
$$+C_{j-1}^{n}\left(\frac{D_{j-1}}{A_j}\frac{(1-\theta)2D_{j-1}\Delta t}{(\Delta z_{j-1})^2}\right)+C_{j+1}^{n}\left(\frac{D_j}{B_j}\frac{(1-\theta)2D_j\Delta t}{(\Delta z_j)^2}\right)$$
$$+\frac{D_{j-1}}{A_j}\epsilon_{j-1}S_{j-1}\Delta t+\frac{D_j}{B_j}\epsilon_j S_j\Delta t, \tag{6.10}$$

where the dummy variables A_j and B_j have been introduced:

$$A_j = 2D_{j-1}+\frac{k_{j-1}}{\mu}(P_j-P_{j-1}), \tag{6.11}$$

$$B_j = \frac{2D_j\Delta z_{j-1}}{\Delta z_j}-\frac{k_{j-1}}{\mu}(P_j-P_{j-1}). \tag{6.12}$$

All the variables at the right-hand side in Eq. (6.10) are known at a certain time t_n (At $t = 0$ initial values for the radon concentration must be given) and again we have an system of equations that is tridiagonal. The truncation error in Eq. (6.10) is $O(\Delta z)^2$ when grid spacing is uniform. From Eqs. (6.5) and (6.6) the truncation error might be expected to be first order in space, but keeping track of first-order errors during the derivation will show that these will cancel. Further, for $\theta = 0.5$, the truncation error in time is $O(\Delta t)^2$.

Scheme for the grid point representing the bottom of the vessel

The bottom of the vessel is impermeable for radon and a boundary condition must be applied for this grid point ($j = 0$). At this position we have no radon flux, or: $\frac{\partial C}{\partial z} = 0$. According to Eq. (6.6) we have the following approximation for the second derivative for $t > 0$:

$$D_0\frac{\partial^2 C}{\partial z^2} = \frac{2D_0}{(\Delta z_0)^2}(C_1-C_0)+O(\Delta z). \tag{6.13}$$

With this equation the finite-difference scheme is obtained directly from Eq. (6.1) without the advection term because, as was already discussed, there is also no air flow at the bottom. The result is:

$$C_0^{n+1}\left(\beta_0+\frac{2\theta D_0\Delta t}{(\Delta z_0)^2}+\theta\beta_0\lambda\Delta t\right)+C_1^{n+1}\left(-\frac{2\theta D_0\Delta t}{(\Delta z_0)^2}\right)=$$
$$C_0^{n}\left(\beta_0-\frac{2(1-\theta)D_0\Delta t}{(\Delta z_0)^2}-(1-\theta)\beta_0\lambda\Delta t\right)+C_1^{n}\left(+\frac{2(1-\theta)D_0\Delta t}{(\Delta z_0)^2}\right). \tag{6.14}$$

Disadvantage of this scheme is that the truncation error in space is $O(\Delta z)$. This is one of the two grid points having this property (the truncation error for the grid point that represents the pressure box is also first-order accurate) but the effect on the solution is likely to be small regarding the fact that the second spatial derivative of the solution at this position will be small.

Scheme for the grid point representing the pressure box

The pressure box is treated as a cavity in which the radon concentration is instantaneously mixed; the radon concentration is the same everywhere inside the box. For this reason the pressure box can be represented by one grid point. The change of radon concentration inside the box is determined by the rate at which the air flow enters and leaves the box, the radon concentration of the incoming air, radioactive decay of radon and fluxes caused by diffusion.

Suppose grid point j_p represents the pressure box and having medium B above the box and medium A under the box, then we have the following equation for the radon concentration inside the pressure box:

$$\frac{\partial C}{\partial t} d_{\text{box}} = f(C_0 - C) - \lambda d_{\text{box}} C - D_{j_p-1} \frac{\partial C}{\partial z}|_A + D_{j_p} \frac{\partial C}{\partial z}|_B, \tag{6.15}$$

where d_{box} (m) is the thickness of the pressure box, f (m s^{-1}) ($= \frac{k}{\mu}\frac{dp}{dz}$) the flow rate of the incoming and outgoing air, C_0 (Bq m^{-3}) the radon concentration of the incoming air and λ (s^{-1}) the decay constant of radon. The derivation of the finite-difference scheme for Eq. (6.15) is straightforward. Again using the general approach for the time differencing and replacing $\frac{\partial C}{\partial z}|_A$ by backward and $\frac{\partial C}{\partial z}|_B$ by forward finite differences (see Eqs. (5.6) and (5.4)) the final result is:

$$\begin{aligned}
&C_{j_p}^{n+1}\left(1 + \theta\Delta t\left(\frac{D_{j_p-1}}{d_{\text{box}}\Delta z_{j_p-1}} + \frac{D_{j_p}}{d_{\text{box}}\Delta z_{j_p}} + \frac{f}{d_{\text{box}}} + \lambda\right)\right) \\
&+C_{j_p-1}^{n+1}\left(-\frac{\theta\Delta t D_{j_p-1}}{d_{\text{box}}\Delta z_{j_p-1}}\right) + C_{j_p+1}^{n+1}\left(-\frac{\theta\Delta t D_{j_p}}{d_{\text{box}}\Delta z_{j_p}}\right) = \\
&C_{j_p}^{n}\left(1 - (1-\theta)\Delta t\left(\frac{D_{j_p-1}}{d_{\text{box}}\Delta z_{j_p-1}} + \frac{D_{j_p}}{d_{\text{box}}\Delta z_{j_p}} + \frac{f}{d_{\text{box}}} + \lambda\right)\right) \\
&+ C_{j_p-1}^{n}\left(\frac{(1-\theta)\Delta t D_{j_p-1}}{d_{\text{box}}\Delta z_{j_p-1}}\right) + C_{j_p+1}^{n}\left(\frac{(1-\theta)\Delta t D_{j_p}}{d_{\text{box}}\Delta z_{j_p}}\right) + \frac{C_0 f \Delta t}{d_{\text{box}}}.
\end{aligned} \tag{6.16}$$

Although this scheme involves three grid points, the truncation error in space is $O[\Delta z]$ since the first spatial derivative of the radon concentration at this grid point need not be continuous, especially when an air flow is induced. To obtain second-order accuracy a difference scheme that include more than three grid points is necessary. Disadvantage in that case is that the matrix that represents the system of linear equations in not tridiagonal. Extra calculations have to be performed in order to make the system tridiagonal after which Thomas algorithm can be used. Adaption of the programme for the 1D-model could be carried out. On the other hand the 2D-model, to be presented in the next chapter, gives a better representation of the real situation inside the radon vessel. For this reason improvement of the 1D-model was not a priority and adaptions were postponed.

Scheme for the grid point representing the surface of the soil column

At the top of the soil column in the radon vessel, radon can escape into the pseudo crawl space. For this cavity we have the boundary condition:

$$\frac{\partial C}{\partial t} d_{\text{cr}} = -\lambda_i d_{\text{cr}} C - D_{J-1} \frac{\partial C}{\partial z}|_A, \tag{6.17}$$

where d_{cr} (m) is the height of the crawl space, λ_i (s^{-1}) the decay constant of radon plus leakage of the crawl space and A is a reference to the soil at the surface. From Eq. (6.17) it is seen that the advective radon flux is not considered. This is due to the fact that the amount of radon that enters the crawl space is the same as the amount of radon that leaves the crawl space (both caused by advective fluxes only).

To maintain a second-order truncation error it is not allowed to use a simple 2-point backward difference scheme for the first derivative. This time a 3-point formula is used [An84]:

$$\frac{\partial C}{\partial z}|A = \frac{3C_J - 4C_{J-1} + C_{J-2}}{2\Delta z_{J-1}} + O(\Delta z)^2. \tag{6.18}$$

This equation is only valid when $\Delta z_{J-2} = \Delta z_{J-1}$ (program takes care of this) and when soil parameters do not vary in these last two grid spacings. With this approximation accurate in second order, the final result for point J is directly derived from the boundary condition Eq. (6.17):

$$\begin{aligned} C_J^{n+1}\left(1 + \frac{3\theta D_{J-1}\Delta t}{2d_{cr}\Delta z_{J-1}} + \theta\lambda_i\Delta t\right) \\ + C_{J-1}^{n+1}\left(-\frac{2\theta D_{J-1}\Delta t}{d_{cr}\Delta z_{J-1}}\right) + C_{J-2}^{n+1}\left(\frac{\theta D_{J-1}\Delta t}{2d_{cr}\Delta z_{J-1}}\right) = \\ C_J^{n}\left(1 - \frac{3(1-\theta) D_{J-1}\Delta t}{2d_{cr}\Delta z_{J-1}} - (1-\theta)\lambda_i\Delta t\right) \\ + C_{J-1}^{n}\left(\frac{2(1-\theta) D_{J-1}\Delta t}{d_{cr}\Delta z_{J-1}}\right) + C_{J-2}^{n}\left(-\frac{(1-\theta) D_{J-1}\Delta t}{2d_{cr}\Delta z_{J-1}}\right). \end{aligned} \tag{6.19}$$

This is the last equation in the whole system of linear equations that has to be solved. However, this system is not completely tridiagonal since the last equation describes a relation between C_J, C_{J-1} *and* C_{J-2}. Therefore, the last two equations in the system, i.e. the equations for grid point $J-1$ and J, are combined such that the first non-zero coefficient in the last row of the matrix that describes the system will become zero. Then the matrix is tridiagonal and again Thomas algorithm is used.

Some remarks concerning the use of these schemes

A peculiar point of interest is that for certain values of D, grid spacing and velocity of air ($\frac{k}{\mu}\frac{dp}{dz}$), the variables A_j or B_j in Eq. (6.10) can become zero or close to zero. This may cause a division by zero or overflow error during the computation. However, during our calculations this never occured and smallest values of A_j or B_j observed were in the order of 10^{-16} and did not stop the computation.

A useful parameter which arises when solving equations desribing combined diffusion and advection is the *mesh Reynolds number* defined by

$$\mathrm{Re}_{\Delta z} = \frac{c\Delta z}{D}, \tag{6.20}$$

where c is the velocity of the air flowing through the sand column. This non-dimensional parameter gives the ratio of advection to diffusion and is often refered to as the Peclet number. When $\mathrm{Re}_{\Delta z} > 1$ advection dominates above diffusion and the numerical behavior of the finite-difference scheme is mainly determined by the advective part.

In view of using this parameter it is seen that A_j or B_j can become exactly zero when $\mathrm{Re}_{\Delta z} = 2$. When this occurs Eq. (6.10) becomes, in principle, upwind. It is hard interpret the consequences for the numerical solution, especially because θ may be chosen anywhere between 0 and 1. Testing of the scheme showed that, using $\theta = 0.5$, the scheme produces oscillations when $\mathrm{Re}_{\Delta z} > 2$. These wiggles are physically not possible for radon transport and a requirement during the use of the models was that oscillations were not allowed, although the exact effect on the solution of small wiggles was not studied. These tests were carried with a block-form as initial profile for the radon concentration. The classification of this test can be called 'severe' since for radon transport such situations are not likely to occur. When $\theta = 1$, the scheme does not produce oscillations for any value of $\mathrm{Re}_{\Delta z}$. Although this is only the case when the air velocity is large, i.e. the dissipation makes the solution smooth. When air velocities are very low (no dissipation) and also the diffusion is very low (wiggles in the solution are not damped), the scheme with $\theta = 1$ also produces oscillations.

Considering the radon vessel experiments, where the air velocities are small (1 - 40 μm s^{-1}) and the diffusion coefficient is in the order of 10^{-6} - 10^{-5} $\mathrm{m}^2\,\mathrm{s}^{-1}$, there is actually no need to worry about computational oscillations in the solution.

6.3 Comparison with analytical solutions

Analytical solutions obtained with the method described in chapter 4 were compared with numerical solutions. These were the only time-dependent solutions available. When advection is present, only analytical solutions are available of the equilibrium state. These solutions were also compared.

6.3.1 Time-dependent diffusive radon transport

As mentioned before, the one-dimensional analytical model can be applied to experimental set-ups that are comparable with the radon vessel of which Fig. 4.1 is a schematical presentation. It consists of a sand column of height h inside a closed cilinder leaving an air column of height d above the sand. Only diffusive radon transport is modelled. At $t = 0$ the radon concentration is assumed to be 0. Fig. 4.2 shows radon profiles calculated with this analytical model. These profiles were also computed with the numerical method at several different grid spacings, time steps and values of θ. In Table 6.1 - 6.4 the deviation (per cent) from the analytical solution is presented.

Each table contains three groups of 4 rows. A group refers to one grid point in space. The upper group indicates the grid point at the bottom ($z = 0$ m), the middle group the central grid point ($z = 1$ m) and the last group the grid point at the top of the sand column ($z = 2$ m). The columns indicate the time and refer to 1, 2, 3, 5 and 20 days after $t = 0$. The rows in each group denote the time step at which the numerical calculation was carried out. Row 1 - 4 respectively indicate a time step of 10, 100, 10^3 and 10^4 seconds. The values in Table 6.1 are computed with a grid spacing of 0.01 m. The grid spacing for the values obtained in Table 6.3 is 0.02 m and in Table 6.4 it was 0.04 m. All values in these three tables are computed with $\theta = 0.5$. Table 6.2 gives values for $\theta = 1$ and grid spacing 0.01 m. From the data in these tables the following is concluded:

$\Delta z = 0.01$ m $\quad \theta = 0.5$					
Δt (s)	$T = 1$ day	$T = 2$ days	$T = 3$ days	$T = 5$ days	$T = 20$ days
at bottom					
10	0.00014	0.00038	0.00046	0.00049	0.00043
100	0.00014	0.00038	0.00046	0.00049	0.00043
1000	0.00018	0.00033	0.00040	0.00045	0.00043
10000	0.064	-0.0043	-0.0053	-0.0034	0.00021
in middle					
10	0.00093	0.00086	0.00080	0.00073	0.00059
100	0.000938	0.00086	0.00080	0.00073	0.00059
1000	0.00071	0.00077	0.00075	0.00070	0.00058
10000	-0.020	-0.0084	-0.0046	-0.0026	0.00036
at top					
10	0.015	0.0074	0.0049	0.0032	0.0019
100	0.016	0.0074	0.0049	0.0032	0.0019
1000	0.016	0.0074	0.0050	0.0032	0.0019
10000	0.078	0.015	0.0068	0.0013	0.0016

Table 6.1: Relative deviation ($\cdot 10^{-2}$) from analytical solution for $\Delta z = 0.01$ m and $\theta = 0.5$. Soil parameters and geometry as in Fig. 4.2. The positions bottom, middle and top correspond to $z = 0$, 1 and 2 m.

$\Delta z = 0.01$ m $\quad \theta = 1$					
Δt (s)	$T = 1$ day	$T = 2$ days	$T = 3$ days	$T = 5$ days	$T = 20$ days
at bottom					
10	0.0013	0.0016	0.0015	0.0012	0.00048
100	0.012	0.013	0.011	0.0078	0.00092
1000	0.12	0.12	0.10	0.073	0.0054
10000	1.13	1.17	1.01	0.71	0.050
in middle					
10	0.0026	0.0020	0.0017	0.0014	0.00063
100	0.018	0.012	0.010	0.0074	0.0010
1000	0.17	0.11	0.094	0.068	0.0056
10000	1.62	1.12	0.90	0.65	0.051
at top					
10	0.014	0.0079	0.0057	0.0040	0.0020
100	0.0087	0.013	0.013	0.011	0.0026
1000	0.051	0.069	0.090	0.086	0.0093
10000	0.58	0.60	0.82	0.80	0.076

Table 6.2: Relative deviation ($\cdot 10^{-2}$) from analytical solution for $\Delta z = 0.01$ m and $\theta = 1$. See also Table 6.1.

- The truncation error in space is practically $O(\Delta z)^2$. This can be seen by comparing the errors at different grid spacing at small time steps.
- According to theory the truncation error in time for $\theta = 0.5$ is $O(\Delta t)^2$. The data does not give a decisive answer. The overall truncation error is probably largely determined by the grid spacing. From data with $\theta = 1$ it is concluded that the truncation error in time is $O(\Delta t)$.
- The errors increase with increasing grid spacing and time step. As long as the ratio $\frac{D\Delta t}{(\Delta z)^2} <$ circa 30, the solution is hardly improved by decreasing the time step. A strange phenomenon is that at grid spacing $\Delta z = 0.04$ relatively good results are obtained with the largest time step (10^4 s).
- Using $\theta = 0.5$ gives better results than using $\theta = 1$.
- Errors are largest at the top of the sand column. This is not surprising since at that position the solution is most curved (second spatial derivative is largest at this position). Also at the top we see that the error decreases as function of time, while at the bottom it is more or less the reverse.
- Quantitatively it can be stated that, when using a grid spacing of 0.01 m and a time step smaller than 10^3 seconds, the relative error (with respect to the analytical solution) is smaller than $2 \cdot 10^{-4}$ for times in the order of one day, while at larger times, when the equilibrium state is almost reached, the relative errors are smaller than $2 \cdot 10^{-5}$. Such deviations are completely acceptable.

6.3.2 Advective and diffusive radon transport, equilibrium state

Analytical solutions of the equilibrium state for combined diffusive and advective radon transport are available [Va93d] for the set-up shown in Fig. 6.1 with no lid ($d_{cr} = \infty$). In Fig. 6.2 the radon profiles are presented for several air flows entering the pressure box. Solutions found with the numerical method almost exactly reproduce the solutions obtained with the analytical procedure. In Table 6.5 the deviation (per cent) between the analytical and numerical results are presented for several air flows at three different positions: at the bottom, in the pressure box and in the middle of the vessel. In these calculations the grid was not uniform; grid spacing varied from 0.1 mm near the bottom, the pressure box and the top of the sand column to 1 cm in the middle of the vessel. The total number of grid points was 234. From the data in Table 6.5 it is concluded that

- The numerical results deviate more for higher air flows, assuming that the analytical results are correct. There are some difficulties involved in the calculation of the radon concentrations in the analytical case. One of them is that a (small) system of equations must be solved *numerically.* Also, it was observed that an analytical solution could not be obtained for air velocities larger than approximately 20 μm s^{-1} (corresponding with a pressure in the pressure box of approximately 10 Pa and an air flow of 4 L min^{-1}).
- The highest mesh Reynold number is approximately 0.03 at the air flow of 1.6 L min^{-1}. Consequently diffusion is dominating over advection for all air flows tested.

$\Delta z = 0.02$ m $\quad \theta = 0.5$					
Δt (s)	$T = 1$ day	$T = 2$ days	$T = 3$ days	$T = 5$ days	$T = 20$ days
at bottom					
10	0.00055	0.0015	0.0018	0.0019	0.0017
100	0.00055	0.0015	0.0018	0.0019	0.0017
1000	0.00059	0.0014	0.0017	0.0019	0.0017
10000	0.0045	-0.0031	-0.0039	-0.0019	0.0014
in middle					
10	0.0036	0.0034	0.0031	0.0029	0.0023
100	0.0036	0.0034	0.0031	0.0029	0.0023
1000	0.0034	0.0033	0.0031	0.0028	0.0023
10000	-0.017	-0.0058	-0.0022	-0.00041	0.0021
at top					
10	0.061	0.029	0.019	0.012	0.0077
100	0.061	0.029	0.019	0.012	0.0077
1000	0.061	0.029	0.019	0.012	0.0077
10000	0.12	0.036	0.021	0.010	0.0073

Table 6.3: Relative deviation ($\cdot 10^{-2}$) from analytical solution for $\Delta z = 0.02$ m and $\theta = 0.5$. See also Table 6.1.

$\Delta z = 0.04$ m $\quad \theta = 0.5$					
Δt (s)	$T = 1$ day	$T = 2$ days	$T = 3$ days	$T = 5$ days	$T = 20$ days
at bottom					
10	0.0022	0.0059	0.0072	0.0077	0.0068
100	0.0022	0.0059	0.0072	0.0077	0.0068
1000	0.0022	0.0059	0.0072	0.0077	0.0068
10000	0.0061	0.0012	0.0015	0.0038	0.0066
in middle					
10	0.014	0.013	0.012	0.011	0.0092
100	0.014	0.013	0.012	0.011	0.0092
1000	0.014	0.013	0.012	0.011	0.0092
10000	-0.0064	0.0042	0.0072	0.0081	0.0090
at top					
10	0.24	0.11	0.077	0.050	0.030
100	0.24	0.11	0.077	0.050	0.030
1000	0.24	0.11	0.077	0.050	0.030
10000	0.30	0.12	0.079	0.048	0.030

Table 6.4: Relative deviation ($\cdot 10^{-2}$) from analytical solution for $\Delta z = 0.04$ m and $\theta = 0.5$. See also Table 6.1.

- Although a fine grid spacing was applied near the pressure box, still the highest errors occur at this position.
- Quantitatively it can be stated that the errors relative to the analytical solution are in the order of 10^{-5} - 10^{-4}. These errors are completely acceptable.

It was observed that, when using a uniform grid with grid spacing 1 cm, the deviation was about 3 percent. Especially refinement of the grid near the pressure box gives much better results. This is an indication that the truncation error in space for the grid point that represents the pressure box is larger than for the other points. Time step used during the computation was 3600 s and θ was 0.5. The equilibrium solution is not very sensitive to the magnitude of the time step (in fact, a time step of about 50 days immediately produces this solution). Also changing to $\theta = 1$ does not have a large influence. Extreme variations of the time step or applying values for θ between 0.5 and 1 introduce relative errors smaller than 0.02 percent (with the adapted non-uniform grid).

The largest air flow employed in the test is 1.6 L min^{-1}, but air flows up to 10^4 L min^{-1} are still possible to calculate with the numerical model. In Section 5.3.2 four different schemes for the advection equation were discussed. With $\theta = 0.5$ the advective part of the scheme (6.10) is (at very large flows) time centred and resembles the space centred scheme (only in the sense that it is certainly not upwind). Consequently, when advection is dominating, dispersive errors may blow up the solution. This is observed when using intermediate and small timesteps. At large timesteps this does not occur, but the solution is highly unstable and does not converge. On the other hand the solution is much more stable when $\theta = 1$ and when not too small time steps are used. But then dissipation is probably larger than the physical diffusion and the solution may not reflect the real situation.

Since these large air flows were not introduced in the radon vessel experiments, the main problem of the numerical model is the truncation error for the grid point that represents the pressure box. As already discussed, this can be solved by using a five-point scheme for this grid point. The time schedule for the present investigations did not allow to work this possibility out. The adaption of the program will probably be carried out in the future.

Another problem is that the air enters the pressure box in the centre, but leaves it through the whole area of the perforated plates. Thus the air flow inside the box will not only be in the z-direction. Radon is carried with this air flow from the central axis of the vessel. In order to model this a 2D-model is necessary, as discussed in the next chapter.

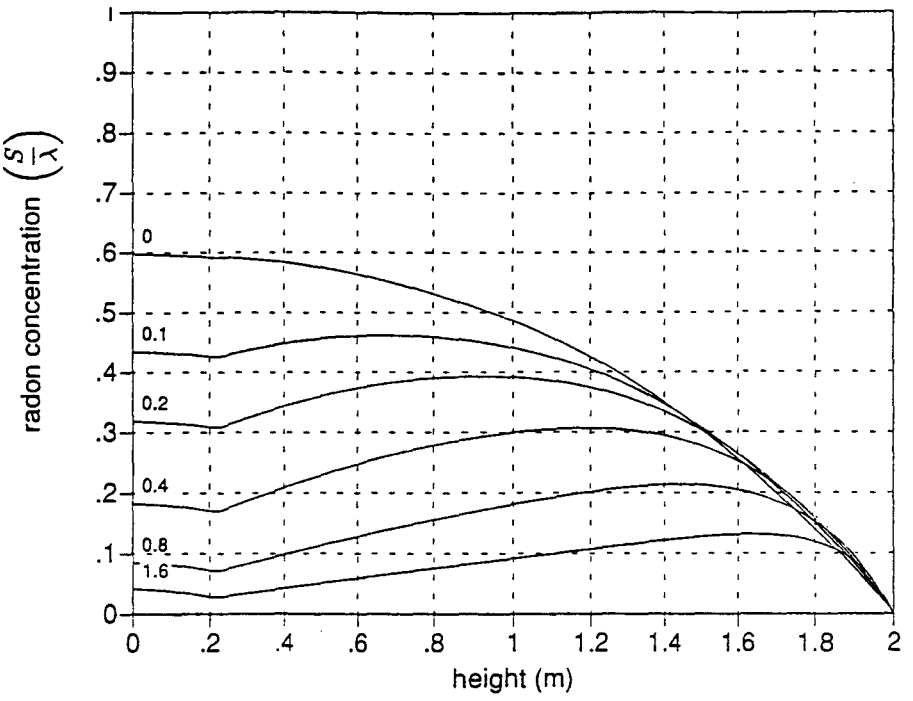

Figure 6.2: Radon profiles as function of height at several air flows entering the pressure box. Profiles are obtained from analytical or numerical solutions (both methods give almost the same results). Values for parameters used: $D_e = 3 \cdot 10^{-6}\ \mathrm{m^2\,s^{-1}}$, $\epsilon = 0.36$, $\beta = 0.36$, $d = \infty$, $h = 2$ m and $\lambda = 2.1 \cdot 10^{-6}\ \mathrm{s^{-1}}$. The pressure box is situated between $z = 0.2$ m and $z = 0.23$ m. Radon concentration is in units $\frac{S}{\lambda}$. Values at the profiles indicate the air flow in liters per minute.

air flow ($\mathrm{l\ min^{-1}}$)	at the bottom	in pressure box	in the middle
0	0.0044	0.0045	0.0026
0.1	0.0061	0.0063	0.0034
0.2	0.0069	0.0072	0.0033
0.4	0.0075	0.0080	0.0025
0.8	0.0090	0.010	0.0023
1.6	0.010	0.014	0.0040

Table 6.5: Percentual deviation of numerical solutions from analytical solutions. Most of the radon profiles tested are presented in Fig. 6.2.

Chapter 7

2D numerical model

In this chapter a 2D finite-difference model will be outlined, mainly based on difference schemes and techniques presented in Chapter 5. The 1D-model made use of the continuity of radon flux. Regarding extra difficulties accompaning the two-dimensional problem, it becomes more complicated to apply this method, which proved to give good results in the 1D-model. In the construction of the model the requirement of continuity is considered, but with this method restrictions are imposed on the scope of application of the model. These constraints, discussed in section 7.2.4 , are not severe but care must be taken when using the model. On the other hand it is not necessary to use the continuity of radon flux since the differential equation describing radon transport is derived based on this requirement. Therefore also finite-difference schemes are considered that directly represent this partial differential equation.

7.1 Discretisation procedure

In Fig. 7.1 a schematic drawing of the radon vessel is presented, as is used in the 2D numerical model. A grid is established on the domain $0 \leq z \leq h+d$, $0 \leq r \leq R$, where r denotes the distance from the central axis and R the radius of the vessel. Consequently we are dealing with a cylindrical coordinate system. As in the 1D-model, the grid spacing need not be uniform. Each grid point is numbered using the counters i and j. In the r-direction $i = 0$ denotes the grid point at $r = 0$ and $i = I$ refers to the grid point at $r = R$. In the z-direction $j = 0$ denotes the grid point at $z = 0$ and $j = J$ refers to the grid point at either $z = h$ (for example to model the radon vessel without the lid) or $z = h + d$. Each volume between two adjacent grid points is homogeneous and is parameterised by the radon production term, the partition corrected porosity, the porosity, the permeability, the bulk diffusion coefficient, the decay parameter (with possible leakage included in case that the grid points are situated in the pseudo crawl space) and the grid spacing, either Δz or Δr. Notice that these volumes have a rather strange form as indicated in Fig. 7.2. The parameters in each of these volumes are indexed by (i, j) and have an extra superscript z or r to indicate whether they apply to the volume between grid points (i, j) and $(i, j+1)$ or between grid points (i, j) and $(i+1, j)$, respectively. For example $D^r_{4,8}$ denotes the diffusion coefficient for the volume between grid points (4,8) and (5,8). In the same way the grid spacing Δz_j is the distance between grid points (i, j) and $(i, j+1)$. On the other

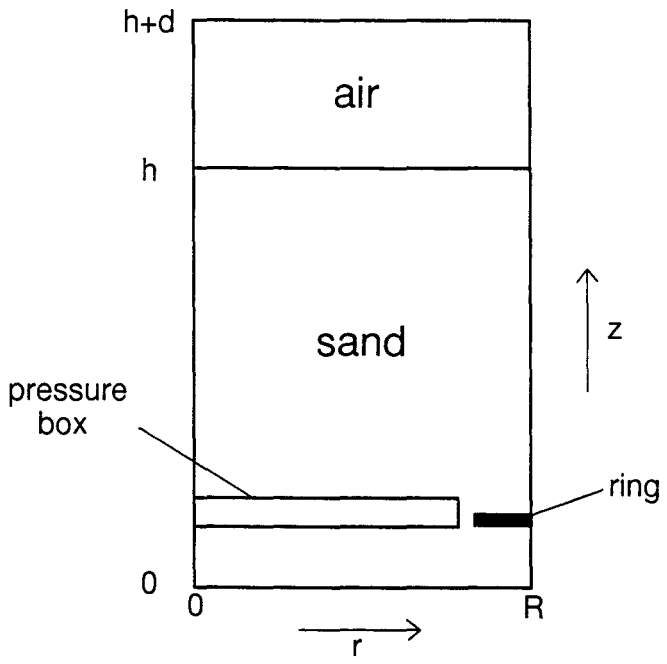

Figure 7.1: Schematic presentation of the radon vessel, used in the 2D numerical model.

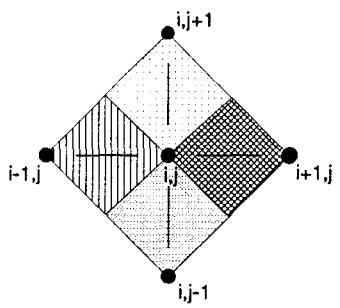

Figure 7.2: Part of the two-dimensional grid established on the r, z-plane presented in Fig. 7.1. Indicated are the volumes (rings around the central axis) between two adjacent points. The soil present in these volumes is taken to be homogeneous.

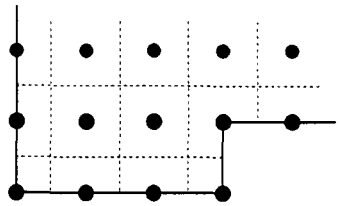

Figure 7.3: Finite-difference grid for the control volume method.

hand, the radon concentration $C^n_{i,j}$ and the pressure $P_{i,j}$ are calculated precisely at the position of the grid points; n is used to index the time step.

In contrast to the 1D-model, there are more than one grid points inside the pressure box and in the air volume above the top of the sand column. Both volumes are treated as a medium (like sand). Consequently, there are no special boundary conditions like Eqs. (6.15) and (6.17) for the pressure box and the air volume. The grid is set up such that grid points are also present precisely at boundaries between two media, at the geometric boundaries $z = 0, z = h + d$ (or $z = h$), $r = 0$, $r = R$ and at the boundaries of impermeable volumes. The ring and also the outer edge of the pressure box, that are metal objects, reflect such impermeable volumes. These objects are not treated as a medium, but boundary conditions are applied to the grid points at the surface.

7.2 Finite-difference schemes

7.2.1 Calculation of the pressure field

The pressure field is calculated using a so called control volume approach [An84] that is more accurate than other methods, especially near boundaries, because it keeps the discrete nature of the solution method in view at all times. In this approach the conservation statement is used instead of a Taylor-series expansion of the terms in the governing partial differential equation. The problem domain is divided in control volumes (rings around the central axis of the vessel) about each grid point. The boundaries of the control volumes (called interfaces) are established halfway between adjacent grid points, except at the geometric boundaries and the central axis, where the grid points are not 'inside' the control volume but are situated at the boundary itself, see Fig. 7.3. Considering the conservation of mass we can state that the amount of air that enters a control volume must be equal to the amount of air that leaves it. From Eq. (3.12) it is seen the air flux is proportional to $k\nabla p$. This equation is applied at the interfaces of a control volume by assuming that the pressure profile between two adjacent grid points is linear. By multiplying the flux with the area (m^2) represented by the interface, the air volume that leaves or enters the control volume through that specific interface is obtained. Summation of the air flows through each interface of one control volume must yield zero.

Consider a grid point (i, j) somewhere inside the problem domain. Then the area $A^{i+1,j}_{i,j}$

(m^2) represented by the interface between grid points (i,j) and $(i+1,j)$ is given by:

$$A_{i,j}^{i+1,j} = 2\pi(r_i + \frac{1}{2}\Delta r_i) \cdot \frac{1}{2}(\Delta z_{j-1} + \Delta z_j), \tag{7.1}$$

and the radial air flow $F_{i,j}^{i+1,j}$ ($m^3\ s^{-1}$) through this area is written as

$$F_{i,j}^{i+1,j} = \frac{k_{i,j}^r}{\mu}\left(\frac{P_{i+1,j} - P_{i,j}}{\Delta r_i}\right) A_{i,j}^{i+1,j}. \tag{7.2}$$

Proceeding in the same manner with the other three interfaces, summation of the four air flows and multiplying with $\frac{\mu}{\pi}$ finally results in:

$$\begin{aligned}
&P_{i-1,j}\left(k_{i-1,j}^r \frac{r_i - \frac{1}{2}\Delta r_{i-1}}{\Delta r_{i-1}}(\Delta z_{j-1} + \Delta z_j)\right) + P_{i+1,j}\left(k_{i,j}^r \frac{r_i + \frac{1}{2}\Delta r_i}{\Delta r_i}(\Delta z_{j-1} + \Delta z_j)\right) \\
&+ \left(P_{i,j-1}\frac{k_{i,j-1}^z}{\Delta z_{j-1}} + P_{i,j+1}\frac{k_{i,j}^z}{\Delta z_j}\right)\left(r_i(\Delta r_i + \Delta r_{i-1}) + \frac{1}{4}((\Delta r_i)^2 - (\Delta r_{i-1})^2)\right) \\
&- P_{i,j}\left(k_{i-1,j}^r \frac{r_i - \frac{1}{2}\Delta r_{i-1}}{\Delta r_{i-1}} + k_{i,j}^r \frac{r_i + \frac{1}{2}\Delta r_i}{\Delta r_i}\right)(\Delta z_{j-1} + \Delta z_j) \\
&- P_{i,j}\left(\frac{k_{i,j-1}^z}{\Delta z_{j-1}} + \frac{k_{i,j}^z}{\Delta z_j}\right)\left(r_i(\Delta r_i + \Delta r_{i-1}) + \frac{1}{4}((\Delta r_i)^2 - (\Delta r_{i-1})^2)\right) = 0.
\end{aligned} \tag{7.3}$$

The finite-difference scheme for grid points at the geometric boundaries or at the surface of an impermeable area is derived according to the same procedure. For those grid points the size of the surface of the interface between the control volumes will be different. For grid points where air enters the radon vessel, i.e. at the center ($r = 0$) of the pressure box, and where air leaves it, i.e. at the surface of the sand column (or at the top of the air column above the sand), the pressure is prescribed (is set at a constant value).

The system of equations obtained is no longer tridiagonal. Now each row of the matrix describing this system contains five non-zero elements and the matrix is said to be penta-diagonal. The diagonal does not contain zero elements. This system of equations is solved iteratively, using Gauss-Seidel iteration. This iteration procedure converges when [An84]

1. The sum of the four elements in a row that are not on the diagonal is smaller than or equal to the element on the diagonal in that row.

2. For at least one row this sum is smaller than the element on the diagonal.

For all rows in the matrix the first requirement is valid and the rows reflecting grid points for which the pressure is prescribed the only non-zero element is on the diagonal and the second requirement is satisfied. The procedure of Gauss-Seidel iteration consists of:

1. Making initial guesses for all unknows. (Starting with 0 for all unknows is allowed)

2. Solving each equation for the unknown whose coefficient is largest in magnitude (in this case that will be the unknown for the diagonal element), using guessed values initially and the most recently computed values for the unknows thereafter.

3. Repeating iteratively the solution of the equations in this manner until changes in the unknows become 'small'.

Mathematically the problem is expressed as

$$\begin{array}{lllll} a_{1,1}P_1+ & a_{1,2}P_2+ & \ldots\ldots\ldots & a_{1,n}P_n & = v_1 \\ a_{2,1}P_1+ & a_{2,2}P_2+ & \ldots\ldots\ldots & a_{1,n}P_n & = v_2 \\ \cdot & \cdot & & \cdot & \cdot \\ \cdot & \cdot & & \cdot & \cdot \\ \cdot & \cdot & & \cdot & \cdot \\ a_{n,1}P_1+ & a_{n,2}P_2+ & \ldots\ldots\ldots & a_{n,n}P_n & = v_n. \end{array} \tag{7.4}$$

In this system of equations, the pressure P has only one index (n) to indicate the grid point. Since $(I+1)*(J+1)$ grid points are present, this index for the pressure ranges from 0 to $(I+1)*(J+1)$. If we index the pressure row by row in the established grid and if we have 10 grid points in one row (r-direction), the only 5 non-zero elements in row k in system 7.4 are $a_{k,k}$, $a_{k,k\pm1}$ and $a_{k,k\pm10}$ (non-existing elements like $a_{1,-9}$ are assumed to be zero). The program-loop in pseudo-Pascal to solve this system using Gauss-Seidel could be

```
WHILE "some criterium" DO
   FOR k := 1 to n DO
      BEGIN
      New_Pk  := (v_k - a_{k,k-1} * P_{k-1} - a_{k,k+1} * P_{k+1}
                 -a_{k,k-10} * P_{k-10} - a_{k,k+10} * P_{k+10})/a_{k,k};
      P_k     := P_k + ω(New_Pk - P_k);
      END;
```

In this short loop the new value assigned to P_k is its old value plus a relaxation parameter ω multiplied with the change of P_k found with the Gauss-Seidel iteration step. If $\omega > 1$ this method is called successive over-relaxation and substantially speeds up the convergence rate. Optimal values for ω observed were about 1.95.

As a criterium to stop the iteration process, the sum of the absolute deviaton in the rows of system (7.4) is regarded. Mathematically it is expressed as

$$\text{total error} = \sum_{k=1}^{n} \left| v_k - \sum_{l=1}^{n} a_{k,l}\, P_l \right|. \tag{7.5}$$

Values of the total error used to stop the iteration process during model tests were approximately 10^{-10}. In these tests the grid contained about 2500 grid points.

7.2.2 Introduction of two space coordinates for time-dependent transport

Regarding only diffusive transport for the moment, it is possible to proceed in a similar way as was presented in Section 5.3.1, where Eq. (5.16) gives an implicit finite-difference scheme for one dimensional diffusion. Starting from this equation a simple two-dimensional scheme for diffusion in Cartesian coordinates and uniform grid would be

$$\frac{\Delta_n U^n_{i,j}}{\Delta t} = D\left(\frac{\delta_i^2 U^{n+1}_{i,j}}{(\Delta x)^2} + \frac{\delta_j^2 U^{n+1}_{i,j}}{(\Delta y)^2}\right). \tag{7.6}$$

Unfortunately, the resulting system of equations is no longer tridiagonal and for example Gauss-Seidel iteration is necessary to solve for each time-step. This would result in an enormous amount of computing time. For this reason it was decided to focus on the alternating-direction implicit (ADI) method. The principle is to employ two difference equations which are used in turn. The first step is a kind of prediction. In one direction the discretisation is implicit, in the other direction explicit. The second step interchanges both directions, i.e. the direction for which the discretisation was explicit (implicit) in the first step, is implicit (explicit) in the second step.

Staying with diffusive transport, a homogeneous medium, Cartesian coordinates and a uniform grid this two-step scheme, using the general intermediate implicit method (Eq. (5.19)), is given by

$$\text{step 1:}\quad \frac{\tilde{U}_{i,j}^{n+1}-U_{i,j}^{n}}{\Delta t} = D\left(\frac{\delta_i^2}{(\Delta x)^2}\left(\theta\tilde{U}_{i,j}^{n+1}+(1-\theta)U_{i,j}^{n}\right)+\frac{\delta_j^2 U_{i,j}^{n}}{(\Delta y)^2}\right), \tag{7.7}$$

$$\text{step 2:}\quad \frac{U_{i,j}^{n+1}-U_{i,j}^{n}}{\Delta t} = D\left(\frac{\delta_i^2}{(\Delta x)^2}\left(\theta\tilde{U}_{i,j}^{n+1}+(1-\theta)U_{i,j}^{n}\right)+\frac{\delta_j^2}{(\Delta y)^2}\left(\theta U_{i,j}^{n+1}+(1-\theta)U_{i,j}^{n}\right)\right). \tag{7.8}$$

The predicted values $\tilde{U}_{i,j}^{n+1}$, obtained with an implicit discretisation for the x-direction in the first ADI-step, are used again in the second ADI-step for an explicit discretisation in the same direction. This scheme is unconditionally stable and the truncation error is $O[(\Delta t)^2+(\Delta x)^2+(\Delta y)^2]$ [Ca69]. During Step 1, a tridiagonal matrix is solved for each row j of grid points and during Step 2, a tridiagonal matrix is solved for each i row of grid points.

Advection, decay and production of radon is simply introduced by adding the corresponding difference operators. For example the right-hand side of Eq. (7.7) becomes, using a central scheme for the first derivative:

$$\left(\frac{D\delta_i^2}{(\Delta x)^2}+\frac{c_x\delta_i}{\Delta x}-\lambda\right)\left(\theta\tilde{C}_{i,j}^{n+1}+(1-\theta)C_{i,j}^{n}\right)+\left(\frac{D\delta_j^2}{(\Delta y)^2}+\frac{c_y\delta_j}{\Delta y}\right)C_{i,j}^{n}+S_{i,j},$$

in which c_x and c_y are the air velocities in the x and y-direction. The expression for the second step is straightforward and does not introduce any difficulties.

7.2.3 Calculation of the radon concentration

Since the radon vessel is symmetric around its central axis, we must find a finite-difference scheme for the two-dimensional form of Eq. (3.25) in cylinder coordinates:

$$\beta\frac{\partial C}{\partial t}=\epsilon S-\beta\lambda C+\frac{k}{\mu}\left(\frac{\partial p}{\partial r}\frac{\partial C}{\partial r}+\frac{\partial p}{\partial z}\frac{\partial C}{\partial z}\right)+\frac{1}{r}\frac{\partial\left(rD\frac{\partial C}{\partial r}\right)}{\partial r}+\frac{\partial\left(D\frac{\partial C}{\partial z}\right)}{\partial z}, \tag{7.9}$$

where the ϕ-coordinate is omitted.

Schemes without using the continuity of radon flux

First, finite-difference schemes are considered that *directly* represent the partial differential equation (7.9). The schemes for the first three terms in Eq. (7.9) at grid point (i,j) are:

$$\beta\frac{\partial C}{\partial t} \approx \beta_{i,j}^{m}\frac{C_{i,j}^{n+1}-C_{i,j}^{n}}{\Delta t} \tag{7.10}$$

$$\epsilon S \approx \epsilon S^m_{i,j} \tag{7.11}$$

$$\beta\lambda C \approx \beta^m_{i,j}\lambda^m_{i,j}C_{i,j}. \tag{7.12}$$

In these schemes the index m refers to a weighed mean with respect to the grid spacing. For example:

$$S^m_{i,j} = \frac{\Delta z_j S^z_{i,j} + \Delta z_{j-1} S^z_{i,j-1}}{\Delta z_j + \Delta z_{j-1}}, \tag{7.13}$$

if the discretisation is in the z-direction. The same applies for the r-direction. With this method it is guaranteed that at a boundary between two media and with a non-uniform grid the correct amount of radon is produced (and decays). A disadvantage of this approach is that the production or decay does not take place exactly at the correct position.

The discretisation of the remaining terms in Eq. (7.9) yields:

$$\frac{k}{\mu}\frac{\partial p}{\partial r}\frac{\partial C}{\partial r} \approx F_r \cdot \left(\frac{\Delta r^\gamma_{i-1}\left(C_{i+1,j} - C_{i,j}\right)}{\Delta r_i\left(\Delta r^\gamma_i + \Delta r^\gamma_{i-1}\right)} + \frac{\Delta r^\gamma_i\left(C_{i,j} - C_{i-1,j}\right)}{\Delta r_{i-1}\left(\Delta r^\gamma_i + \Delta r^\gamma_{i-1}\right)} \right) = \delta_r C_{i,j} \tag{7.14}$$

$$\frac{k}{\mu}\frac{\partial p}{\partial z}\frac{\partial C}{\partial z} \approx F_z \cdot \left(\frac{\Delta z^\gamma_{j-1}\left(C_{i,j+1} - C_{i,j}\right)}{\Delta z_j\left(\Delta z^\gamma_j + \Delta z_{j-1}\right)} + \frac{\Delta z^\gamma_j\left(C_{i,j} - C_{i,j-1}\right)}{\Delta z_{j-1}\left(\Delta z^\gamma_j + \Delta z^\gamma_{j-1}\right)} \right) = \delta_z C_{i,j} \tag{7.15}$$

$$\begin{aligned} \frac{1}{r}\frac{\partial\left(rD\frac{\partial C}{\partial r}\right)}{\partial r} &\approx \frac{D^r_{i,j}\left(r_i + \frac{1}{2}\Delta r_i\right)\left(\frac{C_{i+1,j}-C_{i,j}}{\Delta r_i}\right) - D^r_{i-1,j}\left(r_i - \frac{1}{2}\Delta r_{i-1}\right)\left(\frac{C_{i,j}-C_{i-1,j}}{\Delta r_{i-1}}\right)}{r_i\frac{1}{2}\left(\Delta r_{i-1} + \Delta r_i\right)} \\ &= \delta^2_r C_{i,j} \end{aligned} \tag{7.16}$$

$$\frac{\partial\left(D\frac{\partial C}{\partial z}\right)}{\partial z} \approx \frac{D^z_{i,j}\left(\frac{C_{i,j+1}-C_{i,j}}{\Delta z_j}\right) - D^z_{i,j-1}\left(\frac{C_{i,j}-C_{i,j-1}}{\Delta z_{j-1}}\right)}{\frac{1}{2}\left(\Delta z_{j-1} + \Delta z_j\right)} = \delta^2_z C_{i,j}, \tag{7.17}$$

in which

$$F_r = \frac{1}{\mu}\left(\frac{k^r_{i,j}\Delta r_{i-1}\left(P_{i+1,j} - P_{i,j}\right)}{\Delta r_i\left(\Delta r_i + \Delta r_{i-1}\right)} + \frac{k^r_{i-1,j}\Delta r_i\left(P_{i,j} - P_{i-1,j}\right)}{\Delta r_{i-1}\left(\Delta r_i + \Delta r_{i-1}\right)} \right) \tag{7.18}$$

$$F_z = \frac{1}{\mu}\left(\frac{k^z_{i,j}\Delta z_{j-1}\left(P_{i,j+1} - P_{i,j}\right)}{\Delta z_j\left(\Delta z_j + \Delta z_{j-1}\right)} + \frac{k^z_{i,j-1}\Delta z_j\left(P_{i,j} - P_{i,j-1}\right)}{\Delta z_{j-1}\left(\Delta z_j + \Delta z_{j-1}\right)} \right) \tag{7.19}$$

$$\Delta r^\gamma_i = (1-\gamma_r)\Delta r_i \tag{7.20}$$

$$\Delta r^\gamma_{i-1} = \gamma_r \Delta r_{i-1} \tag{7.21}$$

$$\Delta z^\gamma_j = (1-\gamma_z)\Delta z_j \tag{7.22}$$

$$\Delta z^\gamma_{j-1} = \gamma_z \Delta z_{j-1} \tag{7.23}$$

$$\begin{aligned}
\gamma_r &= 1 - \frac{D^r_{i,j}}{\Delta r_i F_r} = 1 - \frac{1}{\mathrm{Re}_{\Delta r_i}} && \text{if } F_r > 0 \text{ and } \mathrm{Re}_{\Delta r_i} > 2 \\
&= -\frac{D^r_{i-1,j}}{\Delta r_{i-1} F_r} = -\frac{1}{\mathrm{Re}_{\Delta r_{i-1}}} && \text{if } F_r < 0 \text{ and } \mathrm{Re}_{\Delta r_{i-1}} < -2 \\
&= \frac{1}{2} && \text{if } -2 < \mathrm{Re}_{\Delta r} < 2 \\
\gamma_z &= 1 - \frac{D^z_{i,j}}{\Delta z_j F_z} = 1 - \frac{1}{\mathrm{Re}_{\Delta z_j}} && \text{if } F_z > 0 \text{ and } \mathrm{Re}_{\Delta z_j} > 2 \\
&= -\frac{D^z_{i,j-1}}{\Delta z_{j-1} F_z} = -\frac{1}{\mathrm{Re}_{\Delta z_{j-1}}} && \text{if } F_z < 0 \text{ and } \mathrm{Re}_{\Delta z_{j-1}} < -2 \\
&= \frac{1}{2} && -2 < \mathrm{Re}_{\Delta z} < 2.
\end{aligned} \tag{7.24}$$

In these equations the operators δ^2_r, δ_r, δ^2_z and δ_z have been defined and are convenient shorthand notations for the corresponding difference scheme. F_r and F_z respresent the approximated air flow (m s^{-1}) at point (i,j) in the r and z-direction, respectively. The parameters γ_r and γ_z (refered to as γ) can have values between 0 and 0.5, and play a

role when advection is dominating. This will be discussed later. Further notes considering these schemes:

- The difference scheme for first derivatives is, in first instance, without considering the effect of γ_r and γ_z, 'weighed' central. This means that a weighed mean is taken of the forward and backward differencing scheme. Most weight is given to the scheme with the smallest grid spacing. With this method a more accurate approximation is obtained.

- The air flows F_r and F_z are calculated with this same method. Although here we have the pre-knowledge that $k\nabla p$ is continuous and both terms at the right-hand side in Eqs. (7.18) and (7.19), apart from the weigh-factor, do not differ much.

- The term reflecting radial diffusion is written in the so called conservative form. The non-conservative form would be:

$$\frac{D}{r}\frac{\partial C}{\partial r} + \frac{\partial D}{\partial r}\frac{\partial C}{\partial r} + D\frac{\partial^2 C}{\partial r^2}.$$

  In [An84] it is discussed that a difference scheme based on the non-conservative form may lead to numerical difficulties in situations where the coefficients may be discontinuous. The same applies to the diffusion term in the z-direction.

- In Section 5.3.2 four finite-difference schemes for the advection equation were discussed. In the 2D-model, by varying γ and θ, it is possible to obtain all these four schemes with their different characteristics. The parameters γ_r and γ_z are used to vary the schemes for the first derivatives of the radon concentration from central to upwind. The amount of dissipation depends on the mesh Reynold number (or Peclet number, see Section 6.2.2), time step and on which scheme is being used. Dissipation, although unwanted, is necessary at high flow rates to avert oscillations which may even blow up the solution. As long as the absolute value of the Peclet number is smaller than 2, γ will be 0.5 and the schemes remain central. Diffusion is dominating and oscillations do not occur. If the Peclet number is larger than 2, γ is adapted such that the schemes will become more upwind. As a result these oscillations, observed for implicit as well as time-centred schemes, will be damped because of the dissipation accompaning upwind schemes. The formulas for γ_r and γ_z (Eq. (7.24)) are arbitrary. The consequence of taking these formulas is that the 'new mesh' Reynolds number will be exactly 2 and oscillations will just not occur.

In the model, the first step of the ADI-method is implicit in the r-direction, resulting in the final scheme:

$$\begin{aligned}
\text{step 1:}\quad \beta^m_{i,j}\frac{\tilde{C}^{n+1}_{i,j}-C^n_{i,j}}{\Delta t} &= \left(\delta_r^2+\delta_r-\beta^m_{i,j}\lambda^m_{i,j}\right)\left(\theta\tilde{C}^{n+1}_{i,j}+(1-\theta)C^n_{i,j}\right)\\
&\quad+\left(\delta_z^2+\delta_z\right)C^n_{i,j}+S^m_{i,j},\\
\text{step 2:}\quad \beta^m_{i,j}\frac{C^{n+1}_{i,j}-C^n_{i,j}}{\Delta t} &= \left(\delta_r^2+\delta_r\right)\left(\theta\tilde{C}^{n+1}_{i,j}+(1-\theta)C^n_{i,j}\right)\\
&\quad+\left(\delta_z^2+\delta_z-\beta^m_{i,j}\lambda^m_{i,j}\right)\left(\theta C^{n+1}_{i,j}+(1-\theta)C^n_{i,j}\right)+S^m_{i,j}.
\end{aligned} \tag{7.25}$$

Notice that in these two steps the m-index has two different meanings. In the first ADI-step it concerns a weighed mean in the r-direction, whereas in the second ADI-step a weighed mean is taken in the z-direction (see discussion at Eq. (7.13)).

Schemes using the continuity of radon flux

In this section the finite-difference schemes will be discussed based on the requirement that the radon flux must be continuous. Consequently this method largely resembles the method used in the 1D numerical model. However, in the two-dimensional case difficulties arise how to employ this requirement. We only found an approximate method how to deal with the continuity of radon flux. (Actually the appropriate procedure would be to add the four radon fluxes for one control volume surrounding a grid point and add production and decay of radon, which gives an expression for the rate of change of the radon concentration $\frac{\partial C}{\partial t}$ within this volume. The operator splitting is applied in a similar way as discussed before. However, it was decided to focus on the Taylor-series method mainly because this method is described extensively in literature for time-dependent problems.)

Change of soil parameters in the z-direction

In the case that soil parameters *only* differ in one direction, let us say the z-direction, a difference scheme is derived based on the requirement that the radon flux caused by diffusion is continuous in this direction. Physically, this is a reasonable assumption since the diffusive flux in the r-direction will be continuous because soil parameters do not change in that direction. This means that we do not have to consider the four fluxes surrounding a grid point, but only the two fluxes in the z-direction because the two fluxes in the r-direction will cancel (opposite signs). Thus, if there is a change in soil parameters from medium A^z to medium B^z only in the z-direction, we have the boundary condition during step 1 of the ADI procedure:

$$D^z_{i,j-1}\frac{\partial C}{\partial z}|_{A^z,t_n} = D^z_{i,j}\frac{\partial C}{\partial z}|_{B^z,t_n}. \tag{7.26}$$

In a similar way as was presented in Section 6.2.2, expressions can be obtained for $\frac{\partial C}{\partial z}|_{A^z,t_n}$ and $\frac{\partial C}{\partial z}|_{B^z,t_n}$. Although here, in the first ADI-step, we must add the normal finite-difference schemes for the r-direction to these expressions. So, the expression for $\frac{\partial C}{\partial z}|_{A^z,t_n}$ is found from:

$$\beta^z_{i,j-1}\frac{\tilde{C}^{n+1}_{i,j} - C^n_{i,j}}{\Delta t} = \left(\delta_r^2 + \delta_r - \beta^z_{i,j-1}\lambda^z_{i,j-1}\right)\left(\theta\tilde{C}^{n+1}_{i,j} + (1-\theta)C^n_{i,j}\right)$$
$$+ \frac{2D^z_{i,j-1}}{(\Delta z_{j-1})^2}\left(C^n_{i,j-1} - C^n_j + \Delta z_{j-1}\frac{\partial C}{\partial z}|_{A^z,t_n}\right) + F_z\frac{\partial C}{\partial z}|_{A^z,t_n} + S^z_{i,j-1}, \tag{7.27}$$

and the expression for $\frac{\partial C}{\partial z}|_{B,t_n}$ is obtained from:

$$\beta^z_{i,j}\frac{\tilde{C}^{n+1}_{i,j} - C^n_{i,j}}{\Delta t} = \left(\delta_r^2 + \delta_r - \beta^z_{i,j}\lambda^z_{i,j}\right)\left(\theta\tilde{C}^{n+1}_{i,j} + (1-\theta)C^n_{i,j}\right)$$
$$+ \frac{2D^z_{i,j}}{(\Delta z_{j-1})^2}\left(C^n_{i,j+1} - C^n_j - \Delta z_j\frac{\partial C}{\partial z}|_{B^z,t_n}\right) + F_z\frac{\partial C}{\partial z}|_{B^z,t_n} + S^z_{i,j}. \tag{7.28}$$

Substitution of Eqs. (7.27) and (7.28) in the boundary condition Eq. (7.26) gives the finite-difference scheme for the first ADI-step for grid point (i,j). Note that there are also special schemes for boundary points. For example at the edge of the vessel (r=R), the radon flux in the r-direction must be zero. In that case a Taylor-series expansion is carried out that includes the boundary point and the adjacent grid point in the r-direction with the pre-knowledge that $\frac{\partial C}{\partial r} = 0$. The further derivation of the scheme is similar to the method described above.

In the second step of the ADI procedure, which is implicit in the z-direction, we make use of the boundary condition with a weighed mean of the two time levels (similar to Eq. (6.9)):

$$D^z_{i,j-1}\left(\theta\frac{\partial C}{\partial z}|_{A^z,t_{n+1}} + (1-\theta)\frac{\partial C}{\partial z}|_{A^z,t_n}\right) = D^z_{i,j}\left(\theta\frac{\partial C}{\partial z}|_{B^z,t_{n+1}} + (1-\theta)\frac{\partial C}{\partial z}|_{B^z,t_n}\right). \tag{7.29}$$

Again, the expressions for the terms between brackets is found with similar procedures. For example the first term is obtained from:

$$\begin{aligned}\beta^z_{i,j-1}\frac{C^{n+1}_{i,j} - C^n_{i,j}}{\Delta t} &= \left(\delta_r^2 + \delta_r\right)\left(\theta\tilde{C}^{n+1}_{i,j} + (1-\theta)C^n_{i,j}\right)\\ &+\theta\left(\frac{2D^z_{i,j-1}}{(\Delta z_{j-1})^2}\left(C^{n+1}_{i,j-1} - C^{n+1}_{i,j} + \Delta z_{j-1}\frac{\partial C}{\partial z}|_{A^z,t_{n+1}}\right) + F_z\frac{\partial C}{\partial z}|_{A^z,t_{n+1}}\right)\\ &+(1-\theta)\left(\frac{2D^z_{i,j-1}}{(\Delta z_{j-1})^2}\left(C^n_{i,j-1} - C^n_{i,j} + \Delta z_{j-1}\frac{\partial C}{\partial z}|_{A^z,t_n}\right) + F_z\frac{\partial C}{\partial z}|_{A^z,t_n}\right)\\ &- \beta^z_{i,j-1}\lambda^z_{i,j-1}\left(\theta C^{n+1}_{i,j} + (1-\theta)C^n_{i,j}\right) + S^z_{i,j-1}.\end{aligned} \tag{7.30}$$

Change of soil parameters in the r-direction

If there is a change in soil parameters (from medium A^r to medium B^r) in the r-direction, we start with the non-conservative form of the radial diffusion term in homogeneous soil:

$$\frac{1}{r}\frac{\partial\left(rD\frac{\partial C}{\partial r}\right)}{\partial r} = \frac{D}{r}\frac{\partial C}{\partial r} + D\frac{\partial^2 C}{\partial r^2}. \tag{7.31}$$

The term $\frac{\partial D}{\partial r}\frac{\partial C}{\partial r}$ disappears since the Taylor-series expansion is in medium A^r *or* B^r, i.e. we deal with a homogeneous soil volume. The boundary condition during both ADI-steps is:

$$D^r_{i-1,j}\left(\theta\frac{\partial \tilde{C}}{\partial r}|_{A^r,t_{n+1}} + (1-\theta)\frac{\partial C}{\partial r}|_{A^r,t_n}\right) = D^r_{i,j}\left(\theta\frac{\partial \tilde{C}}{\partial r}|_{B^r,t_{n+1}} + (1-\theta)\frac{\partial C}{\partial r}|_{B^r,t_n}\right). \tag{7.32}$$

The expression for the first term between brackets (the one for the second term is found with a similar procedure) in the first ADI-step is obtained from:

$$\beta^r_{i-1,j}\frac{\tilde{C}^{n+1}_{i,j} - C^n_{i,j}}{\Delta t} = \left(\delta_z^2 + \delta_z\right)C^n_{i,j}$$

$$+\theta\left(\frac{2D^r_{i-1,j}}{(\Delta r_{i-1})^2}\left(\tilde{C}^{n+1}_{i-1,j}-\tilde{C}^{n+1}_{i,j}+\Delta r_{i-1}\frac{\partial\tilde{C}}{\partial r}|_{A^r,t_{n+1}}\right)+F_r\frac{\partial\tilde{C}}{\partial r}|_{A^r,t_{n+1}}\right)$$

$$+(1-\theta)\left(\frac{2D^r_{i-1,j}}{(\Delta r_{i-1})^2}\left(C^n_{i-1,j}-C^n_{i,j}+\Delta r_{i-1}\frac{\partial C}{\partial r}|_{A^r,t_n}\right)+F_r\frac{\partial C}{\partial r}|_{A^r,t_n}\right)$$

$$-\beta^r_{i-1,j}\lambda^r_{i-1,j}\left(\theta\tilde{C}^{n+1}_{i,j}+(1-\theta)C^n_{i,j}\right)+S^r_{i-1,j}, \tag{7.33}$$

and in the second ADI-step the expression for the first term between brackets in Eq. (7.32) is obtained from:

$$\beta^r_{i-1,j}\frac{C^{n+1}_{i,j}-C^n_{i,j}}{\Delta t}=\left(\delta_z^2+\delta_z-\beta^r_{i-1,j}\lambda^r_{i-1,j}\right)\left(C^{n+1}_{i,j}+C^n_{i,j}\right)$$

$$+\theta\left(\frac{2D^r_{i-1,j}}{(\Delta r_{i-1})^2}\left(\tilde{C}^{n+1}_{i-1,j}-\tilde{C}^{n+1}_{i,j}+\Delta r_{i-1}\frac{\partial\tilde{C}}{\partial r}|_{A^r,t_{n+1}}\right)+F_r\frac{\partial\tilde{C}}{\partial r}|_{A^r,t_{n+1}}\right)$$

$$+(1-\theta)\left(\frac{2D^r_{i-1,j}}{(\Delta r_{i-1})^2}\left(C^n_{i-1,j}-C^n_{i,j}+\Delta r_{i-1}\frac{\partial C}{\partial r}|_{A^r,t_n}\right)+F_r\frac{\partial C}{\partial r}|_{A^r,t_n}\right)+S^r_{i-1,j}. \tag{7.34}$$

This completes the derivation of the finite-difference scheme in which the continuity of radon flux is being applied. Final finite-difference schemes have not been given, mainly because the derivation is straightforward.

Treatment of the boundary points

At impermeable boundaries we demand that the radon flux in the direction perpendicular to this boundary must be zero, mathematically expressed as $\frac{\partial C}{\partial z}=0$ or $\frac{\partial C}{\partial r}=0$. The Taylor expansion contains two grid points for this direction and consequently the truncation error is $O(\Delta z)$ or $O(\Delta r)$. At corners we have $\frac{\partial C}{\partial r}=0$ and $\frac{\partial C}{\partial z}=0$. The central axis ($r=0$) is treated as an impermeable boundary in the r-direction. At this position we assume that $\frac{D}{r}\frac{\partial C}{\partial r}=0$, although actually a singularity is introduced by the radius r in the denominator. Further we assume that the grid points situated at angular points (at the corner) of an impermeable object can be regarded as normal grid points, having an adjacent grid point in each direction. The latter procedure is only an approximation of the real situation and it was observed in some tests that it may lead to errors if advective transport is dominating at those grid points.

7.2.4 General remarks concerning the use of the 2D-schemes

1. The question arises whether to use the scheme that describes the PDE directly (method 1) or the scheme that is derived based on the continuity of radon flux (method 2). There are two points for attention concerning the second method:

   - The second method can not be used if soil parameters change in both directions at a certain grid point (i,j). During initialisation of the model, care must be taken to avoid the presence of such grid points.
   - Essentially, the differencing scheme for the first derivative is (similar to) central and it is not possible to change it into an upwind scheme. Therefore, oscillations may occur when the Peclet number is larger than 2.

When diffusion is dominating (Peclet number smaller than 2), tests have shown that:

(a) Both methods are identical when soil parameters only vary in the z-direction.

(b) The solution of the two methods slightly differ (relative error in the order of 10^{-4}) when soil parameters vary in the r-direction. This is probably related to the extra term $\frac{D}{r}\frac{\partial C}{\partial r}$ for radial diffusion and to the absence of the term $D\frac{\partial C}{\partial r}$ at time level $n+1$ in the boundary condition Eq. (7.32) (i.e. the condition of continuity of diffusive flux only includes the old and predicted situation; not the final situation after one time step).

From this we can draw the following conclusions:

- The affirming results of both methods is an indication that they are correct.
- It is a matter of taste which method to use as long as the Peclet (mesh Reynolds) number is smaller than two.
- It is recommended not to use the second method when the Peclet number is larger than 2 (at that particular grid point).

2. When advective transport dominates, we have an upwind scheme in case of the first method. These type of schemes are characterised by relatively large dissipation and damping of unwanted oscillations. The time-centred upwind scheme, however, does *not* damp oscillations at Courant numbers (Eq. (5.27)) higher than approximately 10 (this is very for radon transport, but may occur at the centre of the pressure box). In these situations it is recommended to use a total implicit scheme. Disadvantage is that this scheme introduces even more dissipation but theoretically, all oscillations are damped and it is expected that at all magnitudes of the time step, the solution is smooth. Unfortunately, in some situations, this is not the case for the two-dimensional scheme. The cause of this is not understood completely. Probably the prediction made in the first step of the ADI-procedure deviates too much from the eventual solution found in the second step.

   We may conclude that if oscillations occur under advective conditions, this can be suppressed by the following countermeasures:

   (a) Change to a total implicit scheme ($\theta = 1$) and if this does not help:

   (b) Reduce the time step until the oscillations disappear.

   It should be emphasised that these countermeasures are only effective if the pressure field was calculated accurately enough.

Chapter 8

Results, conclusions and recommendations

In this chapter the results will be presented of model calculations of radon transport in the radon vessel with the 1D and 2D numerical model. These calculations are compared with measurements of the radon concentration in the sand at the central axis of the vessel. Based on this comparison conclusions will be drawn. Before model calculations could be carried out, it was necessary to obtain values of the emanation factor and the tortuosity of the sand presently inside the vessel. These parameters were derived from an analysis with the analytical diffusion model presented in Chapter 4. The procedure used to determine these parameters will be outlined.

8.1 Determination of the emanation factor and the tortuosity

Initially it was planned to measure the emanation factor (and later also the tortuosity) of the sand inside the vessel with independent measurements. The emanation factor can be measured with an exhalation meter, developed at the KVI. A description of the instrument and the method to determine the emanation factor are decribed in [Va92b]. In short: this instrument consists of a closed volume with a sample inside of which the emanation factor is to be determined. Radon atoms will escape from the sample and the ionised radon progeny that are produced in the decay are electrostatically collected on a foil just in front of a solid-state detector. The count rate is a measure for the radon concentration inside the volume. From this radon concentration the emanation factor can be calculated if the radium concentration is known (e.g. from γ-ray spectroscopy). With this instrument the radon emanation factor of the sand presently in the radon vessel was determined several times. This resulted in an average value of approximately 0.13. However, the experimental data of the radon vessel experiments could not be reproduced with this emanation factor. These experiments readily indicated an emanation factor of at least 0.2. For this reason it was decided to ignore the results of the experiments with the exhalation meter for the time being. At the moment measurements are in progress and planned to examine the cause of this discrepancy.

Further, it is planned to measure the tortuosity of the sand in an independent expe-

riment. The principle of this measurement is that the electrical conductivity of a sand column saturated with a saline solution depends on the tortuosity (due to the path elongation of the ions in the solution). The construction of this instrument is in progress, so that for the first model calculations it was unevitable to rely on the value of the tortuosity determined from a radon vessel experiment itself. Consequently two parameters, the tortuosity and the emanation factor, had to be determined before model calculations could be performed.

In Chapter 4 an analytical expression was derived for diffusive radon transport in which the radon vessel was treated as a 1D set-up. This analytical model describes the radon concentration as a function of time and height without advection and with an initial condition that the radon concentration is zero at every height. Also an expression was derived with another initial condition, but this situation is not considered in the radon vessel experiments. In Table 2.3 an overview of the measurements with the radon vessel is given. In the measurements of type 1, starting from an initally zero radon concentration, the ingrowth of the radon concentration in the vessel without the lid was determined without advection as a function of height (the nine probes) and time. The analytical expression (Eq. (4.53)) was fitted to the experimental data. For this purpose the radon concentration was considered as a function of time for each probe individually because the radon concentration at a position close to the bottom reaches a higher concentration in equilibrium than at a position closer to the top of the sand column [Va93c] . Thus, nine fits, in which the tortuosity τ and the emanation factor η were the two parameters to be determined, were produced for the nine probes. Each fit gives values for τ and η and the resulting average values for the emanation factor and the tortuosity are (already given in Table 2.2):

$$\begin{aligned} \tau &= 0.73 \pm 0.06 \\ \eta &= 0.243 \pm 0.013. \end{aligned}$$

These values were used as input for the numerical models to analyse the measurements of type 2 in which we have combined diffusive and advective radon transport. These fits are only valid when the radon vessel can be treated as a one dimensional set-up. 2D-model calculations show that this is the case.

8.2 1D-model calculations

1D-model calculations were carried with the parameters given in Table 2.2 and with the air flows induced in the sand column given by the type 2 measurements in Table 2.3. Further points of interest considering the 1D-calculations are:

- The height of the radon vessel was 1.86 m. This height was taken to correct for the curved bottom of the vessel. The height of the vessel is 2 m at the central axis only, see Fig. 2.2.
- The top of the pressure box was situated 1.63 m below the top of the sand column (same distance as in reality) and the thickness was 0.03 m. Thus the bottom of the pressure box was situated 0.2 m above the effective bottom of the vessel.

- The grid spacing was not uniform but varied from 0.1 mm near the pressure box to 1 cm inside the sand. The reason for the refinement of the grid near the pressure box is based on considerations discussed in section 6.3.2.

- For the grid point that represents the top of the sand column, the radon concentration was taken 0 Bq m^{-3}. Also the radon concentration of the air flow that enters the pressure box (C_0 in Eq. 6.15) was taken 0 Bq m^{-3}. It was confirmed experimentally that these radon concentrations are close to zero.

In summary, for the quantities that occur in Eq. (6.1) the following values were taken:

$$\begin{aligned} \beta &= 0.36 \\ D &= 2.89 \cdot 10^{-6}\ \mathrm{m^2\,s^{-1}} \\ k &= 5.45 \cdot 10^{-11}\ \mathrm{m^2} \\ \lambda &= 2.1 \cdot 10^{-6}\ \mathrm{s^{-1}} \\ \epsilon &= 0.36 \\ \epsilon S = \eta\rho\lambda C_{Ra} &= 0.243 \cdot 1760 \cdot 2.1 \cdot 10^{-6} \cdot 3.68 \\ &= 3.3 \cdot 10^{-3}\ \mathrm{Bq\,m^{-3}s^{-1}} \end{aligned}$$

(The bulk diffusion coefficient D for dry soil is, according to Eq. (3.11), the porosity times the tortuosity times the diffusion coefficient of radon in air.)

8.2.1 Results

In Fig. 8.1 the results are presented for the 1D-model calculations. Also the experimental data are presented for the air flows as indicated in Table 2.3. The error bars for the radon concentration are, if not visible, within the size of the markers. From Fig. 8.1 one notices that the model calculations give a reasonable description of the data at J = 0, 6.5 and 10 L min^{-1}. For the intermediate flows the calculations are not able to reproduce the concentration values in the region above the pressure box. Here the data show a much larger dip than the calculations. It was already noticed at the end of Chapter 6 (1D numerical model) that the air enters the pressure box at the centre. As a result the air in the pressure box will also flow in the radial direction. With the 1D-model it is impossible to include such a flow and the effect of this radial flow must be analysed with the 2D-model.

8.3 2D-model calculations

In Fig. 8.2 a schematic presentation is shown of the radon vessel without the lid as used in the 2D-model calculations. The quantities characterising the sand and the dimensions in the z-direction were the same as used in the 1D-model. Features that were dealt with in the 2D-model are the radial dimensions of the pressure box and the ring, situated at the same height as the bottom of the pressure box. Further points of attention for the 2D-model calculations are:

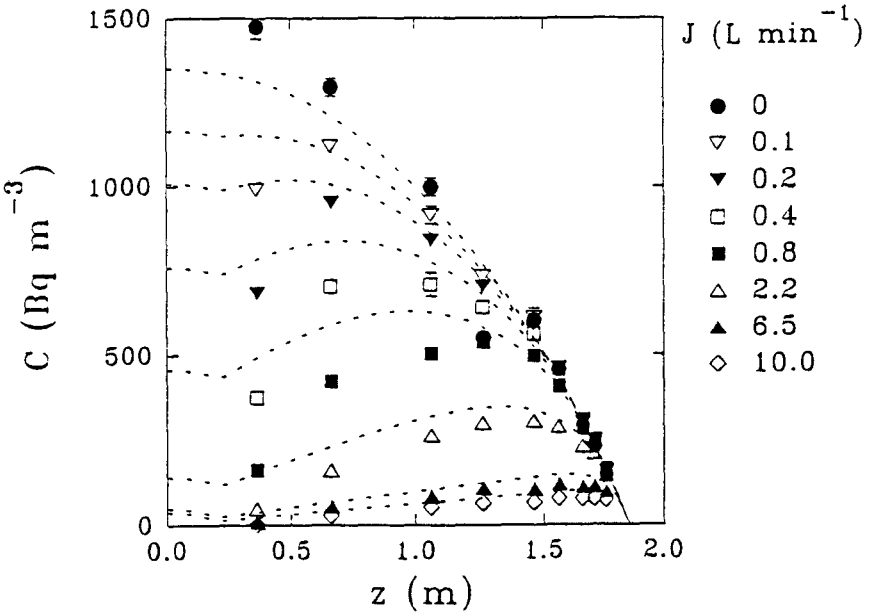

Figure 8.1: Results of the 1D-model calculations (dashed lines) compared with results of the measurements (markers) with the radon vessel. The air flows are indicated in the figure. Error bars are, if not visible, within the size of the markers.

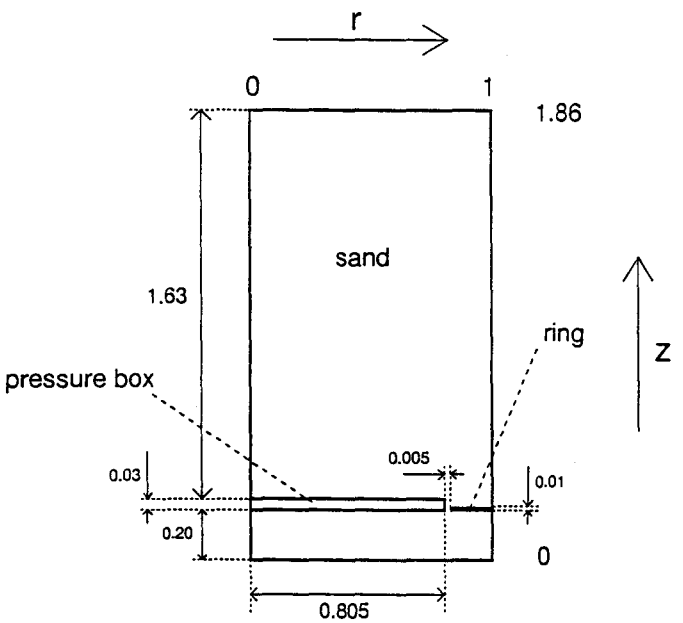

Figure 8.2: Schematic presentation of the radon vessel without the lid, used in 2D-model calculations. Dimensions are in meters.

- At the radius of the pressure box an impermeable object was modelled with a thickness of 3 mm and a height of 4 cm. In reality the outside of the pressure box is closed. The reason for taking an impermeable object with a larger height than the pressure box itself is that in this case we do not have grid points for which the soil parameters change in more than one direction (see the discussion in Section 7.2.4). This deviation from reality in not considered to be serious.
- The radius of the pressure box was 0.805 m (including the object that closes the pressure box at this position) and the inner radius of the ring at the same height was 0.81 m, leaving only a space of 5 mm between these two objects.
- The height of the ring at the same height as the pressure box was 1 cm.
- The pressure box was treated as a medium. The parameters for this medium were:

$$\begin{aligned} \beta &= 1 \\ D &= 1.1 \cdot 10^{-5}\ \mathrm{m^2\,s^{-1}} \\ k &= 1 \cdot 10^{-4}\ \mathrm{m^2} \\ \lambda &= 2.1 \cdot 10^{-6}\ \mathrm{s^{-1}} \\ \epsilon &= 1 \\ \epsilon S &= 0. \end{aligned}$$

  The main differences with the sand parameters are the value of the permeability k and that no radon is produced inside the pressure box. The k-value for the pressure box is about a factor 10^7 larger than of the sand. This number is arbitrary since we do not know the permeability of the pressure box. We do know that it is much higher than of the sand. Taking in the calculations a k-value which is an order in magnitude higher or lower than 10^{-4} m^2 showed hardly changes in the calculated radon concentration.
- In case an air flow is induced inside the sand column, air enters the pressure box at the centre and leaves the sand column at the top. The pressure field was calculated with boundary conditions that the pressure is zero at the top of the sand column and has a certain positive value at the centre of the pressure box. A possibility is to fix the pressure for all grid points at $r = 0$ in the pressure box. However, it was decided to fix the pressure at one grid point; i.e for the grid point at $r = 0$ m and $z = 0.215$ m. For this grid point the radon concentration was set at a constant value. This value represents the radon concentration of the incoming air and was set at 0 Bq m^{-3}.
- The grid spacing was non-uniform in both the z and r-direction. In the z-direction the grid was most refined in the middle of the pressure box (grid spacing 1 mm) and was most coarse (5 cm) in the middle of the vessel. In the region close to the pressure box the grid spacing was 5 mm.

  In the r-direction the most refined grid was situated at the narrow region between the pressure box and the ring (grid spacing 1 mm). Near the central axis the grid spacing was refined to 5 mm, whereas the grid spacing at other radii was approximately 4 cm.

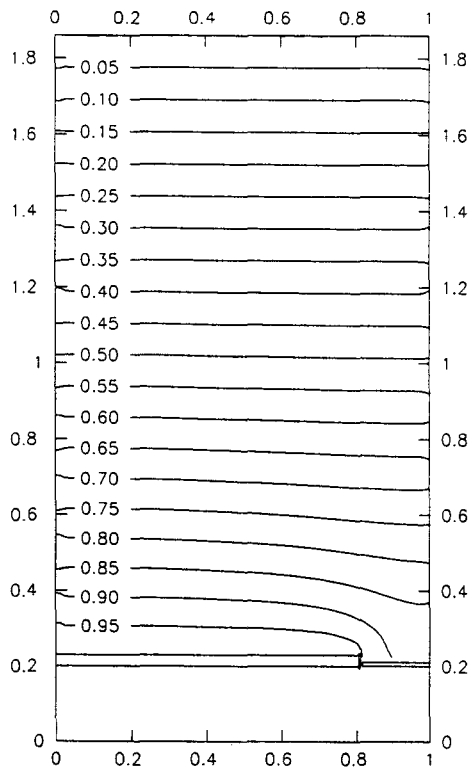

Figure 8.3: Pressure field in the sand part of the radon vessel represented by isobars. The pressure at the centre of the pressure box is set at 1 Pa and is set at 0 Pa at the top of the sand column. The permeability of the pressure box is much larger than the permeability of the sand.

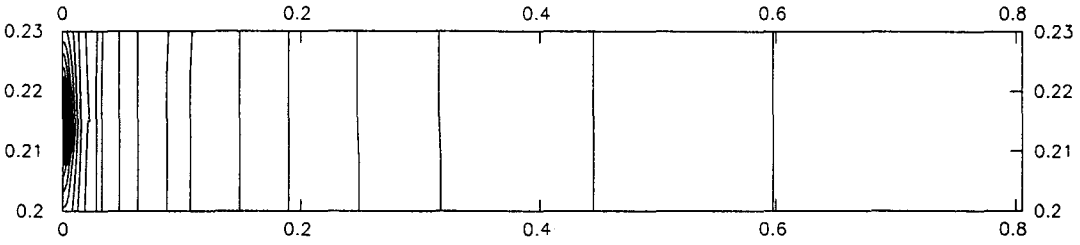

Figure 8.4: Pressure field in the pressure box. The pressure at the middle of the centre of the pressure box is 1 Pa. Near the radius of the pressure box, the pressure is 0.99993 Pa.

8.3.1 Results

Before radon concentrations can be calculated with the 2D-model, the pressure field must be calculated first. This includes a numerical procedure itself and the form of this pressure field greatly influences the radon concentration distribution inside the vessel.

The pressure field

In Fig. 8.3 the pressure field inside the sand is shown when the pressure at the centre of the pressure box is set at 1 Pa. From this figure it is seen that the pressure field is stratified horizontally except for the region just above the ring. Between the pressure box and the bottom of the vessel the pressure differences are very small and are close to 1 Pa. Since the air flow is vertical and uniformly distributed over the radius there is almost only diffusion and no radial advective radon transport inside the sand. In contrast with the situation in the sand, the pressure field in the pressure box is stratified *vertically*, see Fig. 8.4. This means that the air flow is almost totally in the radial direction in the pressure box, as could be expected in view of the high permeability of the box in comparison with the permeability of the sand. Near the outer radius of the pressure box, the pressure is 0.99993 Pa. Thus the pressure differences inside the box are very small, but since the air flow is proportional to $k\nabla p$ still large air flows occur in the pressure box. In the neighbourhood of the central axis, in the middle of the pressure box, the air speed is approximately 5 cm s^{-1} when the pressure at the centre is 1 Pa, corresponding with an air flow of 0.34 L min^{-1}. In the radon vessel experiments air flows up to 6.5 L min^{-1} were induced, corresponding with an air speed at the central axis of about 1 m s^{-1} (!). At this air velocity the mesh Reynolds number (Eq. (6.20)) is approximately 300. The consequences of this large mesh Reynolds number will be discussed later.

The radon concentration

In Fig. 8.5 and 8.6 the results are presented of calculations of the radon concentration in the equilibrium state for air flows varying from 0 (only diffusion) to 6.5 L min^{-1}. In the case that we only have diffusive transport, the radon concentration as function of the radius r varies only slightly. With reference to the fitting procedure in which the emanation factor and tortuosity were determined when only diffusive transport takes place, the 2D-model calculations strongly support the assumption of the one-dimensionality. Under combined diffusive and advective conditions we see that the radon concentration has a two-dimensional structure. This is probably caused by the advective radial transport of radon inside the pressure box (radon enters the pressure box due to diffusion). In the sand the air flows are vertical and variation of the radon concentration as function of the radius will be smoothed by radial diffusion. For this reason, at low air flows, the isoconcentrates are stratified in the upper layer of the sand column. This area of horizontal stratification becomes smaller at higher air flows because the radon atoms move faster to the top of the sand column with increasing air velocity. In other words: less time is given to the diffusion process to smooth the radon profile.

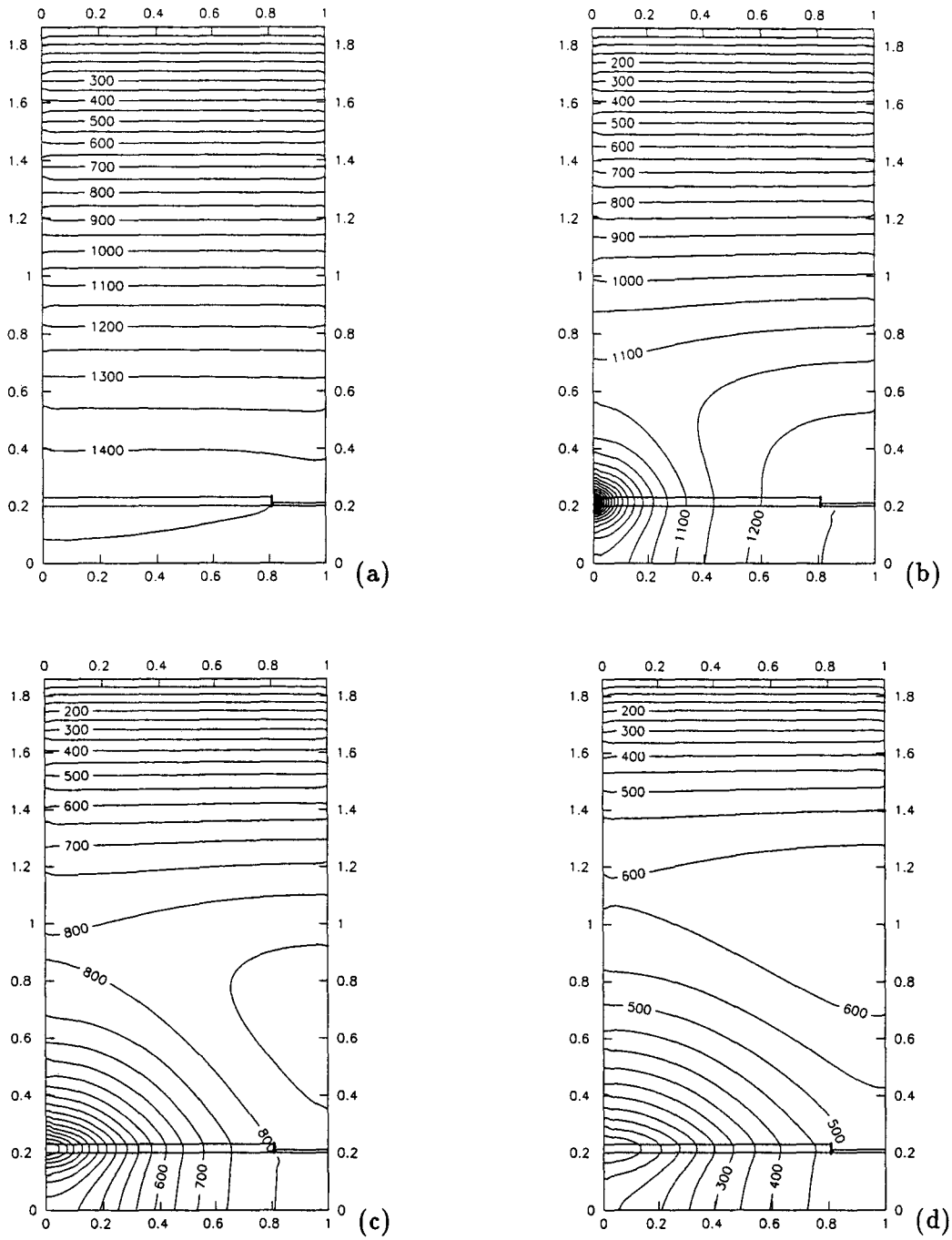

Figure 8.5: Results of 2D-model calculations of the radon concentration in the radon vessel. The induced air flows are (a) 0, (b) 0.1, (c) 0.4, and (d) 0.8 L min^{-1}. Radon concentrations are presented in Bq m^{-3}.

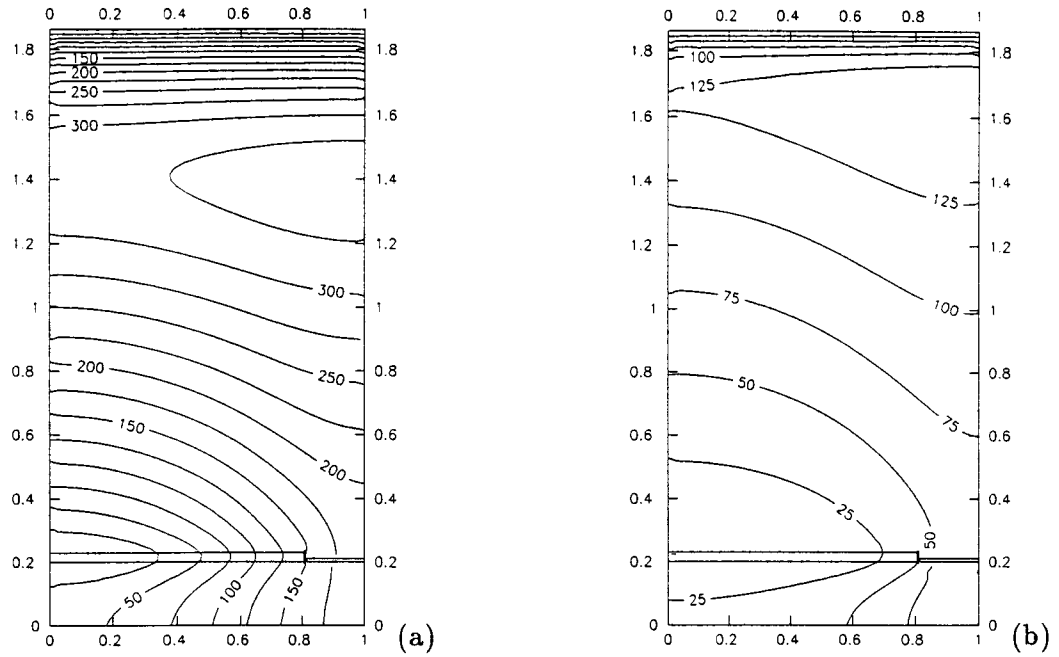

Figure 8.6: Results of 2D-model calculations of the radon concentration in the radon vessel. The induced air flows are (a) 2.2 and (b) 6.5 L min^{-1}. Radon concentrations are presented in Bq m^{-3}.

Due to radial transport of radon in the pressure box, the radon concentration at the central axis of the vessel is lower than calculated with the 1D-model. In Fig. 8.7 the radon concentration at the central axis, calculated with the 2D-model, is given in combination with the experimental data. This figure may be compared with Fig. 8.1 were the results of 1D-calculations were presented in a similar manner. It is seen that the 2D-model gives better values of the radon concentration at the central axis. This is an indication that the predicted two-dimensional structure of the radon concentration in the vessel gives a better representation of the real situation.

However, assuming that the error bars of the data points are correct and there were no systematic errors involved in the measurements, the 2D-model still does not describe the radon concentration correctly. See c.q. the curves for J = 0.1, 0.4, 0.8 and 2.2 L min^{-1}. One notices that for J = 0 and 0.1 L min^{-1} the calculations yield lower values, whereas for J = 0.4, 0.8 and 2.2 L min^{-1} the calculated values come out too high. At the moment it is not clear what causes this difference.

First, the 2D-model is not tested thoroughly; it can not be garantueed that model calculations are correct although the fact that using two different techniques (with and without applying continuity of radon flux) give almost the same results, seems reassuring. Still, since both method are based on the finite-difference approach, this is not a good prove of correctness.

Secondly, the tortuosity and permeability in the horizontal and vertical direction need not be the same (depending on the manner of compaction). Especially at intermediate flow rates this might be of large influence on the radon concentration at the central axis.

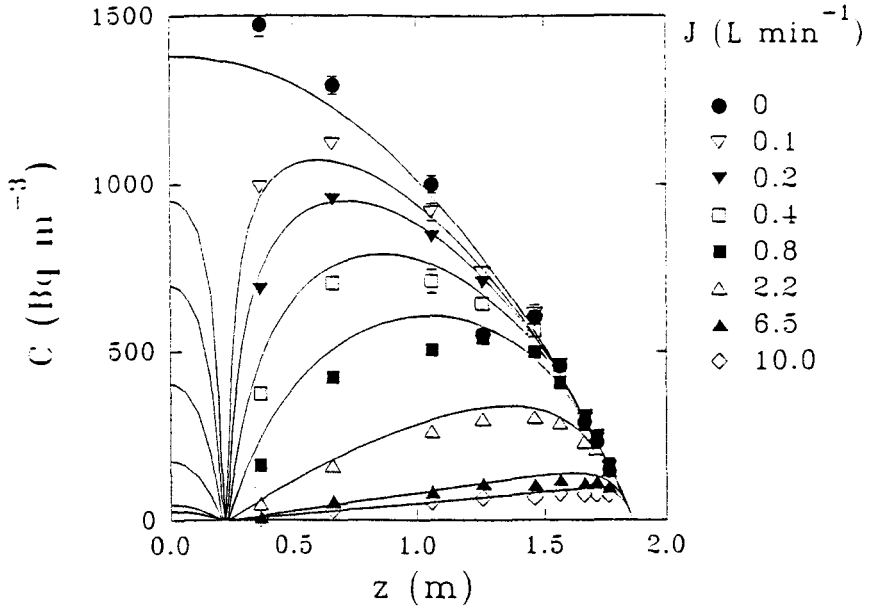

Figure 8.7: Radon concentration at function of the height at the central axis, computed with the 2D-model (solid lines), compared with the experimental data (markers). The air flows are indicated in the figure. Error bars are, if not visible, within the size of the markers.

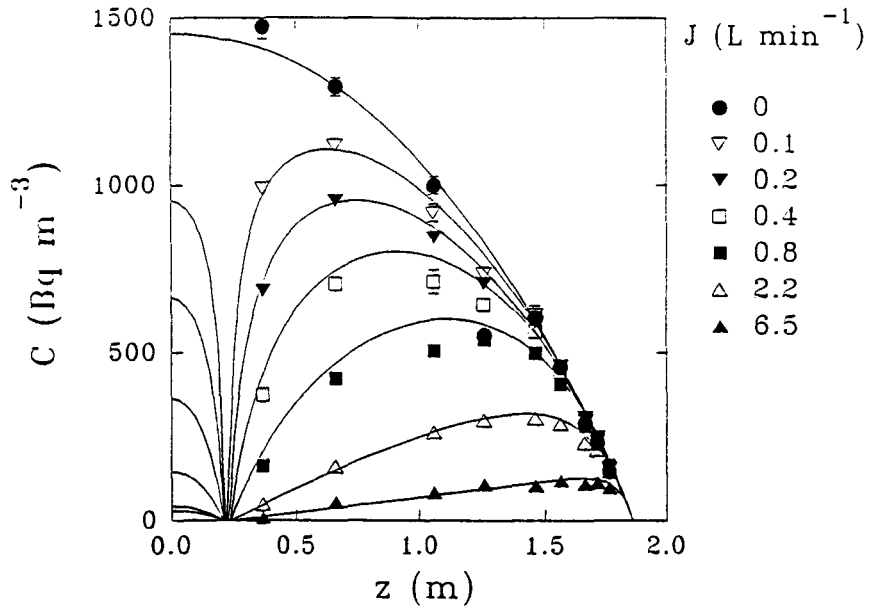

Figure 8.8: Similar to Fig. 8.7, only here the model calculations were carried out with a 20% lower diffusion coefficient and 10% lower emanation factor.

Thirdly the sand parameters between the type 1 and type 2 measurements may have changed. Model calculations were performed with values for the emanation factor and the tortuosity found with the type 1 measurements. If these parameters have changed, the input parameters were incorrect for the modelling of the type 2 measurements. In Chapter 2 it was discussed that the emanation factor increases with increasing moisture content. If the sand was moisturised during the type 1 experiments, the emanation factor found could have been higher than was the case during the experiments with combined diffusion and advection. Moreover, during these experiments an air flow was continuously induced in the sand column. This might have dried the sand. If these assumptions are correct it is not justified to rely on the values found for η and τ.

For these reasons 2D-model calculations have been performed with another emanation factor and tortuosity to check if it was possible to reflect the experimental data better. The result of this 'trial' is presented in Fig. 8.8. This figure is similar to Fig. 8.7, only the diffusion coefficient was 20% lower and the emanation factor was 10% lower. It is seen that the calculations fit the experimental data much better. The fact that the diffusion coefficient had to be lowered supports the possibility that the sand was moisturised in the diffusion experiments.

At the moment measurements are in progress with the lid installed, leaving only a space of 6 cm between the top of the sand column and the lid. In this situation, without advection, the radon concentration is practically equal everywhere in the sand because radon can not escape into free air. With this experiment the emanation factor can be determined more precisely and preliminary results indicate an emanation factor of approximately 0.21, indeed about 10% lower than determined with the type 1 experiments. After these measurements, diffusion experiments must be carried out to check whether the diffusion coefficient is also lower than measured earlier.

8.4 Discussion and recommendations considering the 2D-model

8.4.1 The pressure box

The pressure box was modelled under the assumption that it can be treated as a porous medium. In reality the pressure box is filled with a glass fiber grating with openings through which air can be transported. The air flow is probably turbulent because of the intermittent blockages of the grating and different positions of the openings. As a result, next to the permeability of the box, the diffusion coefficient is not well known too. Model tests with a diffusion coefficient of $1.1 \cdot 10^{-4}$ $m^2\,s^{-1}$ for the pressure box resulted in a higher radon concentration at the central axis. The increase was higher for points close to the pressure box (about 10%) than for points closer to the top of the sand column. Tests with a smaller diffusion coefficient showed that the decrease of the radon concentration at the central axis of the vessel was minimal. Probably dissipation due to the numerical procedure was dominating over diffusion in the pressure box (tests were carried out with an air flow of 3.4 L min^{-1}) so that a lower diffusion coefficient does not make much difference.

The centre of the pressurebox

From Figs. 8.7 and 8.8 it is seen, as was mentioned at the beginning of Section 8.3, that the radon concentration at the centre of the pressure box is zero when an air flow is induced. In the model calculations the grid point at the centre of the pressure box acts as a sink for radon. Radon 'disappears' at this grid point due to diffusion. At low air flows the concentration gradient close to this grid point can be large and the radon loss might be substantial. At large air flows the radon concentration at this position is very low and gradients are small. However, when the mesh Reynolds number is in the order of 300 (air flow approximately 6.5 L min^{-1}), the dissipation is, using an upwind scheme and $\theta = 1$ and a small time step (such that ν stays small), also about a factor 300 larger than the diffusion coefficient of radon in air. Fortunately, the concentration gradient at the centre of the pressure box is about 10^{-7} Bq m^{-3} m^{-1} so that the loss of radon due to dissipation can be neglected.

A possible solution to avoid the problem of radon loss at low air flows, is refinement of the grid at the centre of the pressure box. As a consequence the sink is smaller and air flows are larger close to the grid point where the radon concentration is set at a constant value (in the calculations it was 0 Bq m^{-3}). On the other hand when refinement of the grid in the pressure box is carried out, the pressure differences between adjacent grid points become even smaller. As a result, due to round-off, this may lead to loss of accuracy (also the convergence rate in the calculation of the pressure field drops considerably). For these reasons this measure is not recommended. Another solution is to model the plastic tube through which air enters the pressure box at the centre. With this method the radon concentration is fixed at the inlet of the tube and a radon profile will be established inside the tube. The concentration gradient at the inlet will be smaller than at the centre of the pressure box so that loss of radon is less. The pressure field inside the tube need not be calculated in the iteration process because only the air velocity, which can be calculated from the pressure field in the sand, is of importance. Implementation of this method in the 2D-model is highly recommended.

The perforated plates of the pressure box

The pressure box is covered at both sides with perforated metal plates. The perforation is, in comparison with the grain size of the sand, very coarse (a fine metal mesh attached to the metal plates prevents the sand grains from entering the pressure box). For this reason it is not justified to model the plates as a medium in the model. Also the thickness (3 mm) causes difficulties when it is tried to model these plates as a medium. In model calculations these plates were not considered and radon was free to diffuse into the pressure box. Physically, these plates act as a barrier for radon diffusion. Moreover, the air velocity locally in the openings of the plates will be larger than the air velocity in the sand column. The only correct way to solve this problem is to model all the openings individually. Because in reality these openings are 3 mm, this requires a lot of grid points in the r-direction. Presently, it is not possible to have that many grid points due to limitation of available memory. It must be said that memory management of the programme that performs the 2D-model calculations is not yet very intelligent and substantial improvement concerning this can be attained.

8.4.2 The radon vessel

The 2D-modelling has been executed with a flat bottom and consequently with an effective height for the vessel. In reality the bottom of the vessel is curved. For this reason calculations should be performed with a curved boundary as well. Model initialisation with a curved boundary is not implemented in the 2D-model and adaption of the programme probably requires considerable effort. Although it is not expected that computations with a curved boundary will have a large effect on the radon concentration above the pressure box, it recommended to add this possibility in order to analyse the influence of the curved bottom quantitatively.

8.4.3 Model tests

As was already stated before, it is not garantueed that the 2D-model is correct. To check this several model tests have to be performed. The 1D-model was tested by comparing the results with analytical solutions. This should also be carried out with the 2D-model, although analytical solutions for 2D-problems are much more difficult (if not impossible) to find, especially for cylindrical symmetries. Furthermore, test cases should be performed with non-homogeneous soil, for example with two different soil layers.

Another possibility is to measure the radon concentration in the sand not only at the central axis, but also as function of the radius. This may be carried out by means of inserting a hollow needle axially at the top of the sand column at different radii. With this needle air may be sucked out of the sand for radon concentration analysis. With the experimental data the 2D-structure could be visualised and compared with the calculated radon concentration. Such experiments are planned.

8.5 Conclusions

In this report the mathematical description of radon transport in porous materials has been discussed. This theory has been applied to the situation in the laboratory facility 'the radon vessel', with the use of 3 models. An analytical model for diffusive radon transport in homogeneous soil and two numerical models that calculate the radon concentration for a one and two-dimensional situation as function of time. Model calculations were compared with measured values. From this exercise the following conclusions can be drawn:

- Under diffusive conditions only, the radon vessel can be modelled in one dimension. This is indicated by 2D-model calculations, presented in Fig. 8.5 (a). Under these circumstances the analytical time-dependent model given in chapter 4 can be used to describe radon transport.

- When an air flow is induced in the sand column in the radon vessel, 1D-model calculations are not adequate due to radial radon transport in the pressure box (when the box is at over pressure) and 2D-model calculations are necessary.

- With input parameters based on measurements with only diffusion, the 2D-model predicts the radon concentration at the central axis of the vessel within 15%. Recent measurements with the radon vessel show that some input parameters might have

been too high. Model tests with adapted input parameters show that the radon concentration can be predicted within approximately 5%.

- In order to check the mathematical description of radon transport, input parameters for the modelling should be obtained with measurements independent of the radon vessel itself. The emanation factor and the tortuosity were determined on the basis of radon vessel experiments. Presently efforts are undertaken to measure these parameters independently.

Finally, especially the 2D numerical model has provided us more knowledge of the situation in the radon vessel. The reasonable agreement between theory and modelling on the one hand and experimental data on the other hand has given more certainty with respect to our understanding of radon transport in soil. However, for the moment this knowledge is limited to the simple condition with homogeneous dry soil. Experiments carried out on more complex situations are planned of which it is hoped that they can also be understood with our present insight, although we can only be sure that new difficulties, either experimentally or theoretically and numerically, will have to be coped with. In any case the final goal, to be able to assess radon transport *in situ* better on the basis of the radon vessel experiments, has drawn a bit nearer. Hopefully the 2D numerical model, after enhancement and extension, will contribute to the analysis of the real situation under houses and thereby also, by calculations of the effectiveness of countermeasures, to the reduction of the radon concentration in our interior environment.

Acknowledgements

I would like to thank Emiel van der Graaf for his support and accessibility to questions. Especially his ability to explain theoretical problems clearly and the calmness he radiates are admired and appreciated. I am also grateful to my supervisor Rob de Meijer for offering me the possibility to complete my studies at the KVI and for adding critical observations to this report during its realization.

Further, my sincere thanks go to Claus Andersen who stimulated and helped me with the numerical techniques, incited me to be critical with respect to computer output and offered me numerous good suggestions. I would also like to thank Madito Witteman for the enormous amount of work he got through to obtain the experimental data. Hopefully, to do something in return, this report will be of interest for his Ph.D. thesis. My appreciations also go to Ilka Tánczos who helped me finding accommodation in Groningen.

Finally, I would like to thank all other people at the Environmental Physics Group who made my stay in Groningen really enjoyable.

References

An92a Van der Spoel, W.H. and Van der Graaf, E.R.
KVI Annual report p. 99-100, 1992.

An92b Andersen, C.E.
Entry of Soil Gas and Radon into Houses. Risø National Laboratory, Roskilde, Denmark. Risø-R-623(EN), 1992.

An93 Andersen, C.E.
Personal communications. 1993.

An84 Anderson, D.A., Tannehill, J.C. and Pletcher, R.H.
Computational Fluid Mechanics and Heat Transfer. Hemisphere Publishing Corporation, 1984.

Ba91 Vaas, L.H., Kal, H.B., De Jong, P. and Slooff, W.
Basisdocument radon. Rijksinstituut voor volksgezondheid en milieuhygiène, Bilthoven. Rapport nr. 710401014, 1991.

Bi60 Bird, R.B. Stewart, W.E. and Lightfood, E.N.
Transport Phenomena. John Wiley & Sons, 1960.

Ca59 Carslaw, H.S. and Jaeger, J.C.
Conduction of heat in solids. Second edition. Clarendon Press Oxford, 1959.

Ca69 Carnahan, B., Luther, H.A. and Wilkes, J.O.
Applied Numerical Methods. John Wiley & Sons, 1969

Cr56 Crank, J.
The mathematics of diffusion. Clarendon Press Oxford, 1956.

Me91 De Meijer, R.J.
Infiltratie van radon in woningen. KVI internal report R18. Also published in the series Stralenbescherming VROM, nr: 50A. 1991

Ro91a Rogers, V.C. and Nielson, K.K.
Multiphase radon generation and transport in porous materials. Health Physics, vol. 60, no. 6, pp. 807-815, 1991.

Ro91b Rogers, V.C. and Nielson, K.K.
Correlations for predicting air permeabilities and ^{222}Rn diffusion coefficients of soils. Health Physics, vol. 61, no. 2, pp. 225-230, 1991.

Va92a Van der Graaf, E.R., Heijs, S., De Meijer, R.J., Put, L.W. and Mulder, H.F.H.M.
A facility to study transport of radon in soil under controlled conditions. Radiation Protection Dosimetry Vol. 45 No. 1/4 pp. 223-226, 1992

Va92b Van der Graaf, E.R., Heijs, S., De Meijer, R.J., Put, L.W. and Mulder, H.F.H.M.
The choice of soil type for radon vessel experiments. Techn. Doc. KVI/RV-04, 1992.

Va93a Van der Graaf, E.R., Ten Have, R. and De Meijer, R.J.
Pressure field measurements in the radon vessel and experimental determination of the shape factors of the probes. Techn. Doc. KVI/RV-07, in progress.

Va93b Van der Graaf, E.R., Witteman, G.A.A., Ten Have, R., De Meijer, R.J. and Put, L.W.
Determination of the relative efficiencies of seven Pylon model AB-5 portable radiation monitors and 21 Lucas cells. KVI internal report R42, 1993.

Va93c Van der Graaf, E.R., Witteman, G.A.A., Van der Spoel, W.H., Andersen, C.E. and De Meijer, R.J.
Measurements on, and modelling of diffusive and advective radon transport in soil. Presented at the "First International Workshop on Indoor Radon Remedial Action", Rimini, Italy. 1993.

Va93d Van der Graaf, E.R.
Private communications. 1993.

Appendix A

Thomas algorithm

Thomas algorithm describes a simple method to solve a tridiagonal system of linear equations. Mathematically such a system can be written, using matrix notations:

$$\begin{pmatrix} A_1 & B_1 & 0 & 0 & 0 & 0 & 0 & ..... & 0 \\ C_2 & A_2 & B_2 & 0 & 0 & 0 & 0 & ..... & 0 \\ 0 & C_3 & A_3 & B_3 & 0 & 0 & 0 & ..... & 0 \\ 0 & 0 & . & . & . & 0 & 0 & ..... & 0 \\ 0 & 0 & 0 & . & . & . & 0 & ..... & 0 \\ . & . & . & . & . & . & . & ..... & . \\ . & . & . & . & . & . & . & ..... & . \\ . & . & . & . & . & . & . & ..... & . \\ 0 & .... & 0 & 0 & 0 & 0 & 0 & C_{n-1} & A_{n-1} & B_{n-1} \\ 0 & .... & 0 & 0 & 0 & 0 & 0 & 0 & C_n & A_n \end{pmatrix} \begin{pmatrix} U_1 \\ U_2 \\ U_3 \\ . \\ . \\ . \\ . \\ U_{n-1} \\ U_n \end{pmatrix} = \begin{pmatrix} D_1 \\ D_2 \\ D_3 \\ . \\ . \\ . \\ . \\ D_{n-1} \\ D_n \end{pmatrix} \quad \text{(A.1)}$$

in which A_i, B_i, C_i and D_i $(i = 1...n)$ are known and U_i $(i = 1...n)$ are the unknows for which the system has to be solved. The first step in Thomas algorithm is to combine two equations subsequently such that all coefficients C_i become zero. First row 1 and 2 is combined, then row 2 and 3 etc. It is expressed as

$$\left.\begin{array}{lcl} A_i & := & A_i - \frac{C_i * B_{i-1}}{A_{i-1}} \\ D_i & := & D_i - \frac{C_i * D_{i-1}}{A_{i-1}} \\ C_i & := & 0 \end{array}\right\} \quad (i = 2...n) \qquad \text{(A.2)}$$

where the 'becomes' sign (:=) is used. With this procedure the new matrix only has two non-zero values in each row. In the last row, however, the only non-zero value is A_n and we can directly obtain the unknown U_n:

$$U_n := \frac{D_n}{A_n} \qquad \text{(A.3)}$$

Row $n-1$ of the new matrix describes a relation between U_n and U_{n-1} and therefor, since U_n is known, we can obtain U_{n-1}. Proceding in a similar way, all U_i can be found. It is expressed as:

$$U_i := \frac{D_i - B_i * U_{i+1}}{A_i} \qquad (i = n-1...1) \tag{A.4}$$